https://ntrs.nasa.gov/search.jsp?R=19970011270 2020-06-16T03:04:09+00:00Z

NASA Technical Memorandum 110436

Direct Numerical Simulation of Incompressible Pipe Flow Using a B-Spline Spectral Method

Patrick Loulou, Stanford University, Stanford, California
Robert D. Moser and Nagi N. Mansour, Ames Research Center, Moffett Field, California
Brian J. Cantwell, Stanford University, Stanford, California

February 1997

National Aeronautics and
Space Administration

Ames Research Center
Moffett Field, California 94035-1000

Abstract

A numerical method based on b-spline polynomials was developed to study incompressible flows in cylindrical geometries. A b-spline method has the advantages of possessing spectral accuracy and the flexibility of standard finite element methods. Using this method it was possible to ensure regularity of the solution near the origin, i.e. smoothness and boundedness. Because b-splines have compact support, it is also possible to remove b-splines near the center to alleviate the constraint placed on the time step by an overly fine grid. Using the natural periodicity in the azimuthal direction and approximating the streamwise direction as periodic, so-called time evolving flow, greatly reduced the cost and complexity of the computations.

A direct numerical simulation of pipe flow was carried out using the method described above at a Reynolds number of 5600 based on diameter and bulk velocity. General knowledge of pipe flow and the availability of experimental measurements make pipe flow the ideal test case with which to validate the numerical method. Results indicated that high flatness levels of the radial component of velocity in the near wall region are physical; regions of high radial velocity were detected and appear to be related to high speed streaks in the boundary layer. Budgets of Reynolds stress transport equations showed close similarity with those of channel flow. However contrary to channel flow, the log layer of pipe flow is not homogeneous for the present Reynolds number. A topological method based on a classification of the invariants of the velocity gradient tensor was used. Plotting iso-surfaces of the discriminant of the invariants proved to be a good method for identifying vortical eddies in the flow field.

Acknowledgements

The authors would like to acknowledge many very useful discussions with Drs. Alan Wray, Karim Shariff and Mike Rogers. Computer support by the NAS computational facility is also gratefully acknowledged.

Contents

List of Tables

List of Figures

Nomenclature

Roman symbols

$\mathbf{A}, a_{ij}$	Mass matrix.
A_{ij}	Velocity gradient tensor.
$\mathbf{B}, b_{ij}$	Viscous matrix.
$\mathbf{b}, b_i$	Arbitrary right hand side vector (A.5).
C_f	Friction coefficient (3.1).
CFL	Courant-Friedrichs-Lewy number.
D	Diameter of the computational domain.
E	Energy spectrum.
$\mathbf{e_r}, \mathbf{e}_\theta, \mathbf{e_z}$	Unit vectors of cylindrical coordinate system.
$F(u)$	Flatness or kurtosis (3.10).
$\mathbf{f}_{\mathbf{nl}}, f_{\mathbf{nll'}}$	Nonlinear convective term.
$f\mathbf{e_z}$	Streamwise pressure gradient.
$f(r)$	Arbitrary smooth function (A.1).
G	Computational domain.
$g_l(r)$	B-spline polynomial.
H^n	Sobolev space of degree n.
k	Turbulent kinetic energy.
k_θ, k_z	Wave numbers in the θ and z directions.
L_z	Length of the computational domain.
N_k	Number of knots ($N_k = N_r - S + 1$).
N_r, N_θ, N_z	Number of b-splines, azimuthal and streamwise modes.
$\mathbf{n}$	Unit outward normal vector.

P	Total pressure (2.7).
$\tilde{P}$	Numerical approximation to the pressure.
p	Static pressure.
Q	Two-point correlation.
R_2	Outer edge of domain ($= D/2$).
r	Radial coordinate.
Re	Reynolds number.
S	Degree (or order) of B-spline.
$S(u)$	Skewness (3.10).
t	Time.
U_b	Bulk velocity (2.3).
U_c	Centerline velocity.
$\mathbf{u}$	Velocity vector.
$\mathbf{u}_l$	Vector expansion function.
u_r, u_θ, u_z	Components of velocity in the r, θ, z direction.
u_τ	Friction velocity.
$\mathcal{V}$	Space of vector expansion functions (2.8).
$\mathbf{v}$	Finite dimensional approximation to $\mathbf{u}$.
$\mathcal{W}$	Space of vector weight function (2.9).
$\mathbf{w}_{l'}$	Vector weight function.
y^+	Wall coordinate; $y^+ = (R_2 - r)u_\tau/\nu$.
z	Axial, or streamwise coordinate.

Greek symbols

$\boldsymbol{\alpha}$	Expansion coefficients vector
α_l	Elements of expansion coefficients vector.
$\alpha_1, \alpha_2, \alpha_3$	Time marching coefficients.
$\beta_1, \beta_2, \beta_3$	Time marching coefficients.
$\Delta r, \Delta\theta, \Delta z$	Spacings in the r, θ, z direction.
Δt	Time step.
δ	Displacement thickness.

ϵ_{ijk}	Permutation tensor.
η_i	i^{th} knot point.
ε	Dissipation of turbulent kinetic energy.
Γ	Boundary of the computational domain.
$\gamma_1, \gamma_2, \gamma_3$	Time marching coefficients.
λ	Eigenvalue.
∇	Del operator: $\nabla = \frac{\partial}{\partial r}\,\mathbf{e_r} + \frac{1}{r}\frac{\partial}{\partial \theta}\,\mathbf{e}_\theta + \frac{\partial}{\partial z}\,\mathbf{e_z}$.
ν	Kinematic viscosity.
Ω	Vorticity spectrum.
ω	Vorticity vector.
$\omega_r, \omega_\theta, \omega_z$	Components of vorticity in the r, θ, z directions.
Φ	Arbitrary scalar function
ϕ	Mechanical dissipation of turbulent kinetic energy.
$\mathbf{\Psi}_l$	Vector stream function.
ρ	Density.
θ	Azimuthal coordinate; also momentum thickness.
$\boldsymbol{\xi}$	Finite dimensional weigth function.
ζ_1, ζ_2	Time marching coefficients.

Other symbols

$(\cdot)^{\pm}_{\pm}$	Indicates the class of expansion functions.
$(\cdot)^+$	Normalization with respect to wall variables.
$\hat{(\cdot)}$	Fourtier transformed quantity.
$(\cdot,\cdot)$	Inner product (2.12).
$\|\cdot\|_0$	L_2 norm.
$\|\cdot\|$	Absolute value.
$\bar{\cdot}$	Time and spatial averages.
$(\cdot)^*$	Complex conjugate.
$\widehat{\nabla}$	Fourier transformed del operator ($= \frac{\partial}{\partial r}\,\mathbf{e_r} + \frac{ik_\theta}{r}\,\mathbf{e}_\theta + ik_z\,\mathbf{e_z}$).

Chapter 1

Introduction

This chapter presents an overview of numerical investigations of flows in cylindrical geometries, especially pipe flow. Some background is also included on the important features of pipe flow. The objectives of the present study are laid out, and we conclude with an outline of the present work.

1.1 Numerical method

1.1.1 Background

Since the early seventies, numerical simulations of fluid flows have become an invaluable tool in the study of turbulence. Direct numerical simulations (DNS), or the simulation of fluid flows without the use of any model to resolve the smallest scales of motion, are the tool of choice when the detailed physics of fully turbulent flows are of primary importance.

The expertise and the computational resources have grown so much in the last few years that numerical simulations do more than just supplement experiments, but are now used as an independent means of exploring the physics of more and more complex flows. Flows, most of them incompressible, with one inhomogeneous direction are not uncommon; the homogeneous directions are assumed to be periodic which greatly reduces the complexity of the computations. Both unbounded, or free

shear, and bounded flows have been successfully computed using DNS; among more recent work, Moser and Moin [25] conducted a DNS of a curved channel, Moin and Kim [24] and Kim, Moin and Moser [17] a straight channel, and Rogers and Moser [38] a fully turbulent self-similar mixing layer. O'Sullivan and Breuer [30, 31] studied the growth of disturbances in pipe flow, and Sondergaard [42], studied the effect of initial conditions on the growth of a plane wake. These are typical of what are essentially two types of direct numerical simulations: the first is a transitional simulation where special care is applied to the initial conditions and where transition to turbulence is the ultimate goal of the study; the second, and more common, is a simulation of a fully developed turbulent flow where only the end-state is desired, with little or no attention paid to the transient state.

Yet, because of the cost involved in carrying DNS, practical engineering applications are still out of reach (and will be for decades). Because the smallest scales gets smaller as the Reynolds number increases, only lower Reynolds number flows in simple geometries are attainable with present day computers. Still, this does not imply that DNS do not have any practical use; as an example of usefulness of DNS, results from such simulations are often used to "fine-tune" turbulence models used in other types of simulations commonly used in day to day engineering (see for example Rodi and Mansour [36] or Mansour Kim and Moin [22]), such as large eddy simulations (LES) (e.g. Mansour, Ferziger and Reynolds [21]) and mostly, Reynolds averaged Navier-Stokes (RANS) equations. A subgrid scale model is used to resolve the finer scales of motion in the case of LES, and a turbulence model is used to resolve most of the unsteadiness in the case of RANS.

1.1.2 Survey of numerical methods

Spectral methods are used to carry out DNS because of their high degree of accuracy, giving them the ability to faithfully capture all scales of motion; derivatives of flow parameters, such as vorticity, are also represented very accurately. These methods work especially well on smooth and continuous fields, typical of incompressible turbulent flows. In the homogeneous directions periodic boundary conditions are

applied and Fourier transforms are used to simplify the equations. In addition, the use of fast Fourier transforms (FFT) which make the implementation very efficient. However, when walls are present, or more generally when a direction is not periodic, Fourier transforms are no longer applicable. One must then resort to other kinds of expansions in the cross-stream or normal to the wall direction (e.g. Spalart *et al.* [44]).

In order to be successful, a method used to solve the incompressible Navier-Stokes equations in cylindrical geometries must address two principal problems: first, imposing the continuity equation accurately, and second, accounting for the coordinate singularity which appears at the centerline ($r = 0$) when working in cylindrical coordinates. As we shall see, resolving problems associated with the coordinate singularity is the outstanding difficulty in the design of the numerical method. The problem of imposing the continuity equation arises when solving the incompressible Navier-Stokes equations, since the continuity equation appears as a kinematic constraint on the velocity field. Problems linked to imposing continuity constraint have been well documented, and the reader can consult Canuto *et al.* [7], Hughes [13] or Johnsson [15] for more on the subject.

Several methods have been employed to study fully developed turbulent flows in cylindrical geometries. All these methdos use Fourier transforms in both the streamwise and azimuthal directions, and some other form of expansion in the radial direction. It should be noted that periodicity of the azimuthal direction is *natural* and not an approximation, contrary to the streamwise direction for which periodicity implies a flow with infinite extent.

For their solution of transitional pipe flow, Leonard and Wray [20] (see also Leonard [19]), used divergence-free expansion functions in the context of a (non-Galerkin) weighted residual method. Using solenoidal, or divergence-free expansion functions alleviates the need to explicitly solve the continuity equation; thus, only two of the velocity components are independent. With the no-slip boundary condition built into the expansions and using integration by parts, the pressure term drops out of the equations, and only two unknown velocity components remain. For the radial direction they used shifted Jacobi polynomials. Treatment of the coordinate

singularity was also built into the vector expansion functions using *a priori* knowledge of the behavior of the solution near the origin. This approach guarantees the solution to be *regular**, i.e. values and derivatives are all bounded and smooth. In a slight variation, Moser, Moin and Leonard [26] used Tchebyshev polynomials instead of Jacobi polynomials to solve a fully turbulent curved channel flow. Numerically this flow is somewhat simpler to solve than pipe flow, since the presence of an inner wall eliminates the coordinate singularity.

In analyzing the growth of both linear and nonlinear disturbances in pipe flow, O'Sullivan and Breuer [30, 31], and earlier, Orszag and Patera [29], used a collocation method with scalar expansion functions instead of vector expansions, i.e. each velocity component and the pressure were represented separately. Tchebyshev polynomials were used to represent the radial direction. Time marching was achieved using the splitting method of Orszag and Kells [28] where the pressure gradient and viscous terms were integrated in a three-step process. The nonlinear term was integrated using a second order Adams-Bashforth scheme. As was the case with the method of Leonard and Wray, it a priori knowledge of the behavior of the velocity and pressure near the origin was built into the expansions.

Zhang *et al.* [55] also used a spectral method for their simulation of fully developed pipe flow. Similarly to Leonard and Wray [20], they used Jacobi polynomials as the expansion basis although not in the context of a divergence-free formulation. Time marching was carried out using a fractional step method, with a mixed explicit-implicit second order scheme. Their method also offers the possibility of resolving inflow-outflow boundaries, or spatially evolving flows, although details on the treatment of those boundary conditions were sketchy and no results using them published.

Eggels *et al.* [12] used a second order finite difference technique in the radial direction to simulate a fully developed turbulent pipe flow. Even though finite differences are much simpler to implement than a spectral method, they induce numerical diffusion and dispersion, especially at high wave number (small scales). For a given

*Certain authors prefer the terms *analytic* or *holomorphic* to regular.

accuracy, many more grid points must be used compared to a spectral method. Ultimately this reduces the highest Reynolds number that can be adequately simulated due to memory constraints of the hardware. Eggels *et al.* [12] implemented a way to alleviate the strong restriction on the time step produced by a concentration or clustering of azimuthal modes at the centerline. They treated terms involving azimuthal derivatives implicitly, and all other terms explicitly with a leap-frog scheme for the advective terms, and a lagged forward Euler scheme on the viscous terms. The values at the origin are evaluated using a first order extrapolation; they claim that first order extrapolation does not degrade global accuracy because near the center, the velocity and pressure fields are smooth. It should also be noted that in the context of finite differences, ensuring that the velocity and pressure are bounded and regular near the origin is trivial since only their values, and not derivatives, have to be accounted for.

Verzicco and Orlandi [49] also developed a second order finite difference scheme for cylindrical geometries. They treated the coordinate singularity by introducing a radial flux (ru_r) on a staggered grid, i.e. only the radial flux is evaluated at the origin. The equations were then solved with a fractional-step and approximate-factorization methods, yielding a second order method in both space and time. This method was used by Orlandi and Fatica [27] in simulating fully developed turbulent flow in a pipe with rotating wall, and by Verzicco and Orlandi [48] for a transitional round jet. However, contrary to Eggels *et al.*, no mention is made of any procedure to alleviate the constraint on the time step introduced by the increased azimuthal resolution near the origin.

1.2 Pipe Flow

Pipe flow is without a doubt the most studied flow, and the one with the broadest engineering applications. Reynolds himself [34] developed his famous scaling parameter (c.f. the Reynolds number), by conducting experiments on pipe flow. As such, pipe flow represents the ideal test case on which to apply a new numerical method: the availability of ample experimental measurements should make validation simpler. However, not all issues regarding pipe flow are resolved, and the present results should

address those as well. The next few paragraphs give the salient features of pipe flow and how it contrasts with another well studied flow: channel flow.

Pipe flow differs in many ways from channel flow (the flow between two flat plates). The first difference was observed by Patel and Head [32] who found that in the low Reynolds number range (Re), which for the purpose of the present study is the relevant range, fully developed pipe flow fails to conform to the standard logarithmic law. They found the Reynolds number had to reach a value of $Re = 10000$ (based on the bulk velocity and pipe diameter) before the mean velocity profile would match the log-law, versus a much lower $Re = 3000$ for channel flow (based on the distance between the plates). However, a more recent study of pipe flow by Durst, Jovanović and Sender [11] using a precision laser Doppler anemometry technique (LDA) found that at a Reynolds number of 7442, fully developed turbulent pipe flow obeyed the standard log law.

A second difference with channel flow lies in the transition from laminar to turbulent flow. Patel and Head [32] observed that pipe flow is purely laminar up to $Re = 2000$ after which it enters a transition regime usually triggered by disturbances at the entrance. The transition is maintained up to $Re \approx 3000$ after which the pipe becomes fully turbulent rather suddenly. For channel flow, they observed that the onset of transition appeared at $Re = 1350$ and the flow became fully turbulent for $Re > 1800$. The transition regime for pipe flow was studied in detail by Wygnanski and Champagne [52] and Wygnanski, Sokolov and Friedman [53] (see also Cantwell [5]). They found that the transition regime was actually a very complex process where two different intermittent flows were present: puffs and slugs. Puffs are present for $2000 < Re < 2700$; they are induced by large amplitude perturbations at the pipe inlet. Wygnanski *et al.* referred to the state of the flow in puffs as that of incomplete relaminarization. Slugs however are present at $Re > 3200$ and are produced by small perturbations in the boundary layer at the pipe inlet. The flow within a slug is similar to fully developed turbulence and has a well defined leading and trailing edges, and can extend over the entire length of the pipe. Leonard and Wray [20] and Leonard [19] were able to simulate puffs at $Re = 2200$, showing that methods designed to simulate time evolving flows (streamwise periodic) can capture flow features arising

from perturbed entry conditions.

Lastly, pipe flow is said to be linearly stable to small disturbances. Several investigators have focused their research on trying to find unstable linear modes in pipe flow (see for example Salwen *et al.* [40, 39], Orszag and Patera [29] and O'Sullivan and Breuer [30]). To this day, no unstable linear modes have been found. Channel flow however is linearly unstable to infinitesimal disturbances; it possesses a critical Reynolds number of 11544 above which the flow can be unstable. For pipe flow the only process that sustains and enables growth of perturbations emanates from nonlinear interactions.

1.3 Objectives

The objectives of this study are threefold:

- To develop a numerical method based on b-spline polynomials which would have an accuracy comparable to standard spectral methods and the flexibility of finite elements or finite difference methods.
- To study the fundamental behavior of wall-bounded turbulence in a cylindrical geometry, such as pipe flow.
- To establish the benchmark in pipe flow simulation.

Also, in order to assess the present methodology, several comparisons will be made with various experiments and other direct numerical simulations.

1.4 Outline

The present work is essentially divided in two parts: a detailed explanation of the numerical method, and analysis of the results.

Chapter 2 introduces the numerical method, including some basic facts about b-splines, the time marching method and the technique used to relax the resolution near the origin; it concludes with some test cases used to validate the method.

Chapter 3 presents the results from the pipe flow simulation; results include, mean flow properties, spectra, turbulent intensities, budgets of Reynolds stress transport equations and structure tensors.

Chapter 4 presents a study of flow structures using a topological method based on a classification of the invariants of the velocity gradient tensor.

Chapter 5 concludes with some final observations and recommendations for future work.

Appendix A gives a short summary of b-splines and their properties.

Appendix B exposes in great details the problem of the coordinate singularity and the steps taken to ensure smoothness and boundedness of the velocity field near the origin.

Appendix C shows how the method presented in chapter 2 and appendix B was implemented. This appendix is especially useful if subsequent modifications should be made to the computer code. This appendix outlines the entire structure of the code.

Appendix D gives the exact solution to Stokes problem used to validate the methodology and includes some background on linear stability. Those exact solutions are used in the validation section of chapter 2.

Chapter 2

Methodology

In this chapter, the numerical method that was used to solve the incompressible Navier-Stokes equations is introduced, including some coding strategies. Also included are some of the test cases that were used to validate the method.

2.1 Approach

The numerical method was designed for any incompressible turbulent flows, that can be prescribed in cylindrical coordinates (e.g. pipe flow, round jet). In other words, the method should have the flexibility to resolve both solid and free shear boundaries. Since no attempt is made at resolving inflow/outflow boundaries (spatially evolving), the flow is assumed periodic in the streamwise direction, or so-called temporally evolving flow (equivalent to a flow with infinite streamwise extent).

The present method is conceptually similar to the approaches of Leonard and Wray [20] and Moser, Moin and Leonard [26], in that it makes use of divergence-free vector expansion functions. The major difference between the present method and all the ones described before, is the use of basis splines polynomials (b-splines) to represent the radial direction, in place of Jacobi or Tchebyshev polynomials. B-splines are discrete polynomials, i.e. with local support on a given interval, whereas Jacobi and Tchebyshev polynomials have global support. Polynomials with local support lead to sparse matrices that can be efficiently stored and solved. The local nature of

b-splines enables effortless implementation of various boundary conditions, and the possibility of adjusting the precision near the origin to avoid an overly restrictive time step. Background on b-splines can be found in appendix A.

2.2 Governing Equations

The starting point for the simulations are the incompressible Navier-Stokes equations in cylindrical coordinates

$$\nabla \cdot \mathbf{u} = 0 \tag{2.1}$$

$$\frac{\partial \mathbf{u}}{\partial t} + \mathbf{u} \cdot \nabla \mathbf{u} + \nabla p = \frac{1}{Re_b} \nabla \cdot \nabla \mathbf{u} + f \mathbf{e_z} \tag{2.2}$$

where $\mathbf{u}$ is the velocity, p is the pressure, and f is a uniform body force (pressure gradient) acting in the streamwise direction which drives the flow; it is constantly adjusted such that the mass flow, $\dot{m} = \pi R_2^2 \rho U_b$, is kept constant. Because the density ρ and the radius of the pipe R_2 are constant, the constant mass flux condition implies that the bulk velocity U_b

$$U_b = \frac{2}{R_2^2} \int_0^{R_2} \overline{u}_z \; r \, dr \tag{2.3}$$

must also be constant.

All quantities have been normalized using the radius of the domain R_2 as the lengthscale, and U_b as the velocity scale (see figure 2.1)

$$r = \frac{r^\circ}{R_2} \qquad z = \frac{z^\circ}{R_2} \qquad t = \frac{t^\circ}{(R_2/U_b)} \qquad u_j = \frac{u_j^\circ}{U_b} \qquad p = \frac{p^\circ}{\rho U_b^2}$$

So, the Reynolds number in 2.2 is given by

$$Re_b \equiv \frac{U_b R_2}{\nu} \tag{2.4}$$

where ν is the (constant) kinematic viscosity.

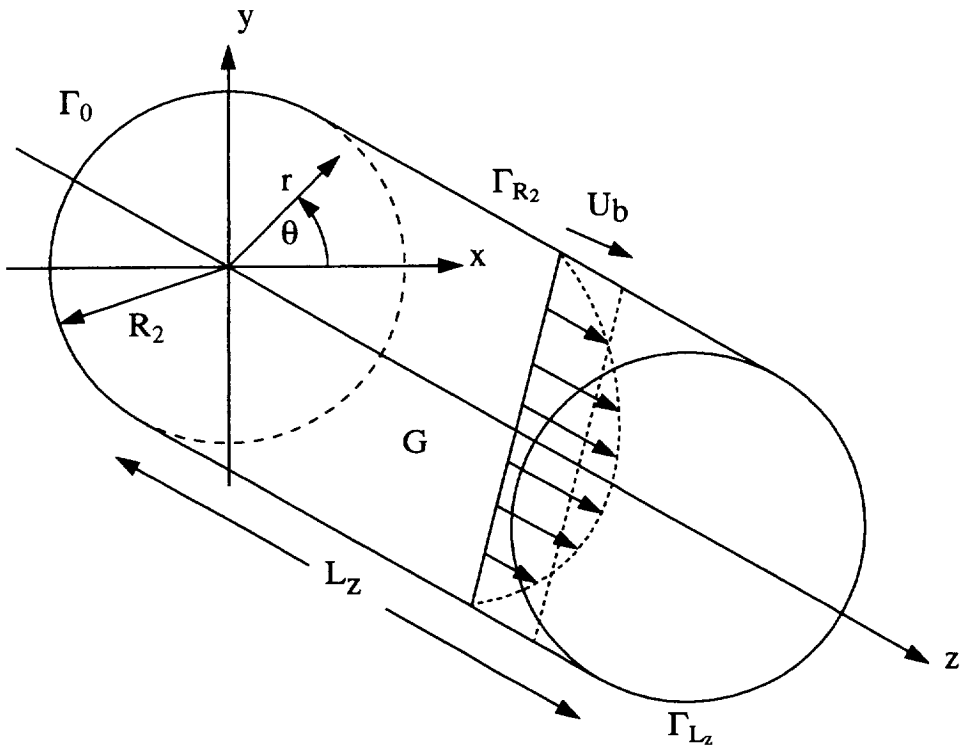

Figure 2.1: Coordinate system and computational domain

Using the following identity

$$\mathbf{u} \cdot \nabla \mathbf{u} = -\mathbf{u} \times \boldsymbol{\omega} + \frac{\nabla(\mathbf{u} \cdot \mathbf{u})}{2}$$

where the vorticity, $\boldsymbol{\omega}$, is defined as

$$\boldsymbol{\omega} \equiv \nabla \times \mathbf{u}, \tag{2.5}$$

the nonlinear advective term in 2.2 can be rewritten to yield

$$\frac{\partial \mathbf{u}}{\partial t} + \nabla P = \mathbf{u} \times \boldsymbol{\omega} + \frac{1}{Re_b} \nabla \cdot \nabla \mathbf{u} + f \mathbf{e_z} \tag{2.6}$$

with

$$P \equiv p + \frac{\mathbf{u} \cdot \mathbf{u}}{2} \tag{2.7}$$

2.3 Numerical Method

2.3.1 Weak Form

Before the Navier-Stokes equations can be solved, they must be transformed in a way which is amenable to numerical procedures. Let $\mathbf{v}$ be the numerical approximation to $\mathbf{u}$, which will consist of a truncated expansion in terms of divergence-free vector functions (i.e. $\nabla \cdot \mathbf{v} = 0$), and let $\tilde{P}$ be the numerical approximation to P. Furthermore, let $\boldsymbol{\xi}$ be any vector function representable by an additional finite set of divergence-free vector functions ($\nabla \cdot \boldsymbol{\xi} = 0$). Spaces which encompass such functions can be written as

$$\mathcal{V} = \{\mathbf{v} \,|\, \mathbf{v} \in H^1(G), \nabla \cdot \mathbf{v} = 0 \text{ in } G,\ \mathbf{v} = 0 \text{ on } \Gamma_{R_2}\} \tag{2.8}$$

$$\mathcal{W} = \{\boldsymbol{\xi} \,|\, \boldsymbol{\xi} \in H^1(G), \nabla \cdot \boldsymbol{\xi} = 0 \text{ in } G,\ \boldsymbol{\xi} = 0 \text{ on } \Gamma_{R_2}\} \tag{2.9}$$

where Γ_{R_2} represent sthe surface $r = R_2$ (see fig. 2.1) and H^n is the Sobolev space of degree n. A function, say f, is said to belong to H^n if it possesses square-integrable derivatives up to order n (Hughes [13]), i.e.

$$\int_0^L \left(\frac{\partial^n f}{\partial x^n}\right)^2 dx < \infty \tag{2.10}$$

With $\mathbf{v} = 0$ on Γ_{R_2}, the no-slip boundary condition, $\mathcal{V}$ is specific to pipe flow. In general, boundary conditions of any type (Dirichlet, Neumann or mixed) could be built into $\mathcal{V}$; boundary conditions built in $\mathcal{V}$ are said to be imposed *strongly*. As long as Dirichlet boundary conditions are imposed strongly on functions in $\mathcal{V}$ (slip or no-slip), $\mathcal{W}$ will always retain the form 2.9, i.e. with $\boldsymbol{\xi} = 0$ on Γ_{R_2}. Functions in $\mathcal{W}$ must be homogeneous at the boundary if the pressure is to drop out of the formulation (more on this later).

To ensure that $\mathbf{v}$ and $\boldsymbol{\xi}$ are truely divergence-free, a standard result from calculus states that if the domain G is simply connected, then $\nabla \cdot \mathbf{v} = 0$ in G if and only if $\mathbf{v} = \nabla \times \boldsymbol{\Psi}$, where $\boldsymbol{\Psi}$ is a vector stream function associated with $\mathbf{v}$. So, if $\mathbf{v}$ is to

be continuous (C^0), then Ψ must at least be C^1 *. This means that second order, or quadratic b-splines are the lowest admissible order that can be used.

By substituting $\mathbf{v}$ for $\mathbf{u}$ in 2.1 and 2.6 and using the standard weighted residual technique which consist in taking the scalar product of the equation with a weight function and integrating over the domain, with $\boldsymbol{\xi}$ as the weight functions, the weak form of the Navier-Stokes equations is obtained †.

$$\left(\boldsymbol{\xi}, \frac{\partial \mathbf{v}}{\partial t}\right) + \left(\boldsymbol{\xi}, \nabla \tilde{P}\right) = \left(\boldsymbol{\xi}, (\mathbf{v} \times \boldsymbol{\omega})\right) + \frac{1}{Re_b}\left(\boldsymbol{\xi}, (\nabla \cdot \nabla \mathbf{v})\right) \tag{2.11}$$

where $\boldsymbol{\omega} = \nabla \times \mathbf{v}$ and the inner product $(\cdot, \cdot)$ is defined as

$$(\mathbf{a}, \mathbf{b}) \equiv \int_G \mathbf{a} \cdot \mathbf{b}\, dV \tag{2.12}$$

Since $\nabla \cdot \mathbf{v} = 0$ by construction, the continuity equation (2.1) drops out from the equation set. A further simplification is possible by eliminating the pressure from 2.11. First, by rearranging the pressure integral

$$\int_G \boldsymbol{\xi} \cdot \nabla \tilde{P}\, dV = \int_G \nabla \cdot (\tilde{P}\boldsymbol{\xi})\, dV - \int_G \tilde{P} \nabla \cdot \boldsymbol{\xi}\, dV \tag{2.13}$$

Then, applying the divergence theorem and using the fact that $\nabla \cdot \boldsymbol{\xi} = 0$ results in

$$\int_G \boldsymbol{\xi} \cdot \nabla \tilde{P}\, dV = \int_\Gamma \tilde{P}\boldsymbol{\xi} \cdot \mathbf{n}\, dS \tag{2.14}$$

where $\Gamma = \Gamma_0 \cup \Gamma_{L_z} \cup \Gamma_{R_2}$ and $\mathbf{n}$ is the unit normal vector. Using periodicity of all variables in the streamwise direction, any surface integral on $\Gamma_0 \cup \Gamma_{L_z}$ vanishes. With only the integral on Γ_{R_2} remaining, $\mathbf{n} = \mathbf{e_r}$, and since $\boldsymbol{\xi} \in \mathcal{W}$, 2.14 is identically zero. Hence, the weak form reduces to

$$\left(\boldsymbol{\xi}, \frac{\partial \mathbf{v}}{\partial t}\right) = \left(\boldsymbol{\xi}, (\mathbf{v} \times \boldsymbol{\omega})\right) + \frac{1}{Re_b}\left(\boldsymbol{\xi}, (\nabla \cdot \nabla \mathbf{v})\right) \tag{2.15}$$

*More formally, with Ψ lying in some space, say $\mathcal{P}$, one could write $\mathcal{P} = \{\Psi \mid \Psi \in H^2(G)\}$.

†Note that the body force term ($f\mathbf{e_z}$) was dropped from 2.11. In the code, the mass flow is held constant through a computational procedure described on page 130; the $f\mathbf{e_z}$ term is never actually computed.

By enforcing 2.15 for all $\boldsymbol{\xi} \in \mathcal{W}$ making up a basis for the weight functions, a coupled set of ordinary differential equations for the coefficients in the expansion for $\mathbf{v} \in \mathcal{V}$ are obtained, which can be solved using standard time-advance techniques. With the pressure eliminated and continuity satisfied, only two unknowns remain.

2.3.2 Velocity representation

Given the weak formulation 2.15, all that remains is to select the basis vectors to represent $\mathbf{v}$ and $\boldsymbol{\xi}$. Using periodicity in θ and z, allows the following representation to be adopted

$$\mathbf{v}(r,\theta,z,t) = \sum_j \sum_m \sum_{l=1}^{N_r} \alpha_{jml}(t)\mathbf{u}_l(r;k_\theta,k_z)e^{i(k_\theta\theta+k_z z)} \tag{2.16}$$

$$\boldsymbol{\xi}_{j'm'l'}(r,\theta,z) = \mathbf{w}_{l'}(r;k_\theta{}',k_z{}')e^{-i(k_\theta{}'\theta+k_z{}'z)} \tag{2.17}$$

where $\mathbf{u}_l$ are the basis expansion vectors and $\mathbf{w}_{l'}$ the basis weight vectors which are both function of r, k_θ and k_z, α_{jml} are the unknown (complex) expansion coefficients and

$$k_z = \frac{2\pi m}{L_z}, \quad -N_\theta/2 \le k_\theta = j \le N_\theta/2-1, \quad -N_z/2 \le m \le N_z/2-1$$

k_z and k_θ (or j) are respectively the streamwise and azimuthal wave numbers, and L_z is the period, or domain length, in the z direction.

Because $\mathbf{v}$ is a real valued quantity, only half of its Fourier coefficients need to be computed since there exists a symmetry of the coefficients such that $\hat{\mathbf{v}}_{-j,-m,l} = \hat{\mathbf{v}}^*_{j,m,l}$. From the standpoint of using this symmetry property, the choice of azimuthal wave numbers is purely arbitrary; instead, one could easily use symmetry of the axial wave numbers. But for the purpose of applying the regularity conditions (see below), using symmetry of the azimuthal wave numbers is the natural choice.

Substituting 2.16-2.17 in 2.15, the discrete form of the equations is obtained

$$\mathbf{A}\dot{\boldsymbol{\alpha}} = \mathbf{B}\boldsymbol{\alpha} + \mathbf{f}_{\mathrm{nl}} \tag{2.18}$$

where **A** and **B** are respectively the $N_r \times N_r$ mass and viscous matrices, defined as

$$\mathbf{A} = \{a_{l'l}\} = \int_0^{R_2} \mathbf{w}_{l'} \cdot \mathbf{u}_l \, r \, dr \tag{2.19}$$

$$\mathbf{B} = \{b_{l'l}\} = \frac{1}{Re_b} \int_0^{R_2} \mathbf{w}_{l'} \cdot \left(\widehat{\nabla} \cdot \widehat{\nabla} \mathbf{u}_l \right) \, r \, dr \tag{2.20}$$

where volume integrals were reduced to single integrals in r by the orthogonality property $\int_0^{2\pi} e^{im\phi} e^{-in\phi} d\phi = 2\pi\delta_{mn}$. Clearly, *the row index corresponds to the weight vectors* $\mathbf{w}_{l'}$, *and the column index to the expansion vectors* $\mathbf{u}_l$. Integrating the viscous matrix by parts yields

$$\mathbf{B} = -\frac{1}{Re_b} \left[\int_0^{R_2} \widehat{\nabla} \mathbf{w}_{l'} : \widehat{\nabla} \mathbf{u}_l \, r \, dr \; - \; R_2 \mathbf{w}_{l'}(R_2) \cdot \left. \frac{\partial \mathbf{u}_l}{\partial r} \right|_{R_2} \right] \tag{2.21}$$

where $\mathbf{a} : \mathbf{b}$ is the double contraction operator ($= a_{ij} b_{ij}$ in tensor notation) and $\widehat{\nabla}$ is the Fourier transformed del operator. $\mathbf{f_{nl}}$ is a vector of length N_r accounting for the nonlinear term. 2.18 is a linear set of ordinary differential equations for all combinations of k_θ, k_z wave numbers.

Regularity conditions

Because of the coordinate singularity that appears in the ∇ ($= \frac{\partial}{\partial r} \mathbf{e_r} + \frac{1}{r} \frac{\partial}{\partial \theta} \mathbf{e}_\theta + \frac{\partial}{\partial z} \mathbf{e_z}$) operator when written in cylindrical coordinates, special care must be taken to ensure that any quantity evaluated at the origin be bounded and smooth. Regularity conditions imply a set of requirements imposed on the velocity field; with the velocity field being C^∞, upon a transformation from cylindrical to cartesian coordinates, the origin of the cylindrical system should map smoothly as any other point would. The origin is not a special point.

Those conditions are the subject of appendix B. It is shown that regularity of the velocity field amounts to essentially two conditions: first, the radial and azimuthal velocity components are constrained to each other. Second, each velocity component must have a strictly defined behavior in r near the origin.

Vector shape functions

Within the confine of the regularity conditions, there is a great deal of freedom in constructing the expansion vectors. By choosing $\mathbf{w}_{l'}$ to be the complex conjugate of $\mathbf{u}_l$, a Galerkin method is obtained in 2.15. Galerkin's method has the advantages of minimizing the error in the L_2 norm and generating a positive definite mass matrix (see for example Stanaway *et al.*[45]).

With continuity satisfied and the pressure eliminated, only two degrees of freedom are associated with each Fourier/b-spline mode. Following the notation of Leonard and Wray [20], it is convenient to divide the expansion and weight vectors, $\mathbf{u}_l$ and $\mathbf{w}_{l'}$, into two distinct classes of vectors ($\mathbf{u}_l{}^+$ and $\mathbf{u}_l{}^-$) and ($\mathbf{w}_{l'}{}^+$ and $\mathbf{w}_{l'}{}^-$), with coefficients $\alpha^+_{jml}(t)$ and $\alpha^-_{jml}(t)$ respectively. The following vectors meet both regularity conditions, provided that g_l satisfy the appropriate conditions at $r = 0$

$$\mathbf{u}_l{}^+(r;k_\theta,k_z) = \begin{pmatrix} u_{r_l}{}^+ \\ u_{\theta_l}{}^+ \\ u_{z_l}{}^+ \end{pmatrix} = \widehat{\nabla} \times \begin{pmatrix} 0 \\ 0 \\ -k_z r g_l \end{pmatrix} = k_z \begin{pmatrix} -ik_\theta g_l \\ r g_l{}' + g_l \\ 0 \end{pmatrix} \tag{2.22}$$

$$\mathbf{u}_l{}^- = \widehat{\nabla} \times \begin{pmatrix} -ig_l \\ g_l \\ 0 \end{pmatrix} = \begin{pmatrix} -ik_z g_l \\ k_z g_l \\ g_l{}' + \frac{(1-k_\theta)}{r} g_l \end{pmatrix} \tag{2.23}$$

where $\widehat{\nabla}\times$ is the Fourier transformed curl operator, $g_l \equiv g_l(r)$ are the b-splines polynomials, and $g_l{}' = dg_l/dr$. The above representation is incomplete when $k_z = 0$, i.e. $v_r = v_\theta = 0$; in this case, the k_z factor is removed from 2.22 and 2.23 is left unchanged.

Because b-splines are polynomials of any order, they generally do not have the correct behavior in r near the origin. To remedy this, b-splines must be made to have a behavior analogous to the requirements B.8-B.10. The procedure by which this is achieved is the subject of appendix B. A summary of the expansion vectors is given in table B.1.

Upon splitting the vectors in two classes, the velocity becomes $\hat{\mathbf{v}}_{jml} = \alpha^+_{jml}\mathbf{u}_l{}^+ +$

$\alpha^-_{jml}\mathbf{u}_l{}^-$ and 2.18 is composed of the following

$$\mathbf{A}^+_+\dot{\boldsymbol{\alpha}}^+ + \mathbf{A}^-_+\dot{\boldsymbol{\alpha}}^- = \mathbf{B}^+_+\boldsymbol{\alpha}^+ + \mathbf{B}^-_+\boldsymbol{\alpha}^- + \mathbf{f}_{\rm nl}{}^+ \quad (2.24)$$

$$\mathbf{A}^-_-\dot{\boldsymbol{\alpha}}^- + \mathbf{A}^+_-\dot{\boldsymbol{\alpha}}^+ = \mathbf{B}^-_-\boldsymbol{\alpha}^- + \mathbf{B}^+_-\boldsymbol{\alpha}^+ + \mathbf{f}_{\rm nl}{}^- \quad (2.25)$$

where

$$\mathbf{A}^+_+ = \int_0^{R_2} \mathbf{w}_{l'}{}^+ \cdot \mathbf{u}_l{}^+ \, r\, dr \qquad \mathbf{A}^+_- = \int_0^{R_2} \mathbf{w}_{l'}{}^- \cdot \mathbf{u}_l{}^+ \, r\, dr \quad (2.26)$$

$$\mathbf{A}^-_- = \int_0^{R_2} \mathbf{w}_{l'}{}^- \cdot \mathbf{u}_l{}^- \, r\, dr \qquad \mathbf{A}^-_+ = \int_0^{R_2} \mathbf{w}_{l'}{}^+ \cdot \mathbf{u}_l{}^- \, r\, dr \quad (2.27)$$

and similarly for the viscous matrices. Appendix C gives the complete details on how the discrete system of equations is assembled and each matrix is defined.

2.3.3 Nonlinear Term

As it appears in 2.24 and 2.25, the nonlinear term is defined as

$$\mathbf{f}_{\rm nl}{}^\pm = \{f^\pm_{{\rm nl}\,l'}\} = \frac{1}{2\pi L_z}\int_0^{L_z}\int_0^{2\pi}\int_0^{R_2} \mathbf{w}_{l'}{}^\pm \cdot (\mathbf{v}\times\boldsymbol{\omega})\, e^{-i(k_\theta{}'\theta + k_z{}'z)}\, r\, dr\, d\theta\, dz \quad (2.28)$$

This term is computed in the standard way using the so-called pseudo spectral approach, where the product $\mathbf{w}_{l'}{}^\pm \cdot (\mathbf{v}\times\boldsymbol{\omega})$ is computed in physical space by means of fast Fourier transforms (FFT) and the final result given by the inverse transform (the integral $\frac{1}{2\pi L_z}\int_0^{L_z}\int_0^{2\pi}\cdots e^{-i(k_\theta{}'\theta+k_z{}'z)}\,d\theta\,dz$ is the very definition of the inverse Fourier transform). By using FFT, the pseudo spectral method has the advantage of requirering fewer operations than the full spectral approach: typically, the pseudo spectral approach requires $\sim N\log_2 N$ operations, whereas the full spectral approach requires $\sim N^2$ operations. Fourier transforms are done using the 3/2 rule to avoid any aliasing errors. Problems related to aliasing errors have been well documented and are not repeated here (see Rogallo [37], Canuto *et al.* [7] and Sondergaard [42] for background). Numerical errors in the radial direction are alleviated by computing all integrals to machine accuracy by using Gauss quadrature technique. Specific details on how this procedure was implemented are given in appendix C.

2.3.4 Time Advance

The time advancement method used to compute the time derivative in 2.18 is the so-called SMR method (see Spalart *et al.* [44]), which is a mixed explicit–implicit method; it uses a third order Runge-Kutta (RK) method for the explicit part and a trapezoidal (second order), or Crank-Nicholson, method for the implicit part. An equation to be time marched is split into a linear and a nonlinear part

$$\frac{\partial \Phi}{\partial t} = L(\Phi) + N(\Phi) \tag{2.29}$$

where $L(\Phi)$ is the linear term which consists of the viscous term and $N(\Phi)$ is the nonlinear convective term. The method to advance Φ_n at time t to Φ_{n+1} at time $t + \Delta t$ is given by

$$\Phi' = \Phi_n + \Delta t[L(\alpha_1\Phi_n + \beta_1\Phi') + \gamma_1 N(\Phi_n)] \tag{2.30}$$

$$\Phi'' = \Phi' + \Delta t[L(\alpha_2\Phi' + \beta_2\Phi'') + \gamma_2 N(\Phi') + \zeta_1 N(\Phi_n)] \tag{2.31}$$

$$\Phi_{n+1} = \Phi'' + \Delta t[L(\alpha_3\Phi'' + \beta_3\Phi_{n+1}) + \gamma_3 N(\Phi'') + \zeta_2 N(\Phi')] \tag{2.32}$$

where

$$\alpha_1 = \frac{29}{96}, \quad \alpha_2 = -\frac{3}{40}, \quad \alpha_3 = \frac{1}{6}$$

$$\beta_1 = \frac{37}{160}, \quad \beta_2 = \frac{5}{24}, \quad \beta_3 = \frac{1}{6}$$

$$\gamma_1 = \frac{8}{15}, \quad \gamma_2 = \frac{5}{12}, \quad \gamma_3 = \frac{3}{4}, \quad \zeta_1 = -\frac{17}{60}, \quad \zeta_2 = -\frac{5}{12}$$

Even though this method requires two previous levels of storage, it can be made to require only one previous level of storage (details are in given in section C.4).

Stability and Accuracy

The advantage of treating the viscous term with an A-stable implicit method is to relieve the time constraint, since it is customary to ignore the implicit part of the

equation when establishing that constraint. Consider the following linear model problem

$$\frac{\partial \Phi}{\partial t} + \mathbf{u} \cdot \nabla \Phi = 0 \tag{2.33}$$

Assuming that Φ is periodic in all three directions, 2.33 becomes

$$\frac{\partial \Phi}{\partial t} + i \left(u_r k_r + u_\theta \frac{k_\theta}{r} + u_z k_z \right) \Phi = 0 \tag{2.34}$$

For the third order Runge-Kutta scheme the CFL number is $\sqrt{3}$, and the stability criterion is given as

$$\Delta t \leq \frac{\sqrt{3}}{|\lambda_{\max}|} \tag{2.35}$$

with

$$|\lambda_{\max}| \equiv \max \left| u_r k_r + u_\theta \frac{k_\theta}{r} + u_z k_z \right| \tag{2.36}$$

using the triangle inequality

$$\leq \max \left(|u_r| k_r + |u_\theta| \frac{k_\theta}{r} + |u_z| k_z \right) \tag{2.37}$$

$$\leq \max \left(|u_r| \frac{\pi}{\Delta r} + |u_\theta| \frac{k_{\theta \max}}{r} + |u_z| k_{z \max} \right) \tag{2.38}$$

where $k_{\theta \max} = N_\theta/2 - 1$ and $k_{z \max} = \frac{2\pi}{L_z}(N_z/2 - 1)$ and $k_{r_{\max}} = \frac{2\pi}{R_2}\frac{N_r}{2} = \frac{\pi}{\Delta r}$ with $\Delta r = R_2/N_r$.

Since maximizing λ guarantees stability, assuming periodicity of the radial direction yields a conservative estimate. Figure 2.2 shows a plot of the modified (or numerical) wave number versus the exact value. It is clear that the b-spline approximation, in the context of a Galerkin method, yields wave numbers always less than, or equal to the exact value.

Having ensured the solution is well behaved at the origin (through the imposition of the regularity conditions), a problem still remains near the origin. This problem is best explained by considering a grid in physical space. In the example of figure 2.3, the mesh on the left shows a concentration of grid point as the radius decreases; this would lead to a highly restrictive time step since the value of $r\,\Delta\theta$ becomes very

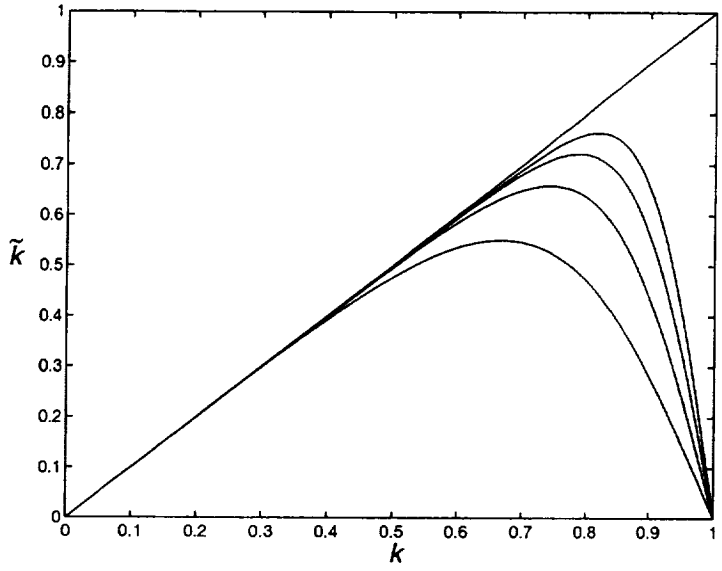

Figure 2.2: Modified wave number ($\tilde{k}$) versus wave number (k) normalized by $k_{\max}$, for splines of orders 1 through 4. The straight line is the spectral limit (exact) and higher order are closer to spectral.

small near the origin. To alleviate this, grid points should be removed to keep the value of $r\,\Delta\theta$ approximately constant. Since no special feature (such as a boundary layer) exists near the center, there is no need for the added resolution.

In the present context, i.e. using a Fourier representation for the azimuthal direction, such a procedure would translate into letting the maximum azimuthal wave number vary with the radial position, such that the ratio $k_{\theta\max}/r$ appearing in 2.38 be approximately constant. Because b-splines have local support, splines for larger values of k_θ can be removed near the center of the pipe, while leaving the ones on the outer region. This procedure is termed *modal reduction*. In order for the ratio $k_{\theta\max}/r$ to be constant, k_θ has to be made a function of r[‡]; the following was adopted

$$k_{\theta\max}(r) = (k_{\theta\max} - b)\frac{r}{R_2} + b \qquad \text{for } 0 < r \leq R_2 \tag{2.39}$$

[‡]Making k_θ a function of r complicates the computation of the nonlinear term since Fourier transforms must be done on fixed lengths. Even though this is not a problem in principle the implementation of modal reduction in the context of FFT is not trivial. Details are given in section C.2

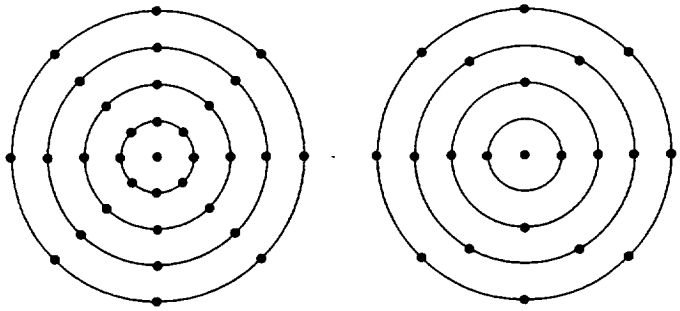

Figure 2.3: Mesh (left) with constant number of grid points on each radial location. Mesh (right) with constant $r\,\Delta\theta$ between grid points.

where $k_{\theta\max} = N_\theta/2 - 1$ and b is set to some small value (2 or 3). At $r = 0$ there is only a single non-zero Fourier mode ($k_\theta = 0$ for u_z and $k_\theta = 1$ for u_r and u_θ). The modal reduction algorithm can be written as

$$\alpha_{jml_i} = 0 \qquad j \geq k_{\theta\max}(r_i) + 1 \tag{2.40}$$

and l_i are splines with support on $r \leq r_i$. Finally, the CFL condition is given as

$$\Delta t \leq \frac{\sqrt{3}}{\max_i \left(|u_{r_i}| \frac{\pi}{\Delta r_i} + |u_{\theta_i}| \frac{k_{\theta\max}(r_i)}{r_i} + |u_{z_i}| k_{z\max} \right)} \tag{2.41}$$

where all velocities are evaluated in physical space. The time step can be evaluated while the nonlinear term is being computed since it too requires velocities in physical space.

Running with the full CFL number was found to be both stable and accurate. In addition to alleviating the CFL condition, modal reduction greatly reduces the computations; typically, when modal reduction is active, the computations take 30% less time than with the full, unreduced modes.

2.4 Computer Code

The method described in this work was coded to run on the vector-parallel CRAY C90 super computer. The computer used had 64 MW[§] of available memory and eight processors. To save memory, the code was designed to take advantage of the solid-state storage device (SSD), a very high speed ram disk. The code was written in *VECTORAL*, a computer language designed by Wray [51] to ease implementation of vector processing and facilitate the handling of large datasets. Two versions of the code were written: one serial (single CPU) and one parallel (some subroutines of the parallel version are written in C). Parallelization was straightforward in the context of the numerical method and the shared memory architecture of the computer. Both are highly optimized to take advantage of vectorization. The serial version runs at 600 MFlops and the parallel runs at roughly 500 MFlops/CPU, depending on system load. Running a grid of $72 \times 160 \times 192$ ($N_r \times N_\theta \times N_z$) with fourth order splines, the serial code needed 16 MW of memory. For sake of comparison, the code runs at 14 μsec/mode/RK sub-step when using cubic splines (without modal reduction), whereas the mixing layer code of Spalart *et al.* [44] achieves 13 μsec/mode/RK sub-step using Jacobi polynomials instead of b-splines.

The code is divided in two principal subroutines called passes: the first pass consist in computing the nonlinear term; it accounts for 85% of the computations. The second pass advances the solution to the next time step. The order of execution is given as follows

- **Pass 1**

  1. Unload the data from database (SSD).
  2. Reorder the data and zero the oddball wave number ($k_z = -N_z/2$) in preparation for the fast Fourier transforms (FFT).
  3. Compute A_l–K_l (see section C.2 for the definitions of those terms) and transform (FFT) to physical space.

[§]MW = mega word, 1 word = 8 bytes.

4. If first RK sub-step, compute the maximum eigenvalue and update the time step (Δt).
5. Compute $\gamma_{l'}^{+}$, $\beta_{l'}^{-}$, $\Upsilon_{l'}^{-}$, $\tilde{\Upsilon}_{l'}$ and $\tilde{\delta}_{l'}$ and FFT to Fourier space.
6. Obtain the result $\mathbf{f}_{\mathbf{nl}l'}^{+}$ and $\mathbf{f}_{\mathbf{nl}l'}^{-}$.
7. Save the result to the database.
8. Proceed to pass 2.

- **Pass 2**

1. Unload the result from pass 1 and the previous step variable from the database.
2. Impose the regularity and boundary conditions on the results of pass 1.
3. Compute the mass and viscous matrices ($\mathbf{A}$ and $\mathbf{B}$).
4. Compute the effective mass and viscous matrices ($\widetilde{\mathbf{A}}$ and $\tilde{\mathbf{B}}$).
5. Impose the regularity and boundary conditions.
6. If first RK sub-step, do some run-time diagnostics.
7. Time march (see section C.4 for the exact details).
8. Save the results to the database.
9. Proceed to pass 1.

2.5 Boundary and Initial Conditions

2.5.1 Boundary Conditions

The no-slip boundary conditions, where $\mathbf{v} = 0$ on $r = R_2$ (see 2.8) is used to simulate pipe flow. Applying those conditions to the functions given in table B.1, constrains the expansion coefficients which have support on $r = R_2$. The resulting conditions are given in table 2.1.

Table 2.1: Expansion coefficients for the no-slip boundary conditions.

	$k_\theta = 0$	$k_\theta > 0$
$k_z = 0$	$\alpha^+_{N_r} = 0$ $\alpha^-_{N_r} = 0$	$\alpha^+_{N_r-1} = \alpha^+_{N_r} = 0$ $\alpha^-_{N_r-1} = \alpha^-_{N_r} = 0$
$k_z \neq 0$	$\alpha^+_{N_r} = 0$ $\alpha^-_{N_r-1} = \alpha^-_{N_r} = 0$	$\alpha^+_{N_r-1} = \alpha^+_{N_r} = 0$ $\alpha^-_{N_r-1} = \alpha^-_{N_r} = 0$

In all cases, the support rules given in section A.3 were used to derive the conditions of table 2.1. A consequence of those boundary conditions is for $\frac{\partial u_r}{\partial r}\Big|_{R_2} = 0$, which is required by continuity.

2.5.2 Initial Conditions

As mentioned in the introduction, pipe flow is linearly stable to infinitesimal disturbances; the onset of turbulence can only be brought about by nonlinear interactions. This implies the flow cannot be started with unstable modes in order to trigger transition and bring about the onset of turbulence as rapidly as possible. The flow was started with a mean velocity profile, or (0,0) mode, given by $1 - r^8$, and with the rest of the modes filled with noise with an amplitude of $\approx 10\%$ of the mean. This amplitude was found to be more than adequate to excite the nonlinear process.

2.6 Validation

Three different approaches were used to validate the code: representation tests using known velocity fields, solution to Stokes' problem and the propagation of linear Orr-Sommerfeld waves. Each approach serves a different purpose and is explained below.

2.6.1 Representation Tests

The objective of this first test is to ensure that the method was implemented correctly (validation of the method proper is left for subsequent tests). The idea behind this

test is quite simple: use an arbitrary function instead of b-splines representations ($\sum_l \alpha_l^{\pm} g_l$) in the expansion vectors (table B.1) to generate a benchmark result; then check that solution against the one obtained by b-splines. The coefficients ($\alpha_l^{\pm}$) used for the b-splines solution are generated using the projection procedure shown in A.1–A.5. Those tests can be done to verify the mass and viscous matrices, and the nonlinear term; they are repeated for all four families of expansion vectors. The arbitrary function should satisfy the boundary condition and be regular (possess the correct power of r). As an example, one could use

$$f(r; k_\theta, k_z) = r^{|k_\theta - 1|}(1 - r^2)^2 \tag{2.42}$$

where it is assumed $R_2 = 1$.

2.6.2 Stokes Flow

Once the implementation of the method is validated, we turn our attention to the validation of the method itself. To validate the method, we make use of Stokes' problem for which there is an exact solution (see appendix D). The objective is to solve numerically Stokes eigenvalues and eigenfunctions and compare them to the exact solution. The relevance of solving Stokes eigenproblem was best explained by Hughes [13] (p. 434): "The accuracy of the eigenvalues and eigenfunctions are measures of the quality of both **M** and **K** [¶], in other words, the entire spatial discretization."

Hughes [13] gives the following error estimates for eigenvalues and eigenfunctions computed using Galerkin's method when solving an elliptic eigenvalue problem (of degree one)

$$\tilde{\lambda}_s - \lambda_s \leq c h^{2S} \lambda_s^{S+1} \tag{2.43}$$

$$\| \mathbf{v}_s - \mathbf{u}_s \|_0 \leq c h^{S+1} \lambda_s^{(S+1)/2} \tag{2.44}$$

where h is the mesh size parameter, c is a constant independent of h or λ_s, $\| \cdot \|_0$ is the L_2 norm and $0 < \lambda_1 < \lambda_2 < \ldots$; both $\tilde{\lambda}_s$ and $\mathbf{v}_s$ are the numerical approximations.

[¶] i.e. **A** and **B**, the mass and viscous matrices

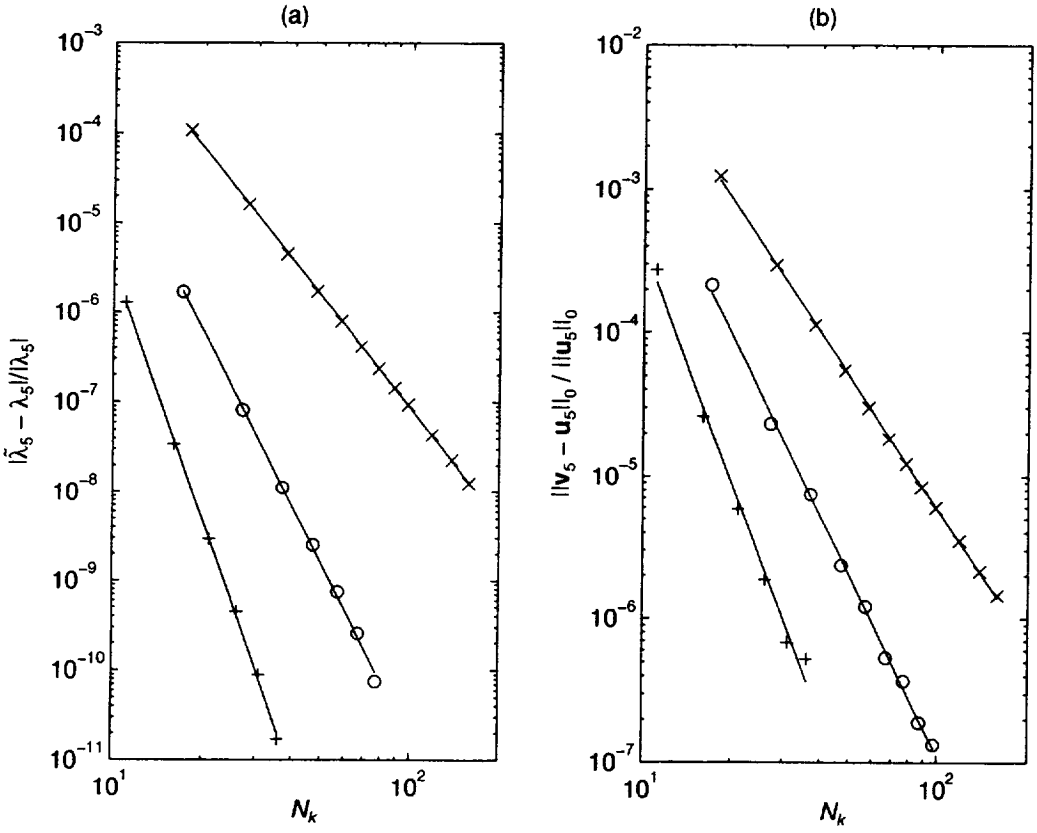

Figure 2.4: Convergence plots for the Stokes eigenvalues (a) and eigenfunctions (b) on an equispaced grid with N_k knots, for $k_\theta = 2$, $k_z = 2\pi$ and $s = 5$. Plots are for cubic $\times$, quartic o and quintic + b-splines.

Figure 2.4 gives relative errors for the fifth eigenvalue and eigenfunction for $k_\theta = 2$ and $k_z = 2\pi$; plots for other combination of wave numbers are included for completeness and given on figure 2.7, page 30. As expected, errors for the eigenvalues are much lower then their eigenfunctions equivalent since as shown in 2.43 and 2.44, eigenvalues converge faster than eigenfunctions (exponent of h). Eigenvalue errors quickly reach round-off levels for higher degree splines and moderate values of N_k (the number of knots).

Slopes of each curve represent the convergence rates and are given in table 2.2. Computed rates are always bounded from below by the estimates 2.43–2.44, and the agreement between them is very good. Preserving the full rate of convergence gives

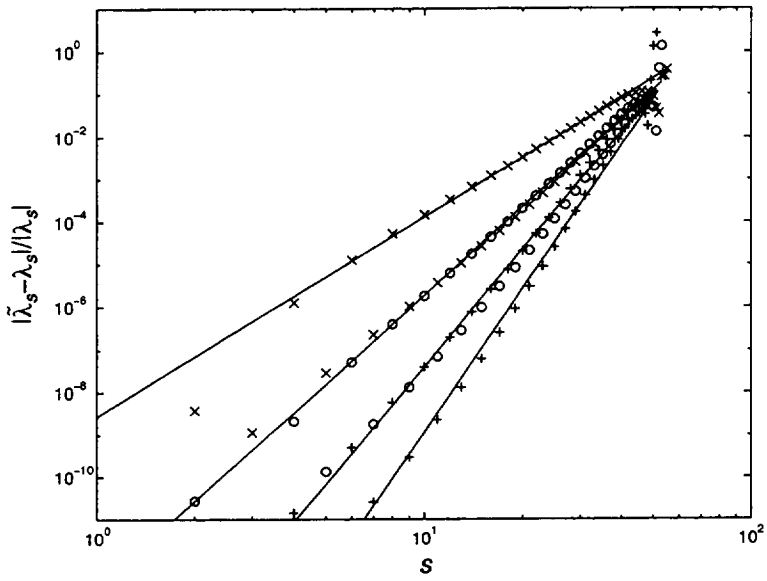

Figure 2.5: Relative error in eigenvalue for $N_r = 30$, $k_\theta = 0$ and $k_z = 2\pi$. Symbols are as figure 2.4

a strong indication that the computations are behaving as expected.

Table 2.2: Convergence rates for $k_\theta = 2$, $k_z = 2\pi$.

	Eigenvalues		Eigenfunctions	
S	computations	(2.43)	computations	(2.44)
3	4.14	4	3.11	3
4	6.50	6	4.21	4
5	9.34	8	5.42	5

Because the expansion functions as defined in table B.1 involve derivatives of b-splines, with a b-spline of degree S, the method will converge at the rate of a spline of degree $S-1$; this should not be surprising since the q^{th} derivative of a b-spline a degree S can be represented by a b-spline of degree $S-q$. This explains the discrepancy one might observe between the estimates 2.43–2.44 and the values of table 2.2.

This behavior is best observed in the expansion functions for $k_\theta = 0$ and $k_z > 0$: the $\mathbf{u}_l^-$ vector involves a derivative of a b-spline whereas $\mathbf{u}_l^+$ does not. For this case,

the plus and minus modes should converge at different rates. Figure 2.5 clearly shows this behavior: the plus mode of the cubic spline converges at the same rate as the minus mode of the quartic. Figures 2.7 (e) and (f) show that for the (0,0) modes, convergence is much faster since these expansion functions involve no derivative of b-splines. So, every derivative incurs a loss of an order of accuracy. Figure 2.5 also shows an interesting consequence of the estimates 2.43-2.44. Because the eigenvalue λ_s appears on the right hand side of the estimates, when the eigenvalue becomes large the error follows accordingly; with s large, the error becomes $O(1)$.

2.6.3 Wave propagation

The last test consists in propagating Orr-Sommerfeld waves. The objectives are to validate the time marching method, and the computation of the nonlinear term. It also ensures that the code as a whole is working properly, such as access to the SSD and other I/O.

The idea is to start the computations from a solution to the linearized Navier-Stokes equations for an arbitrary wave number pair (k_θ, k_z); such solution is known as an Orr-Sommerfeld wave (see appendix D) and is given by D.19. This wave is then propagated using the standard Navier-Stokes solver. If the amplitude of this wave is small enough, it should behave linearly such that the solution at any given time is

$$\hat{\mathbf{u}}(r,t;k_\theta,k_z) = \varepsilon\hat{\mathbf{u}}(r,0;k_\theta,k_z)e^{-i\omega t} \tag{2.45}$$

where ε is a small number chosen to be 10^{-6}.

Figure 2.6 gives the error norms for the four different wave number pairs after having propagated for fifty time steps. The linear growth of the error in time for plots (a)–(c) is in agreement with the predicted error, which has a form

$$|e(t_n)| = c\Delta t^2 t_n + O(\Delta t^3) \tag{2.46}$$

where c is a constant independent of Δt, and $t_n = n\Delta t$. 2.46 implies that if Δt is small enough, so higher order terms become negligible, the error will grow linearly in

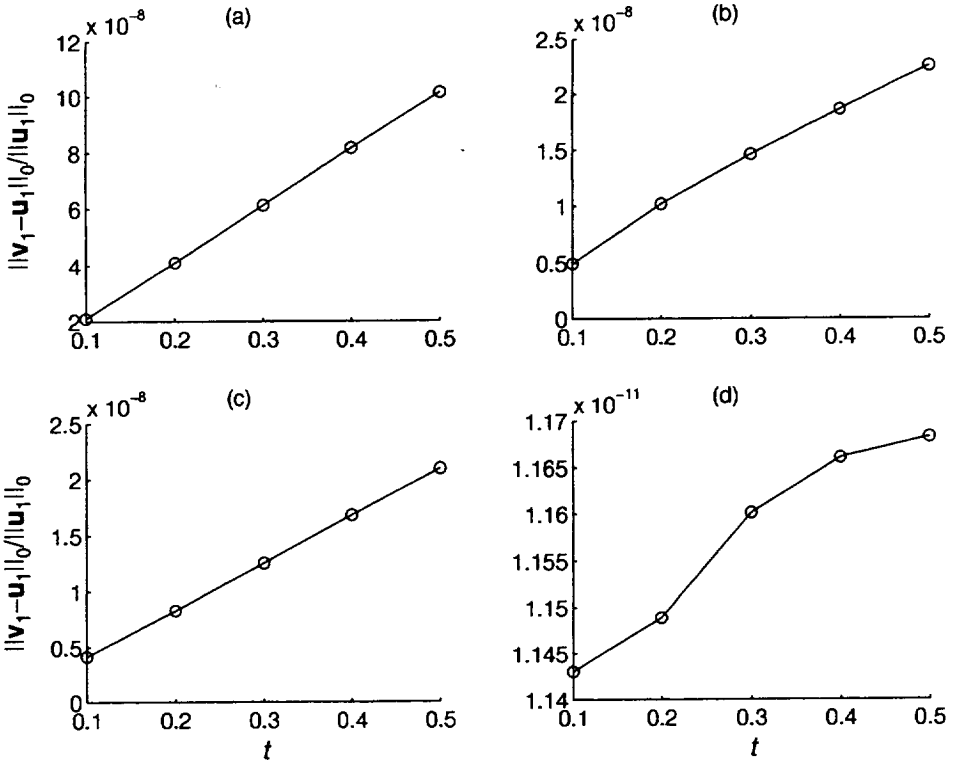

Figure 2.6: Relative L_2 error norm of the Orr-Sommerfeld wave for the four different wave number pairs (k_θ, k_z): (a) (1,1); (b) (1,0); (c) (0,1) and (d) (0,0). Parameters are $Re_b = 9600$, $N_r = 35$, $S = 3$, $N_\theta = N_z = 12$ for a $CFL = 0.05$.

a finite time. In absolute terms, the low error is also an indication that the nonlinear term is behaving as expected by preserving linearity of the solution. Plot (d) is a simple measure of how well the mean flow is preserved, since the nonlinear term has zero contribution for the (0,0) mode; the error is no larger than round-off.

Lastly, it was possible to observe an additional wave or alias at $(2k_\theta, 2k_z)$ with amplitude $O(\varepsilon^2)$ being generated by the nonlinear term. This is not unexpected since the product $\mathbf{v} \times \boldsymbol{\omega}$ will generate a term with an exponential of the form $e^{2k_\theta + 2k_z}$. This is further evidence that the nonlinear term is behaving as it should. To make this alias disappear, we could have selected a smaller initial amplitude such that ε^2 would be of the same order as round-off.

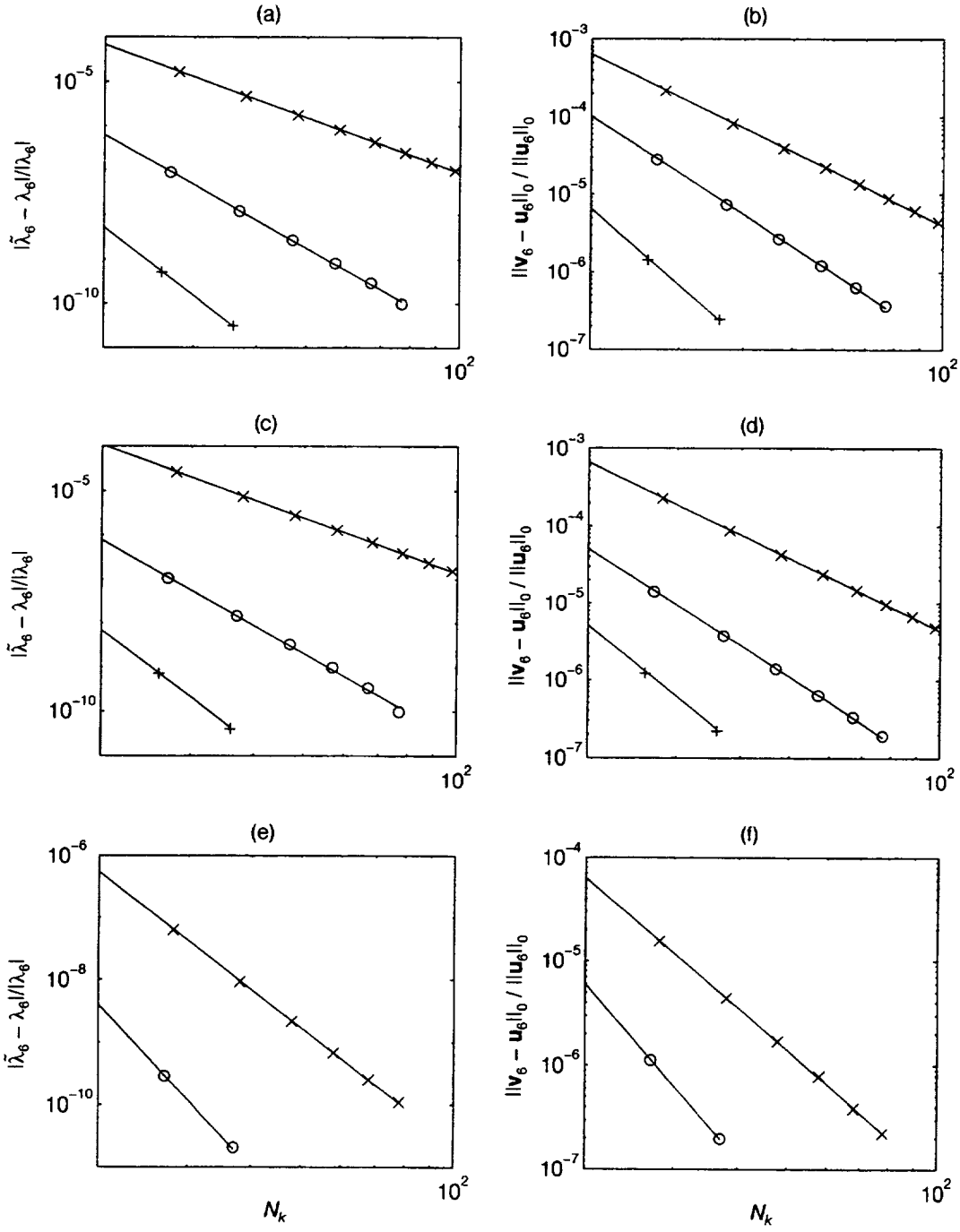

Figure 2.7: Convergence plots for the other families of expansion functions (k_θ, k_z) for (respectively) eigenvalues and eigenfunctions: (a)-(b) $(0, 2\pi)$, (c)-(d) (1,0), (e)-(f) (0,0). Symbols are as for figure 2.4.

Chapter 3

Pipe Flow

We present in this chapter results for the pipe flow simulation. The following results were obtained using the method described in chapter 2. The pipe flow simulation of Eggels *et al.* [12] (hereinafter referred to as EUW), the channel flow simulation of Kim, Moin and Moser [17] (KMM), the PIV (Particle Image Velocimetry) and LDA (Laser Doppler Anemometry) measurements in pipe flow of Westerweel *et al.* [50] (WDV), and the high resolution LDA measurements (also in pipe flow) of Durst, Jovanović and Sender [11] (DJS); all were used to compare with the present results.

3.1 Test Case

In wanting to keep within the same Reynolds number range as the aforementioned investigators, the Reynolds number based on the bulk velocity, U_b, and pipe diameter, D, was set to $Re_b = U_b D/\nu = 5600$ (or a Reynolds number of $Re_\tau = 380$ based on the wall shear velocity u_τ). This value matches KMM's value of 5600 based on the mean velocity and channel width (or $Re_\tau = 360$), and is close to EUW's value of 5300 ($Re_\tau = 360$) based on U_b and D. The computations were carried out on a grid of $72 \times 160 \times 192$ ($N_r \times N_\theta \times N_z$), for a total of 2.2 million Fourier/b-splines modes (less if we account for modal reduction) with quartic b-splines. The length of the domain, L_z, was chosen to be $5D$, the same as EUW; the adequacy of the spatial resolution and L_z will be assessed later by examining the velocity and vorticity spectra, and the

streamwise two-point correlations. With this computational domain, grid spacings are about $R_2\Delta\theta^+ \approx 7.5$ and $\Delta z^+ \approx 9.9$ wall units*. A non-uniform grid is used in the radial direction based on an exponential function: close to the wall the radial grid spacing is smaller, with the first point away from the wall located at $r^+ \approx 0.39$; spacing reaches its maximum near the center with $\Delta r^+ \approx 5.7$. Very close to the center, a finer radial grid is used in order to impose the regularity conditions; a finer grid makes this process more local.

Those values compare well with EUW who used $96 \times 128 \times 256$ grid points with an equispaced mesh in the radial direction. The first point away from the wall was located at $r^+ = 0.94$, with the rest spaced by $\Delta r^+ \approx 1.88$. Other grid spacings were $R_2\Delta\theta^+ \approx 8.84$ (at the wall) and $\Delta z^+ \approx 7$. Since EUW do not remove azimuthal modes as the radius decreases, the azimuthal resolution varies linearly with r and reaches a minimum of 0.05 wall units near the centerline. Even though the total number of grid points exceeds the one used for our present simulation, EUW's resolution must be considered at par if not inferior to the present one: since EUW's computational procedure is based on second order finite differences, which possesses a high diffusivity compared with the present technique, many more grid points must be used to adequately represent the small scales. EUW's choice of a uniform grid in the radial direction is certainly questionable.

KMM's computations used $192 \times 129 \times 160$ modes in the streamwise, crosstream and spanwise directions (y, y, z) respectively. KMM's grid spacings were $\Delta x^+ \approx 12$ and $\Delta z^+ \approx 7$. The channel had a length of $2\pi D$ (versus $5D$ for the pipe) and a spanwise length of πD, where D is the channel width, or distance between walls. The crosstream, or y direction, was discretized with a cosine grid (necessary for Tchebyshev approximation) with the first point away from the wall located at $y^+ \approx 0.05$, reaching a maximum spacing of 4.4 at the center. Their near wall resolution is almost an order of magnitude smaller than the value adopted for the present simulation. There appears to be very little advantage in using such a fine resolution since the

*the + superscript refers to nondimensionalization with respect to wall variables, mainly the wall shear velocity $u_\tau^2 = (\tau_w/\rho) = -\nu\, \partial\bar{u}_z/\partial r|_{R_2}$; e.g. $r^+ = r u_\tau/\nu$.

viscous sublayer is usually of order $y^+ = 5^\dagger$. The only apparent reason for this, is an attempt to resolve numerical artifacts produced near the boundary (so-called *projection error*; see Moser and Moin for background [25]). Because of the cost involved and the lack of additional physical insight gained by such a fine grid, no attempt was made to duplicate their resolution.

3.2 Turbulence Statistics

The results presented in this section are comprised of 46 different fields approximately equispaced in time, averaged over a period of 43 time units (based on the non-dimensional time D/U_b). The results of EUW consist of 41 fields averaged over a period of 59 time units. Although 40 time units might not be ideal to remove all statistical errors, it is certainly adequate. Statistical steady-state is reached when the total shear stress $\tau_{rz} = 1/Re_b \partial \bar{u}_z/\partial r - \overline{u_r' u_z'}$ becomes a linear function of r. If τ_{rz} is normalized by τ_w, then $\partial \tau_{rz}^+/\partial r = 1$. Defining the deviation from linearity as $\|\tau_{rz}^+ - r\|_0/\|r\|_0$, the deviation for the present simulation is 0.51%, and for the DNS of EUW, 0.72%.

3.2.1 Mean flow

Table 3.1 compares several mean flow parameters reported by various investigators to the results from the present computation. Of interest, is the friction coefficient defined as

$$C_f = 2\left(\frac{u_\tau}{U_b}\right)^2 \tag{3.1}$$

The computed value of 9.16×10^{-3} agrees within half a percent of Blasius' empirical formula. Differences between the present simulation and EUW values for C_f, the displacement thickness δ, and the momentum thickness θ, are consistent with expected dependence on Reynolds number (with the Reynolds number increasing, those values should decrease). Differences in geometry between the pipe and channel are also

†For the pipe, y^+ is defined as $y^+ = (R_2 - r)u_\tau/\nu$.

Table 3.1: Mean flow properties from several investigators. Repeated in modified form from EUW.

	b-splines	DNS (EUW)	PIV (WDV)	LDA (WDV)	HWA (EUW)	DNS (KMM)
Re_c[a]	7248	6950	7100	7200	7350	6600
Re_b	5600	5300	5450	5450	5600	5600
Re_τ	380	360	366	371	379	360
U_c/u_τ	19.11	19.31	19.38	19.39	19.40	18.20
U_b/u_τ	14.77	14.73	14.88	14.68	14.76	15.63
U_c/U_b	1.29	1.31	1.30	1.32	1.31	1.16
$C_f(\times 10^{-3})$	9.16	9.22	9.03	9.28	9.18	8.18
$C_{f_{\text{bla}}}(\times 10^{-3})$[b]	9.13	9.26	9.19		9.13	8.44[c]
$C_{f_{\text{bar}}}(\times 10^{-3})$[d]	9.36	9.51	9.43		9.36	–
δ/R_2[e]	0.121	0.127	0.124	0.130	0.128	0.141
θ/R_2[f]	0.066	0.068	0.068	0.071	0.070	0.087
$H = \delta/\theta$	1.84	1.86	1.83	1.83	1.82	1.62
G[g]	8.74	8.91	8.78	8.79	8.73	6.97

[a] All Reynolds numbers are based on D, the pipe diameter or channel width, and ν.
[b] Friction coefficient based on Blasius' formula $C_{f_{\text{bla}}} = 0.079 Re_b^{-0.25}$.
[c] Based on Dean's correlation $C_f = 0.073 Re_b^{-0.25}$ (from KMM).
[d] Friction coefficient based on Barenblatt's hypothesis (see page 38).
[e] The displacement thickness δ is defined as $\delta(2R_2 - \delta) = 2\int_0^{R_2} (1 - \bar{u}_z(r)/U_c)\ r\,dr$ (EUW).
[f] The momentum thickness θ is defined as $\theta(2R_2 - \theta) = 2\int_0^{R_2} \bar{u}_z(r)/U_c\,(1 - \bar{u}_z(r)/U_c)\ r\,dr$.
[g] $G = U_c/u_\tau((H-1)/H)$.

apparent; for a similar Re_τ, the channel has a significantly lower friction coefficient, with larger δ and θ.

Figure 3.1 shows the mean velocity and vorticity profiles. Agreement with EUW and the experiments of WDV is excellent. The slight bulge in the velocity profile for $0.3 \leq r \leq 0.8$ compared to EUW is due to a slightly higher Reynolds number in our case, which causes the velocity profile to be fuller. As expected, the mean vorticity is maximum at the wall and drops to zero at the center, indicative of a vortex sheet in the near-wall region.

Figure 3.2 (a,b) shows the mean velocity profile normalized by the wall shear stress velocity compared to the experimental data of WDV, and the results from EUW and KMM simulations. Figure 3.2 (a) reveals good agreement between the experiments

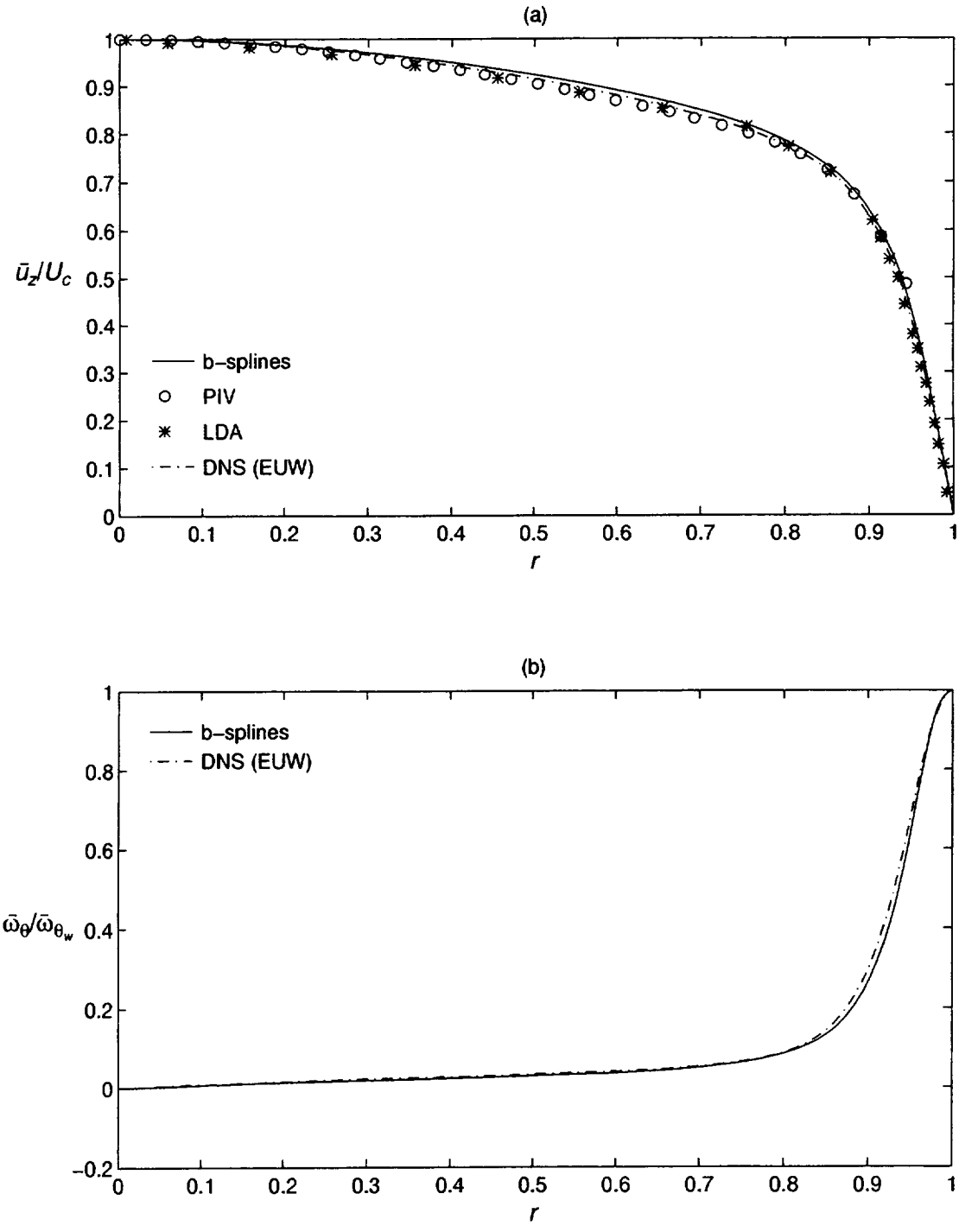

Figure 3.1: Mean profiles: (a) streamwise velocity normalized by the centerline velocity; (b) azimuthal vorticity normalized by the vorticity at the wall.

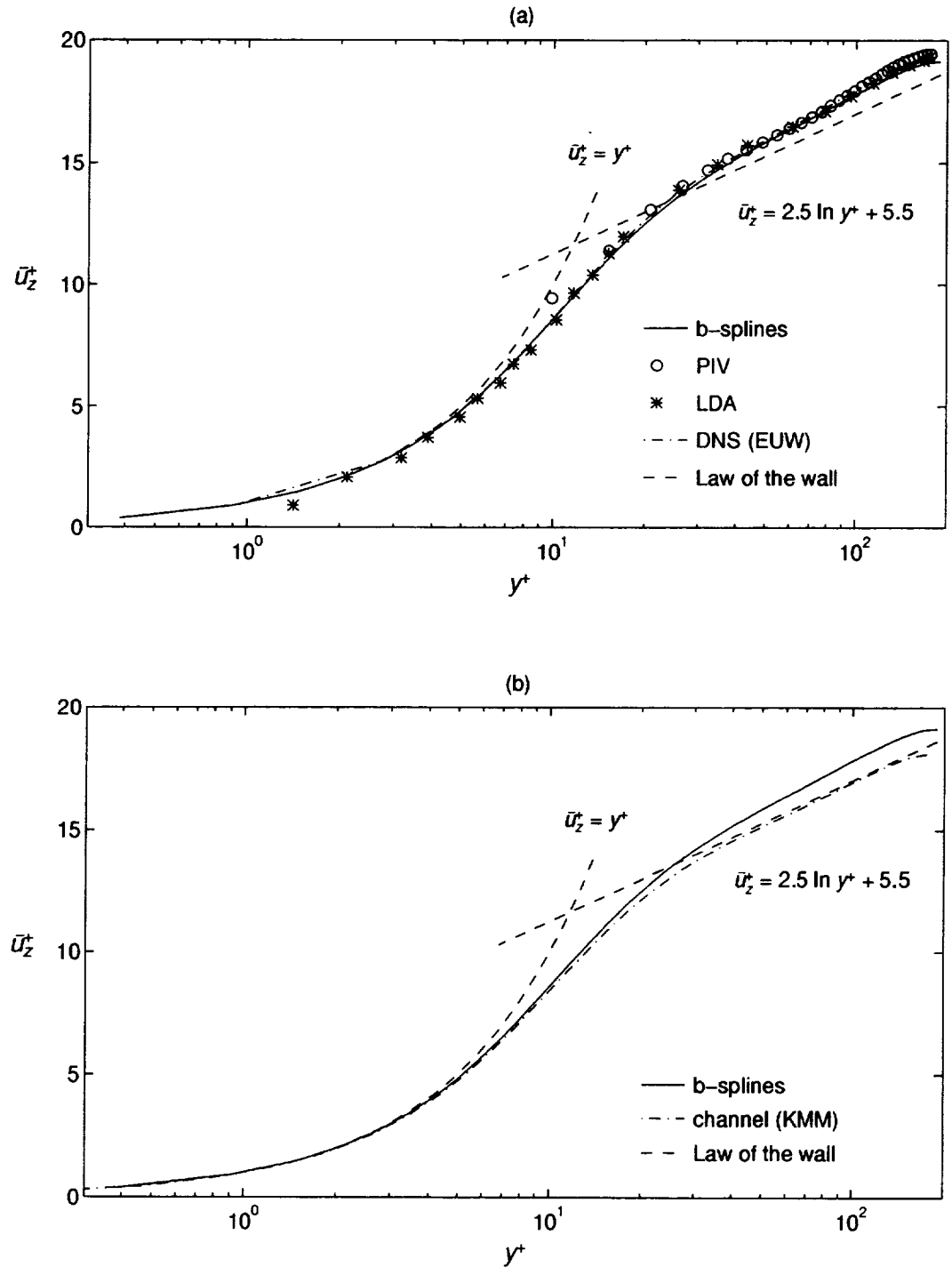

Figure 3.2: Mean velocity profiles scaled with u_τ: (a) pipe, (b) comparison between the pipe and channel.

and the two simulations. In the viscous sublayer ($y^+ < 5$) the present simulation and the law of the wall collapse to a single curve until $y^+ \approx 4$. This collapse is even more apparent in figure 3.2 (b) where the pipe is compared to the channel; all three curves are undistinguishable in the viscous sublayer. In the inertial sublayer (log region), the expected discrepancy between pipe flow and the log law is apparent. Patel and Head [32] observed this discrepancy for pipe flow up to $Re_b \approx 10000$ [‡]. A closer look at figure 3.2 (a) shows that in the inertial sublayer, the present simulation is closer to the logarithmic profile than that of EUW, which is consistent with the trend observed by Patel and Head for higher Reynolds numbers. For channel flow however, they found that a lower value of $Re_b \approx 3000$ was sufficient to match the logarithmic profile. Figure 3.2 (b) compares the velocity profiles for the pipe and channel; following KMM, the additive constant is taken to be 5.5 to compensate for low Reynolds number effect, instead of the more common 5.0 (see Tennekes and Lumley [47] chap. 5). As expected by Patel and Head's [32] prediction, the channel matches the logarithmic region.

Recently, Barenblatt [2] and Barenblatt and Prostokishin [3] introduced a power law to describe the velocity profile in the inertial sublayer instead of the traditional logarithmic profile. The novelty in Barenblatt's approach is the dependency of the predicted profile on the Reynolds number. Whereas the log law is independent of the Reynolds number (based on Kármán's constant $\kappa = 0.40$ and an additive constant of 5.0), Barenblatt proposed the following

$$\bar{u}_z^+ = \left(\frac{1}{\sqrt{3}} \ln Re + \frac{5}{2} \right) y^{+3/(2 \ln Re)} \tag{3.2}$$

where the Reynolds number can either be based on the bulk or centerline velocity (this was found to make little difference even in the low Reynolds number range). Figure 3.3 compares the velocity profiles for the log law and Barenblatt's power law (we should point out that Barenblatt makes no claim as to the validity of his approach

[‡] Although the recent experiments on pipe flow by Durst, Jovanović and Sender [11] at $Re_b = 7442$ revealed perfect match with the logarithmic profile, raising doubts as to what the exact threshold should be.

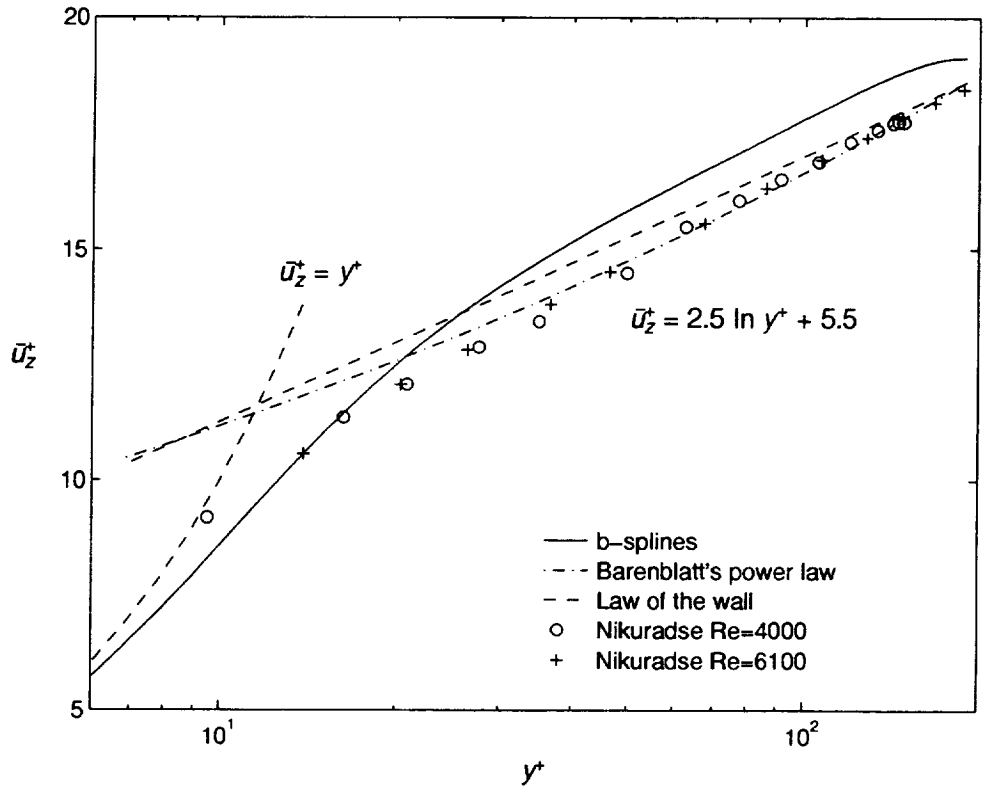

Figure 3.3: Comparison of velocity profiles in the inertial sublayer with the standard log law and Barenblatt's power law.

in the low Reynolds number range). The power law underpredicts the velocity in most of the range of y^+. Because Barenblatt's power law is Reynolds number dependent, it was possible to suggest a skin friction law given by

$$C_{f_{\text{bar}}} = \frac{2}{\psi^{2/(1+\alpha)}} \tag{3.3}$$

where

$$\psi = \frac{e^{3/2}(\sqrt{3}+5\alpha)}{2^{\alpha}\alpha(1+\alpha)(2+\alpha)} \qquad \text{and} \qquad \alpha = \frac{3}{2\ln Re} \tag{3.4}$$

Results are given in table 3.1. It is clear that the agreement is far from optimal, with errors in the 2 to 3% range, although the error seems to diminish as the

Reynolds number increases. This would be consistent with Barenblatt and Prostokishin's [3] observations that for higher Reynolds numbers, the predicted values are within experimental scatter (although they only used Nikuradse's rather dubious pipe flow measurements; from figure 3.3 Nikuradse's measurements recover the logarithmic profile even though for this Reynolds number range, the actual profile should lie above the log region). In summary, Barenblatt's power law approach does not produce better results than the standard logarithmic profile in the low Reynolds number range, although the method yields close estimates of friction coefficients.

3.2.2 Spectra and two-point correlations

Assessing the resolution of the computational domain can be made through close examination of the one-dimensional velocity and vorticity spectra. Figures 3.4–3.5 and 3.6–3.7 respectively show the velocity and vorticity spectra for several radial locations: one in the viscous sublayer ($y^+ = 3.458$), one in the buffer layer ($y^+ = 21.99$), one in the inertial, or log region ($y^+ = 122$) and one the wake region ($y^+ = 169.1$). The one-dimensional velocity spectra are defined as

$$E_{\zeta\zeta}(r;k_z) = \frac{1}{2\pi}\int_0^{2\pi} Q_{\zeta\zeta}(r,\delta\theta)e^{ik_\theta\theta'}d\theta' \tag{3.5}$$

$$E_{\zeta\zeta}(r;k_\theta) = \frac{1}{L_z}\int_0^{L_z} Q_{\zeta\zeta}(r,\delta z)e^{ik_z z'}dz' \tag{3.6}$$

where

$$Q_{\zeta\zeta}(r,\delta\theta) = \overline{\hat{u}'_\zeta(r,\theta,z,t)\hat{u}'_\zeta(r,\theta+\theta',z,t)} \tag{3.7}$$

$$Q_{\zeta\zeta}(r,\delta z) = \overline{\hat{u}'_\zeta(r,\theta,z,t)\hat{u}'_\zeta(r,\theta,z+z',t)} \tag{3.8}$$

are the two-point correlations for streamwise and azimuthal separations (no sum on repeated Greek indices). The velocity spectra is simply the Fourier transform of the two-point correlations and vice versa. Vorticity spectra ($\Omega_{\zeta\zeta}$) are similar to 3.5 and 3.6, with $\hat{\omega}'_\zeta$ replacing $\hat{u}'_\zeta$.

Velocity spectra reveal that all small scales are adequately resolved since no significant accumulation of energy is observed at high wave numbers. Away from the

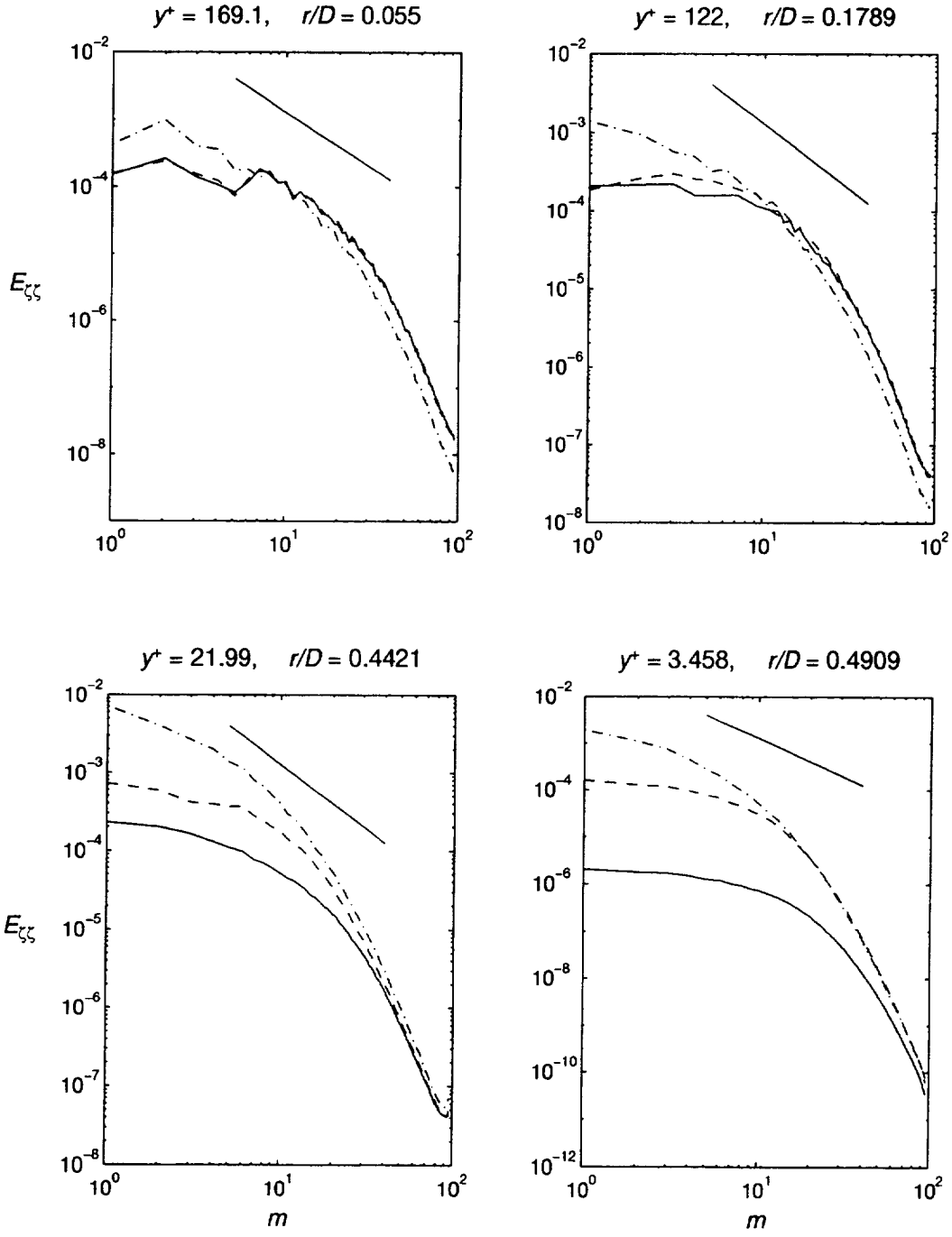

Figure 3.4: Streamwise velocity spectra: E_{rr} ——, $E_{\theta\theta}$ - - - -, E_{zz} — · — · —. The straight line indicates the Kolmogorov spectrum $E \sim {k_z}^{-5/3}$ and $m = k_z L_z/(2\pi)$.

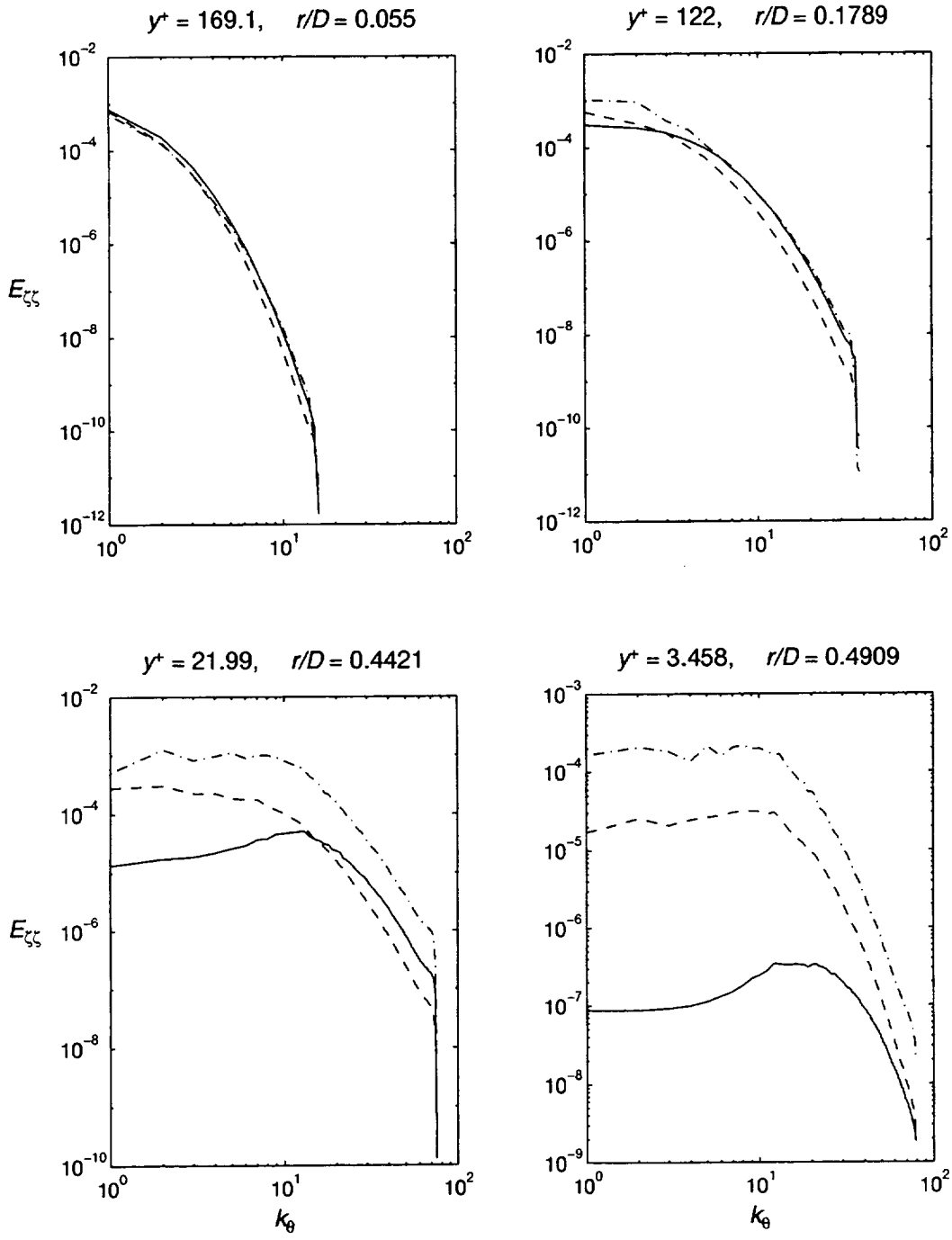

Figure 3.5: Azimuthal velocity spectra; symbols are as for figure 3.4.

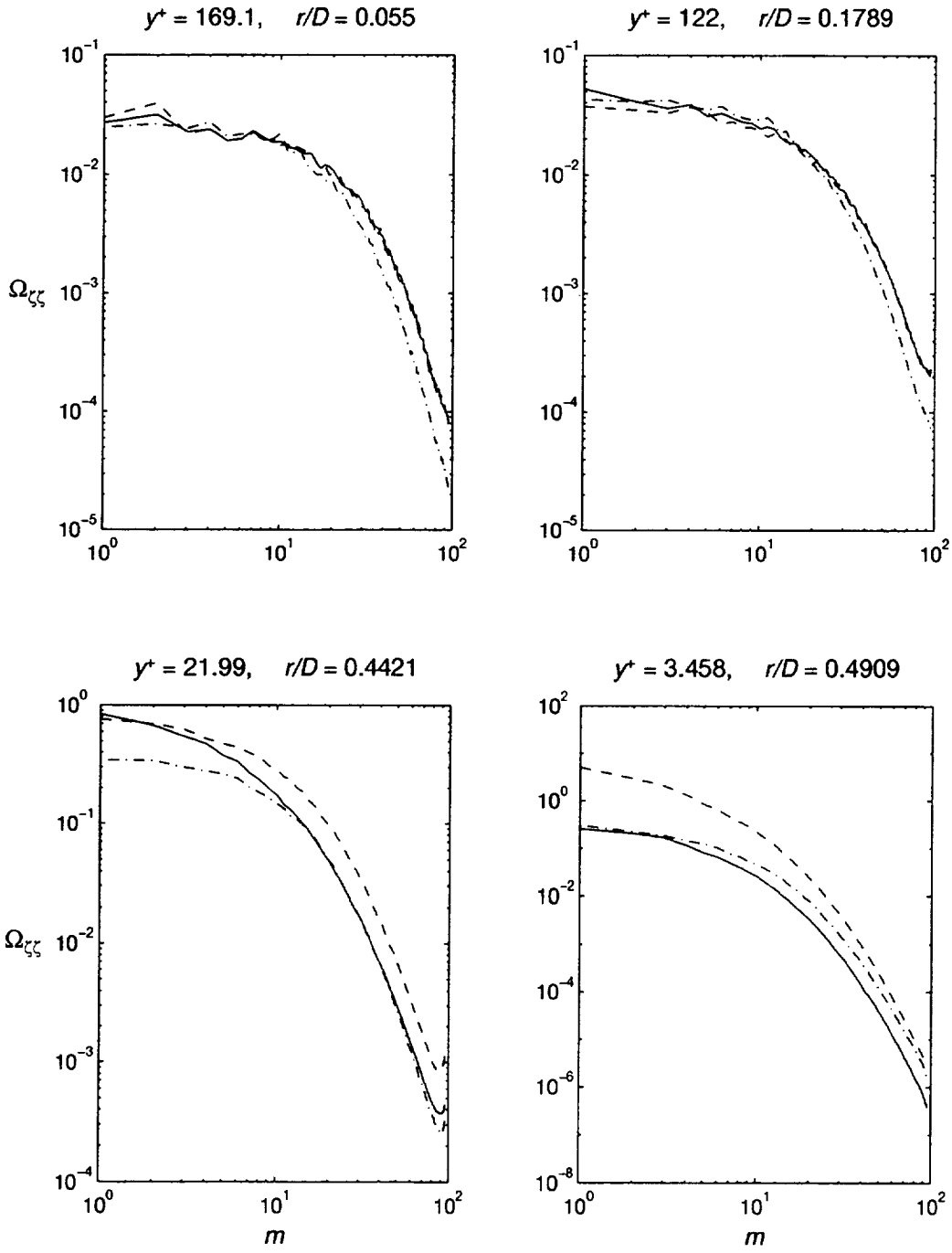

Figure 3.6: Streamwise vorticity spectra: Ω_{rr} ——, $\Omega_{\theta\theta}$ - - - -, Ω_{zz} - · - · -; $m = k_z L_z/(2\pi)$.

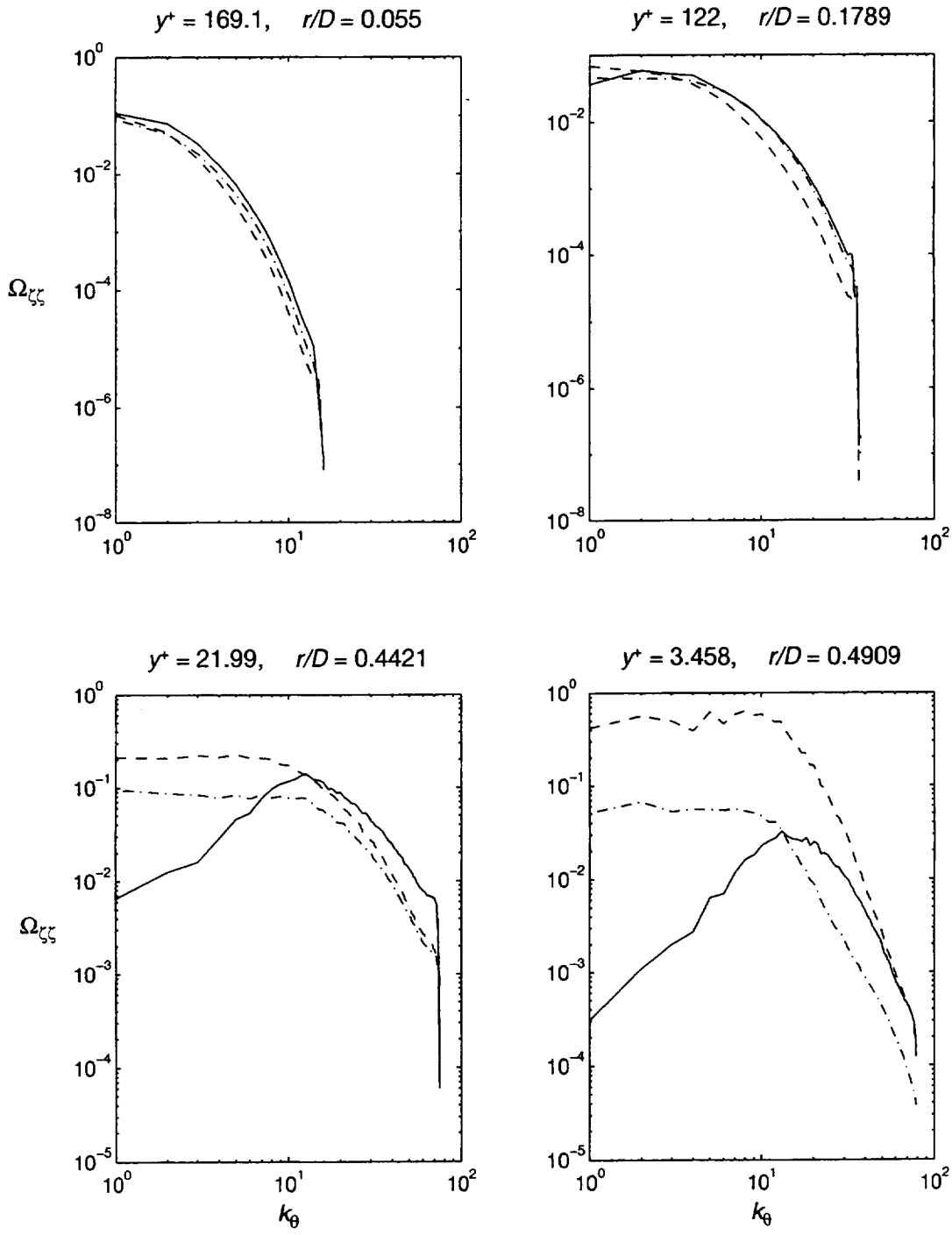

Figure 3.7: Azimuthal vorticity spectra; symbols are as for figure 3.6.

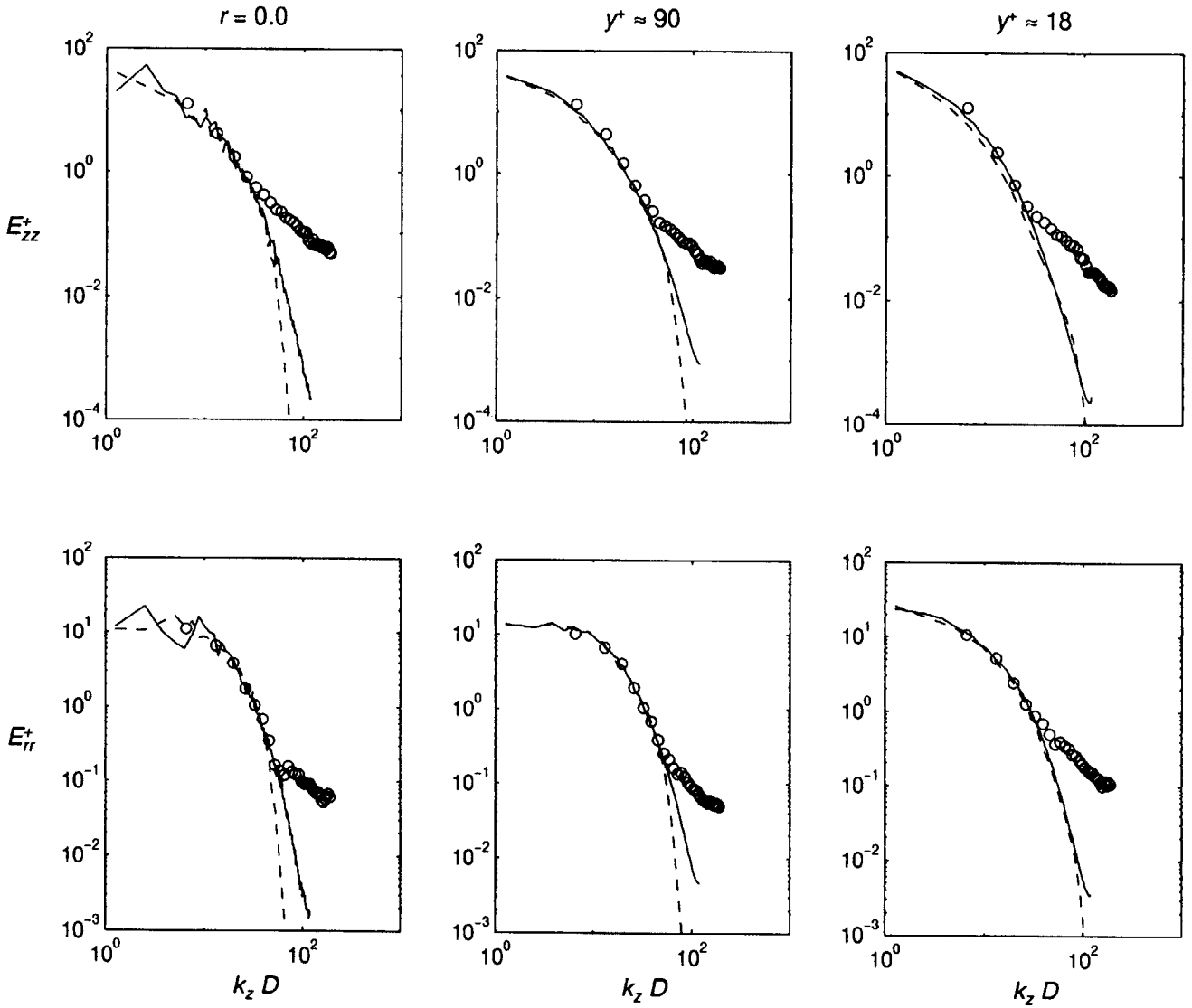

Figure 3.8: Comparison of normalized velocity spectra with PIV results and DNS (EUW). B-splines ——, PIV o, EUW - - - -.

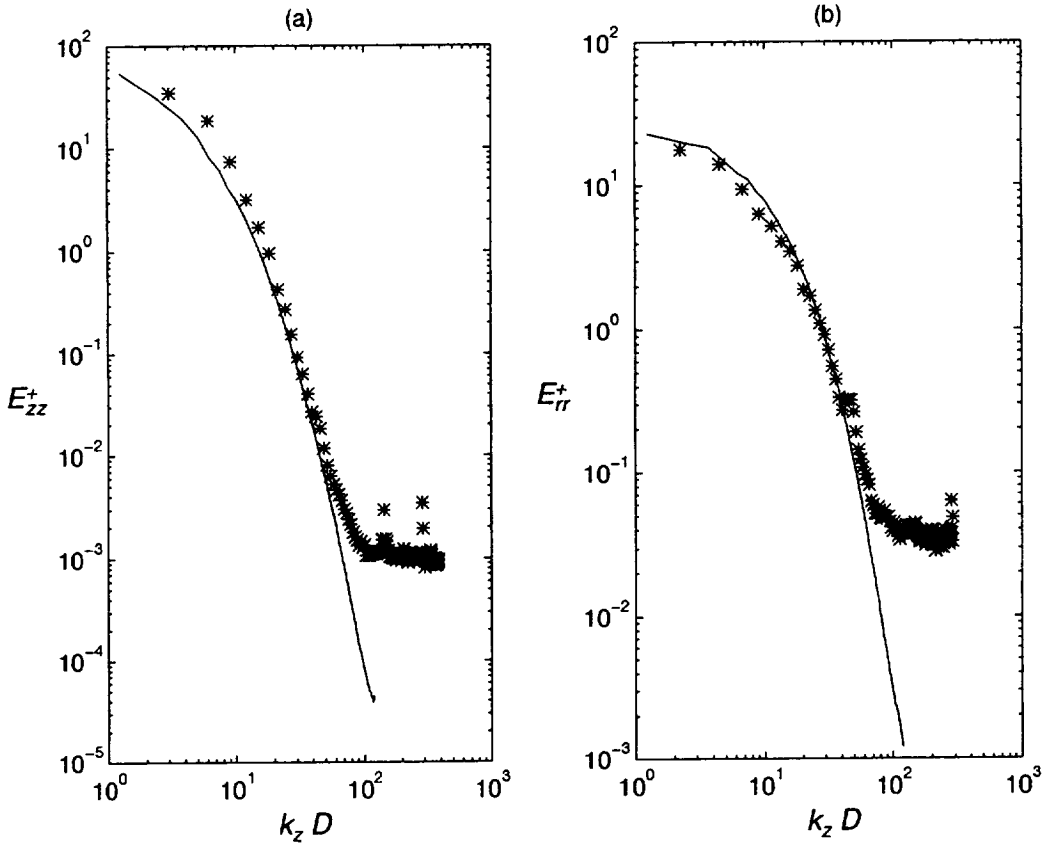

Figure 3.9: Comparison of normalized velocity spectra with LDA results for $y^+ \approx 11$. B-splines ——, LDA $*$.

wall, smaller scales show at least four decades of reduction of energy compared to the larger scales (low wave numbers). Near the wall, significant anisotropy is detected with energy of the radial perturbations being almost three orders of magnitude less than the streamwise perturbations at lower wave numbers; this is especially apparent in the azimuthal spectra. Conversely, the wall has a sustaining effect on the streamwise perturbations by maintaining a higher energy level at low wave numbers. Large radial perturbations are virtually non-existent near the wall. Figure 3.4 shows energy spectra compared to the inertial range of the Kolmogorov spectrum, or $k^{-5/3}$ law. Away from the wall (typically in the log region), The energy follows the Kolmogorov

spectrum rather closely at moderate wave numbers, indicating mostly turbulent diffusion; closer to the wall viscosity becomes predominant and the energy decays faster. The higher level of noise in the spectra near the center are caused by the small number of azimuthal modes, which degrades spatial averaging.

Further evidence of the adequate resolution is seen in the vorticity spectra, since vorticity is more sensitive to the resolution of the small scales. Vorticity spectra show at least three decades of decay and no significant pile-up of energy at high wavenumbers. A very small amount of pile-up is observed in the streamwise spectra for $y^+ \approx 22$, but overall should have no consequence because of the large drop in energy between low and high wave numbers. Near the wall, the higher energy level of the azimuthal perturbations is a direct consequence of the streamwise velocity perturbations also being large (see figure 3.16 and 3.18). The rather abrupt cut-off observed at high wave numbers near the center is a consequence of modal reduction.

Figures 3.8 and 3.9 compare the present spectra with those from the experiments of WDV and the DNS of EUW. The spectra were normalized as follows

$$E^+_{\zeta\zeta}(k_z D) = \frac{E_{\zeta\zeta}(k_z D)}{u_\tau^2 \kappa \left(E_{\zeta\zeta}(0)/2 + \sum_{n=1}^{N_z/2-1} E_{\zeta\zeta}(n\kappa) \right)} \tag{3.9}$$

where $\kappa = 2\pi D/L_z$. Figure 3.8 shows almost perfect agreement between the experiments and the present results for $k_z D$ up to ≈ 40, after which the PIV results are unreliable. Agreement between the two simulations is also good, but two important differences appear: first, as expected, the higher wave numbers of the DNS of EUW diffuse much more rapidly than the present results; this is consistent with the higher diffusivity of their numerical scheme. Second, the near wall streamwise spectra of EUW undershoots the one obtained by the b-splines over most of the spectrum (see figure 3.8 for $y^+ = 18$); this is probably due to the lack of near wall resolution combined with the higher diffusivity of their method. This shows that most of the smaller scales are not adequately resolved by EUW.

Figure 3.9 is similar to figure 3.8, but shows the higher resolution of LDA technique. The differences between the present simulation and the LDS measurements are difficult to explain, in light of the almost perfect agreement of the PIV results. A

possible explanation is the proximity of the wall ($y^+ \approx 11$) which makes the measurements more difficult; an anomaly of the experimental data is clearly visible in figure (b) at $k_z D \approx 45$.

Figures 3.10 and 3.12 give the two-point velocity correlations for streamwise and azimuthal separations respectively; figures 3.11 and 3.13 give the equivalent two-point vorticity correlations. Figure 3.10 for $y^+ \approx 3.5$, shows the velocity perturbations are still slightly correlated for large streamwise separations which implies that the size of computational domain (L_z) might be marginal (too short), although not by much since the values are quite small. For other radial positions, the zero correlation point is still within statistical sampling error as indicated by the standard deviation; near the center, the error becomes very large due to the fewer number of azimuthal modes. EUW's results also show symptoms of a marginal domain length. However, their results show that the correlation is maintained further away from the wall than in the present computations; this is again due to their larger viscosity and numerical damping.

The streamwise component of the streamwise velocity correlations are correlated over longer distances, indicating the presence of coherent streamwise features, or so-called streaks. The two-point vorticity correlation (fig. 3.11) also indicates that in the near wall region, the values are correlated over the length of the domain. Note however that near the center, the vorticity correlation gives a much clearer picture than the velocity correlation did: there is no evidence of correlated values near the center, and even down to $y^+ \approx 22$. In the viscous sublayer, the presence of long vortex-sheets are apparent by the longer correlation length of the azimuthal component.

The extent of the two-point velocity correlations for azimuthal separations show the circumferential size, or width of the streaks. The results show that the width of the streaks is rather narrow as indicated by the zero-crossings of the streamwise component at $y^+ \approx 3.5$; we obtain $\lambda^+ \approx 55$, where λ^+ is the average width of a streak, for an average streak spacing of $2\lambda^+ \approx 110$; this is in agreement with Kline *et al.* [18] who experimentally found a mean streak spacing of $2\lambda^+ \approx 100$ in boundary layers, Moser and Moin [25] who also obtained $2\lambda^+ \approx 100$ in curved channel flow, and similarly for KMM and the straight channel. The large negative correlation in the

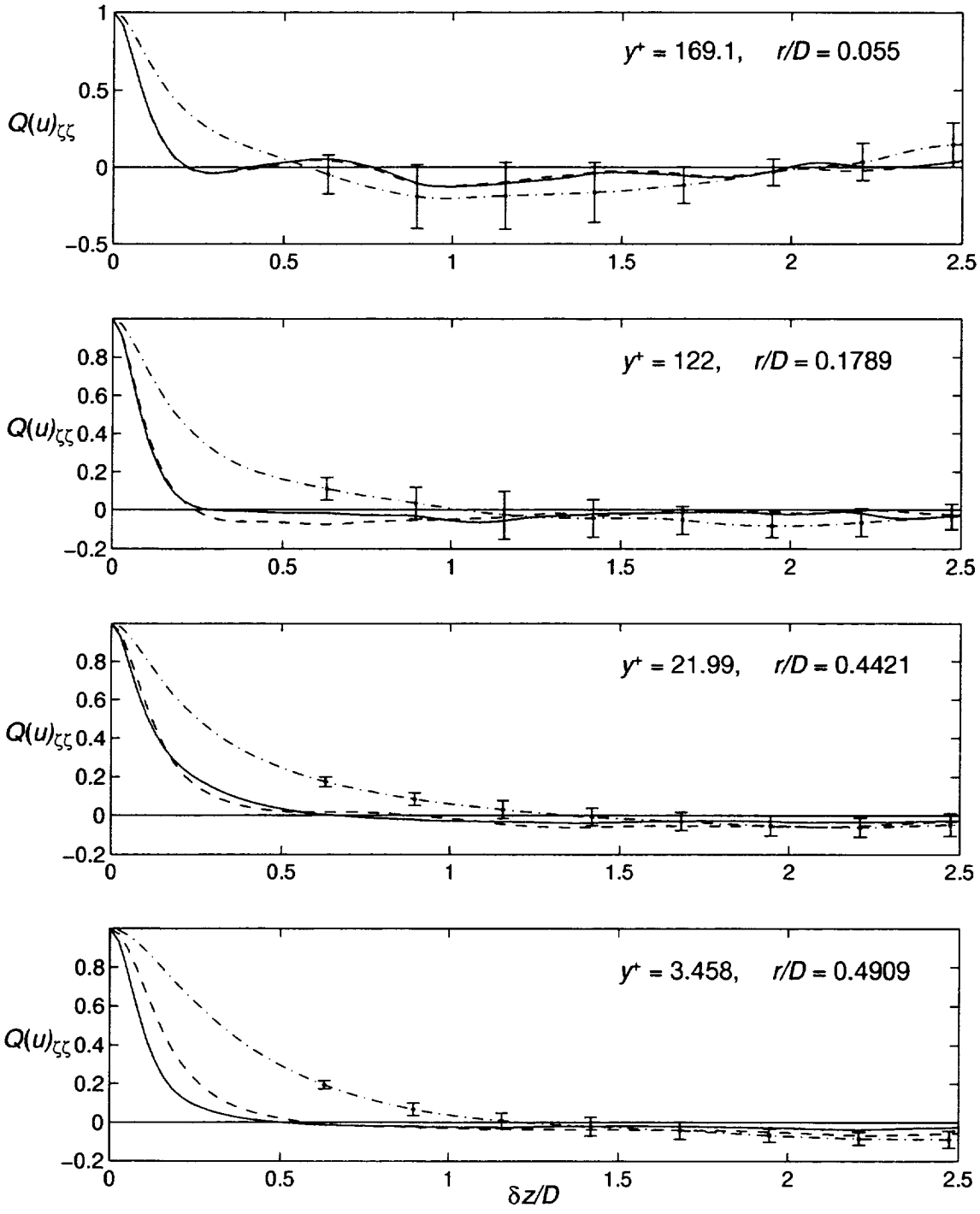

Figure 3.10: Two-point velocity correlations for streamwise separation: Q_{rr} ——, $Q_{\theta\theta}$ - - - -, Q_{zz} - · - · -. The error bars indicate the standard deviation ($\pm\sigma$) of the streamwise component.

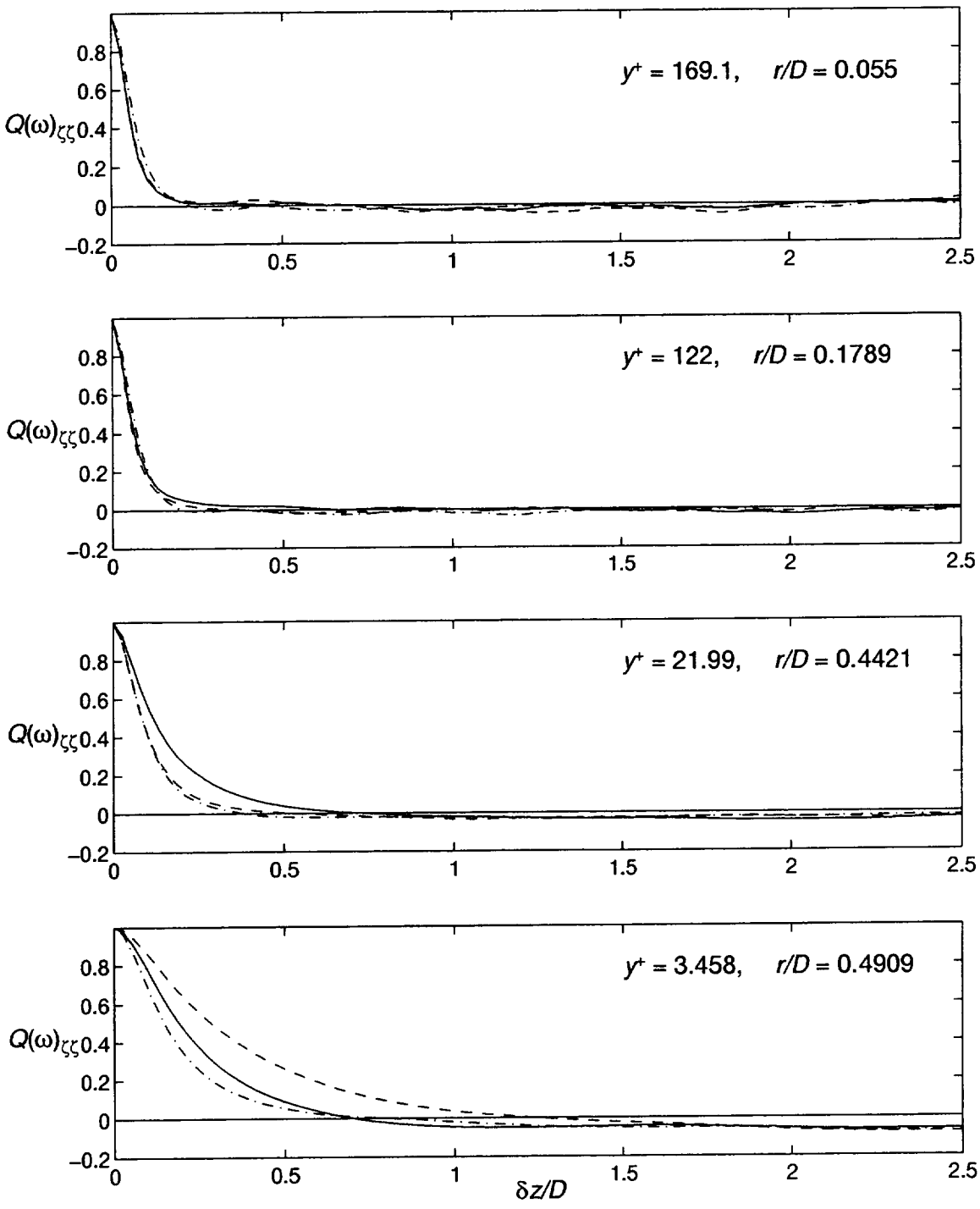

Figure 3.11: Two-point vorticity correlations for streamwise separation. Symbols as for figure 3.10.

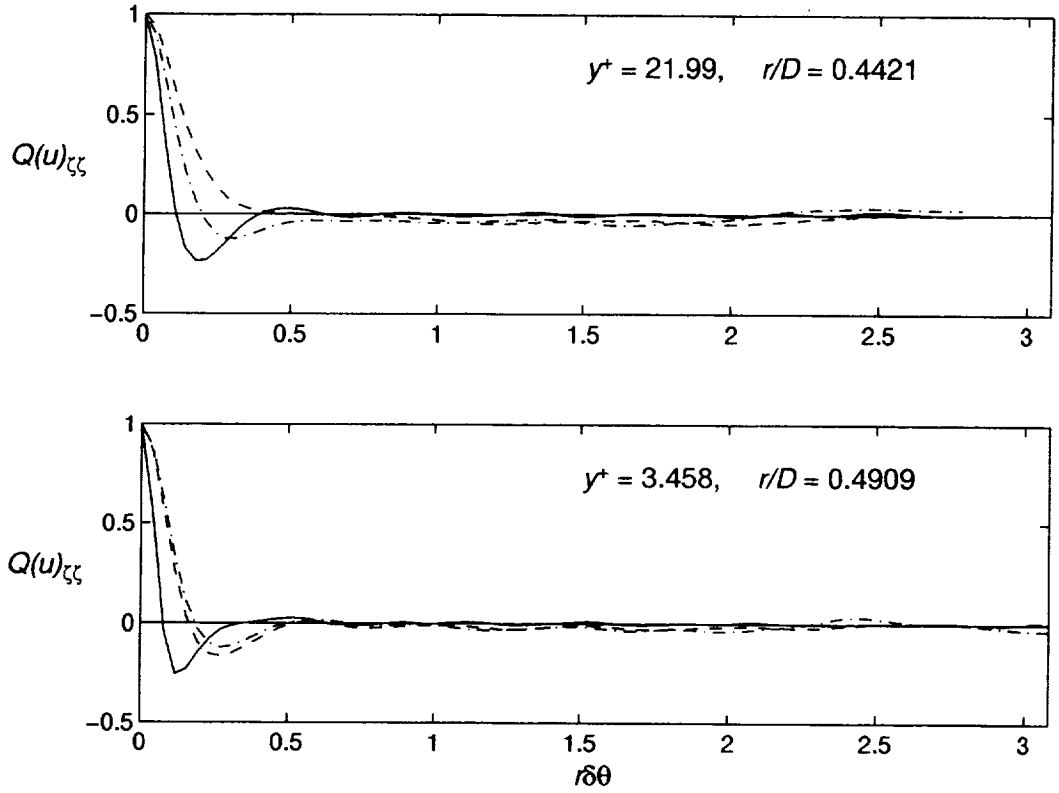

Figure 3.12: Two-point velocity correlations for azimuthal separation; symbols are as for figure 3.10.

radial component is produced by the impingement and ejection of fluid toward and away from the wall; this was also observed in KMM and Moser and Moin [25]. Two-point vorticity correlation for azimuthal separations are also shown on figure 3.13. A large negative correlation is observed which indicates the presence of counter-rotating radial vortices. Figure 3.14 shows contour plots of the streamwise and radial vorticity and velocity perturbations for a single flow realization; it illustrates physically the two-point correlations: the presence of a (short) streamwise vortex (3.14.a) entrains fluid, with one side going toward the wall (impingement, $u_r' > 0$) and one side going away from the wall (ejection, $u_r' < 0$) (3.14.b). The impinging fluid has a positive radial vorticity and the ejecting fluid, negative radial vorticity (3.14.c); the motion of the impiging and ejecting fluid is not strictly linear but *helical*. These two counter-rotating radial vortices entrain fluid in the streamwise direction in the region between

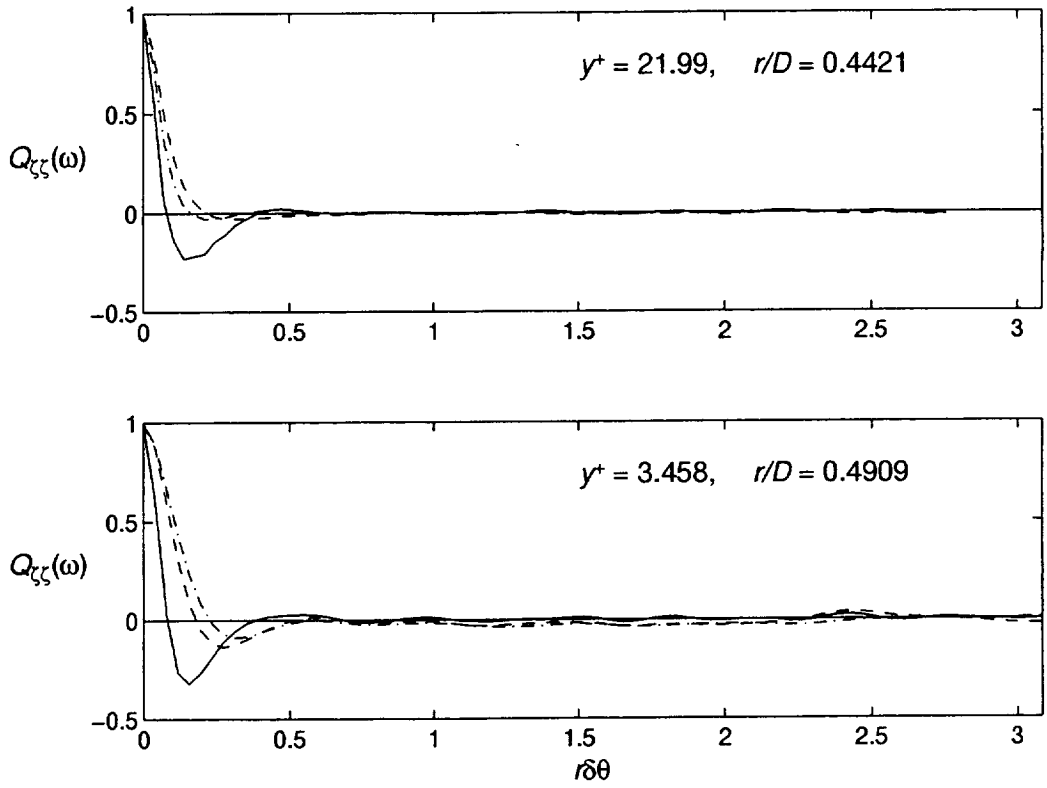

Figure 3.13: Two-point vorticity correlations for azimuthal separation; symbols are as for figure 3.10.

their respective cores (3.14.d), yielding a high speed streak. The positive streamwise velocity perturbation is seen to extend behind the location of the streamwise eddy indicating that the eddy is moving downstream in the pipe leaving behind it a high speed streak.

3.2.3 Turbulent intensities

Figures 3.15 (a) shows the Reynolds shear stress for the present simulation, the experiments of WDV and computations of EUW. The measurements, especially PIV, show significant deviation from the computations; PIV is better suited to collect instantaneous fields than to gather statistics (see EUW). LDA results track the computed value more closely, but lack resolution for $r > 0.7$. Both computations show close

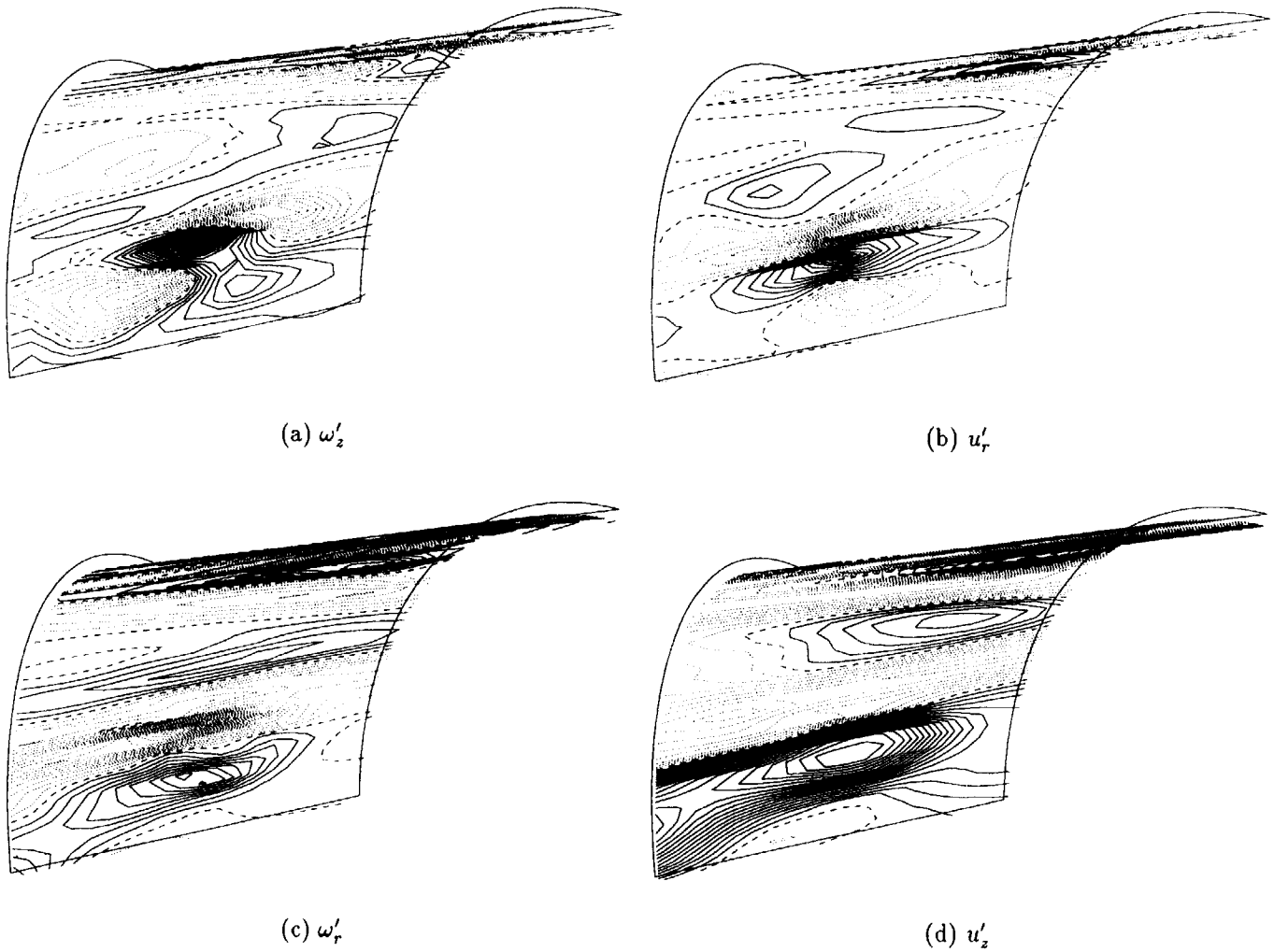

(a) ω_z' (b) u_r'

(c) ω_r' (d) u_z'

Figure 3.14: Contour plots of the streamwise and radial velocity and vorticity perturbations ($y^+ \approx 5$). Length of segment $\approx L_z/10$. Solid, dashed and dotted lines are respectively positive, zero and negative contours.

agreement, except for $r > 0.8$ where the differences are consistent with differences in Reynolds number. The total shear stress (see page 33), is almost linear indicating statistical steady state or fully developed turbulence. The exact value of $\tau_{rz}^{+} = r$ is is plotted for reference. The present results agree well except for a slight overshoot for $0.5 < r < 0.65$, whereas EUW has a slight overshoot for $r < 0.65$. Figure 3.15 (b) reveals almost perfect agreement between the pipe and channel. The slight overshoot of the b-splines between $0.2 < r < 0.6$ is probably caused by the number of samples used to generate the average.

Figures 3.16 and 3.17 show the rms (root mean square) of the three velocity perturbations. Figure 3.16 (a) reveals relatively good agreement with the experiments and both simulations. For the radial and azimuthal components, the differences between both computations are consistent with different Reynolds numbers, with the present simulation being somewhat higher. The difference for the streamwise component is rather surprising, with EUW simulation overshooting the present computation in the region $0.6 < r < 0.9$, a trend opposite to what is observed for the other two components. The higher energy of the streamwise component is probably due to numerical artifacts produced by EUW method, such as inadequate resolution in the near-wall region. This is confirmed by figure 3.16 (b) where the same rms velocity fluctuations are compared with KMM's channel simulation. Slight differences between all three components are observed, with the pipe results being consistently above the channel's; values are closely matched near the wall, and somewhat higher intensity for the pipe near the center, a trend similar to the mean flow.

DJS conducted a series of LDA measurements in the near-wall region of pipe flow at different Reynolds number ranging from 7442 to 20 500. The results for $Re_b = 7442$ are plotted in figure 3.17; the agreement between their measurements and the present computations is excellent, especially for the streamwise and azimuthal components. The added noise in the azimuthal component is not surprising since this is the most delicate direction to measure (WDV did not even attempt to make measurements in the azimuthal direction). In fact, most of the data showing the greatest deviation was measured from the centerline to the upper wall, whereas the data measured from the centerline to the lower wall agrees much more closely. Measurements for the radial

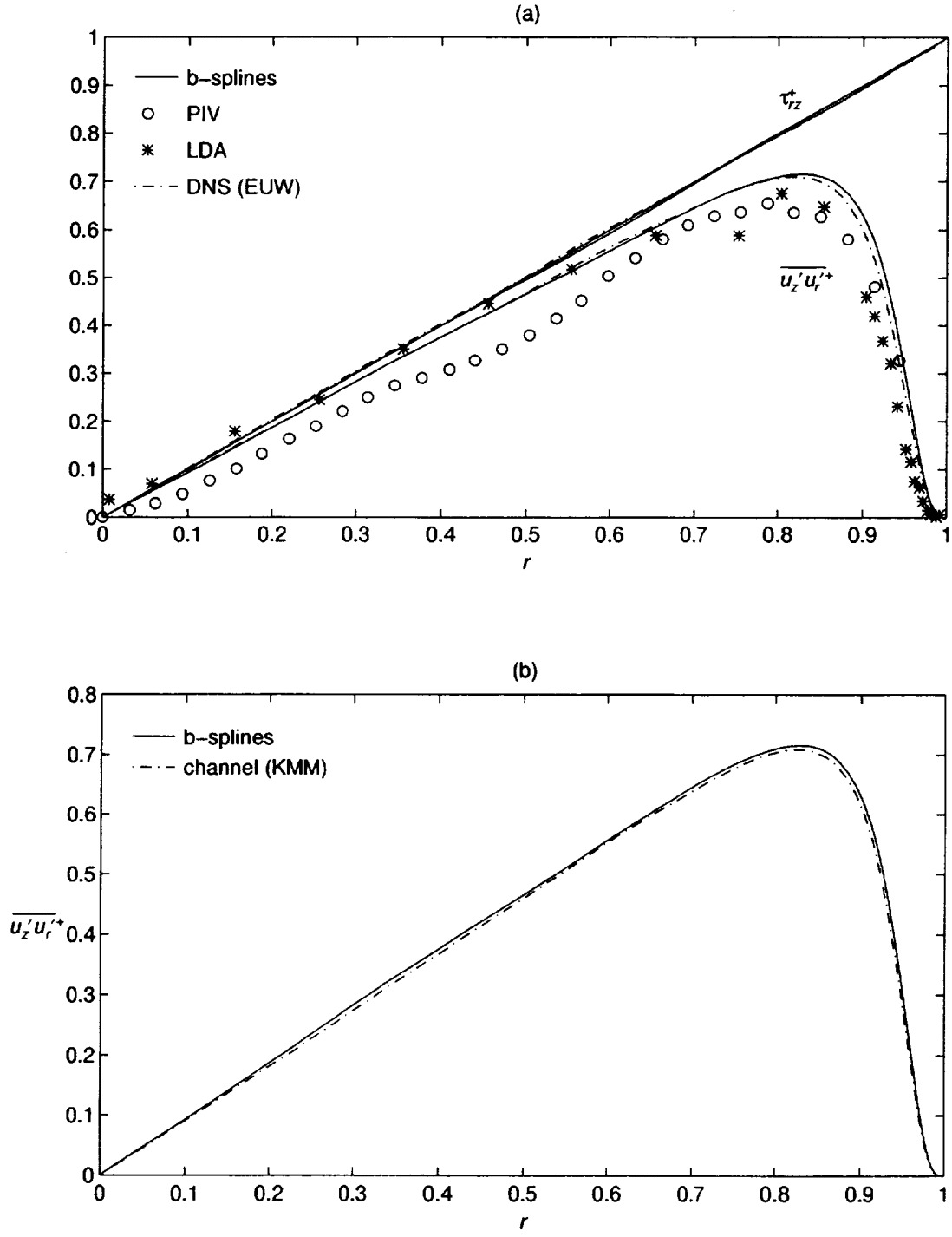

Figure 3.15: Reynolds shear stress: (a) pipe data with total shear stress ($\tau_{rz}^+ = r$); the exact value of τ_{rz}^+ is also plotted for comparison. (b) comparison between the pipe and channel.

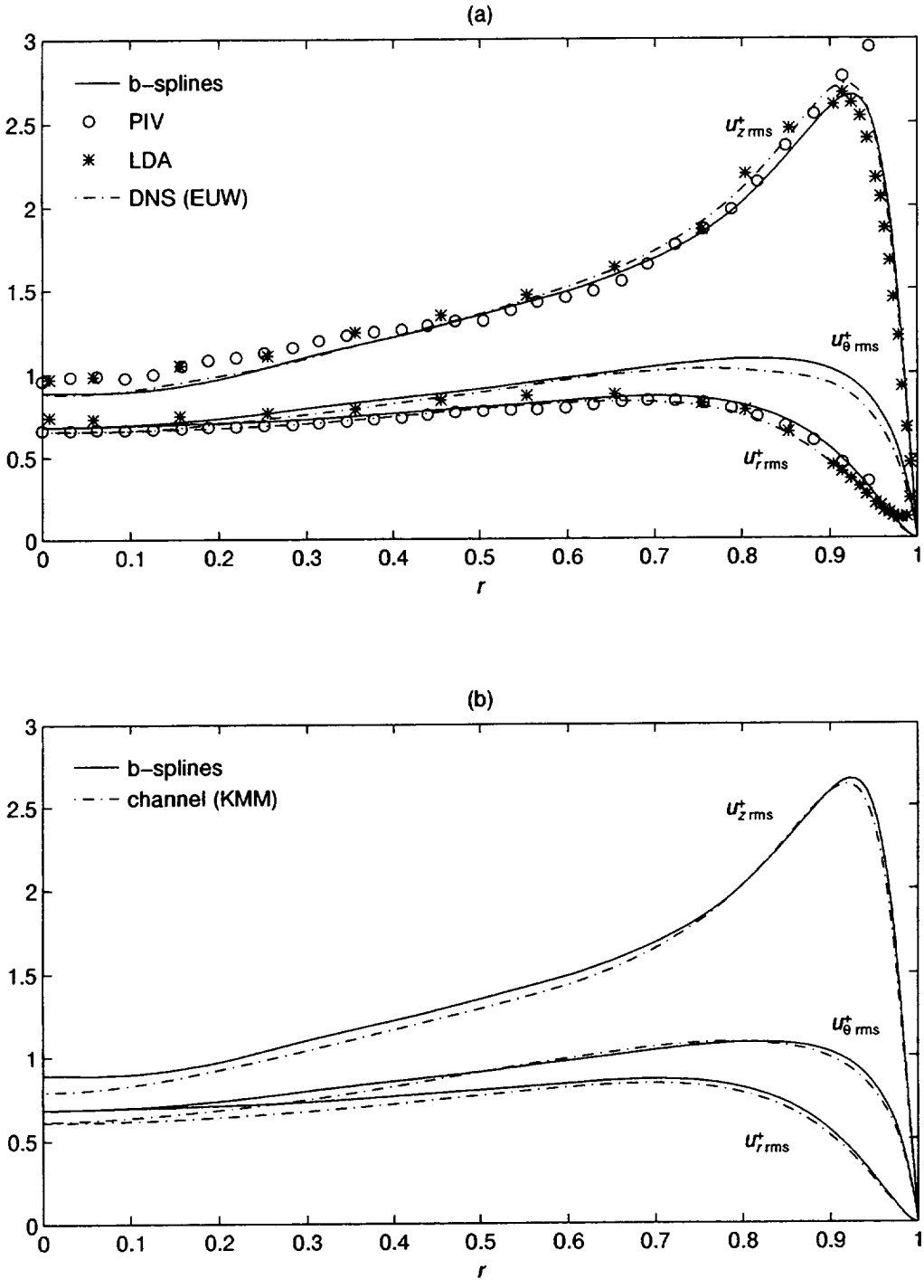

Figure 3.16: RMS (root mean square) of velocity fluctuations: (a) pipe, (b) comparison between the pipe and channel.

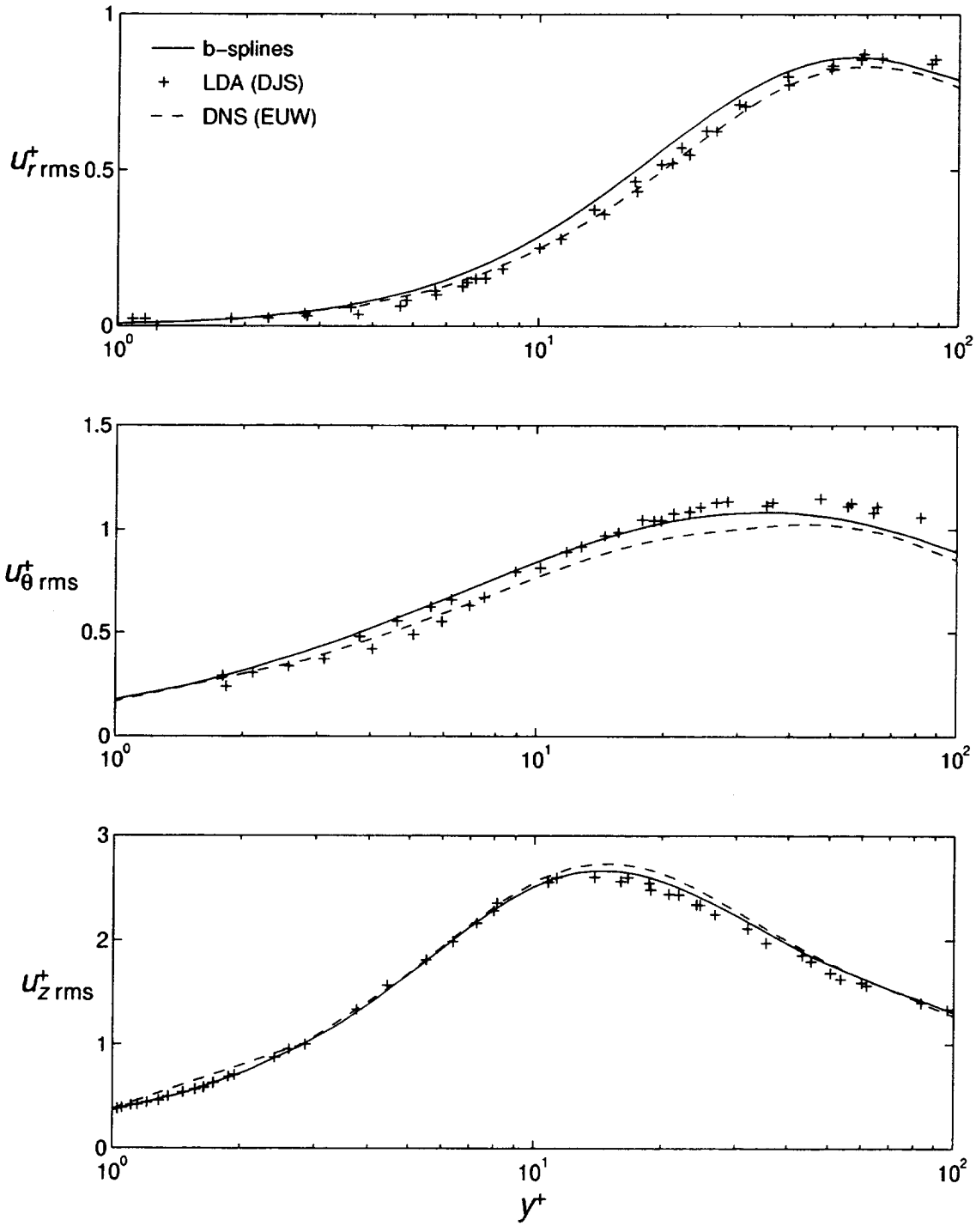

Figure 3.17: RMS of velocity fluctuations: comparison between the present simulation and DJS' near-wall LDA data ($Re_b = 7442$).

component tend to fall between the present results and EUW's simulation; a possible explanation for this lower than expected amplitude might stem from DJS' rejection of high amplitude radial perturbations (see section 3.2.4). Farther from the wall, Reynolds number effects are apparent with the measurements having higher values (figure 16 of DJS shows this trend for different Reynolds numbers).

Figure 3.18 (a) shows the rms pressure[§] fluctuations normalized by ρu_τ^2. The shape of the profile is in good agreement with the results of EUW; the higher values for the present simulation is a result of higher Reynolds number, which seems to support KMM's assumption that pressure fluctuations are dependent on Reynolds number, even when normalized by wall variables (see KMM section 4.2). The results are also in qualitative agreement with KMM, where they obtained a maximum of 1.75 at $y^+ \approx 30$ with a wall value of ≈ 1.5, versus a maximum greater than 2 at $y^+ \approx 31$ and a wall value of ≈ 1.65 for the present results. The centerline value is also higher at ≈ 0.95 for the pipe versus ≈ 0.75 for the channel. Clearly, for a similar Reynolds number the pipe possesses larger pressure fluctuations than the channel.

Figure 3.18 (b) shows the rms of vorticity fluctuations normalized by u_τ^2/ν. These results are in good qualitative agreement with KMM, Moser and Moin [25] and the pipe flow simulation of Zhang *et al.* [55], the latter being a much lower Reynolds number flow ($Re_b = 2500$). Unfortunately, no experimental measurements could be found for comparison. Comparing with KMM, the streamwise vorticity shows a local minimum at $y^+ \approx 5$, with a maximum being reached at the wall. KMM have attributed this to the presence of streamwise vortices close to the wall. Figure 3.19 shows a view in the polar plane of the streamwise vortex shown on figure 3.14. The maximum in rms vorticity at the wall is explained by the presence of a mirror vortex with vorticity inverse to that of the eddy. Between the mirror vortex and the eddy, vorticity reaches zero; in the average sense however, this translates into vorticity reaching a minimum.

For $r < 0.75$ all three vorticity fluctuations are virtually identical contrary to velocity fluctuations which are quite different. This points to isotropy of the small

[§]Because pressure drops out of the equation set (see 2.3.1), a Poisson solver had to be written to compute the pressure which can be determined solely from the velocity.

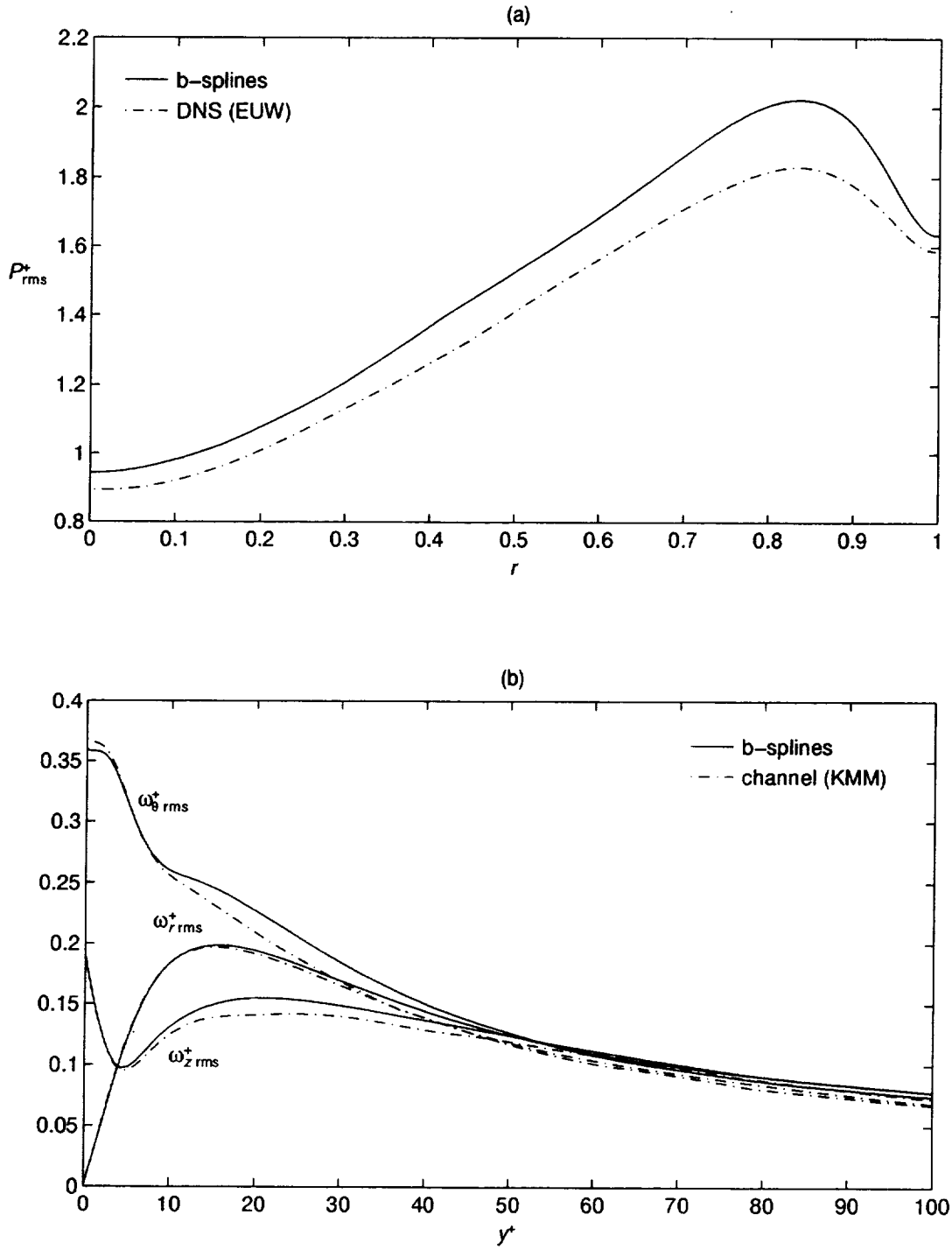

Figure 3.18: (a) RMS of pressure fluctuations normalized by ρu_τ^2. (b) RMS of vorticity fluctuations normalized by u_τ^2/ν.

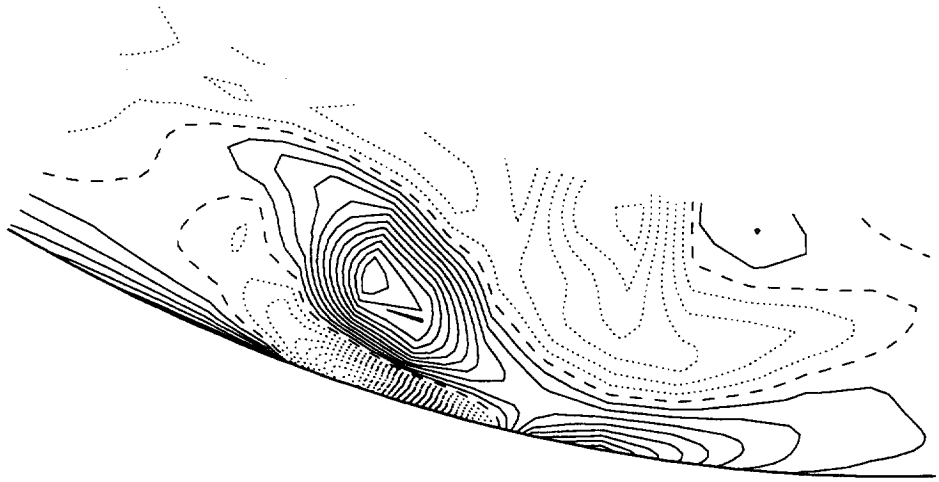

Figure 3.19: Streamwise vorticity perturbation ω_z'. Solid, dashed and dotted lines are respectively positive, zero and negative contours.

scales since vorticity fluctuations are by nature small scales phenomena whereas velocity fluctuations tend to be produced by larger, more energetic scales.

3.2.4 Higher order statistics: Skewness and Flatness

Skewness and flatness (also referred as *kurtosis*) are shown in figures 3.20–3.23. They are respectively defined as third and fourth moments of velocity perturbations

$$S(u_i') = \frac{\overline{u_i'^3}}{\overline{u_i'^2}^{3/2}}, \qquad F(u_i') = \frac{\overline{u_i'^4}}{\overline{u_i'^2}^2} \tag{3.10}$$

Each is related to the probability density: if the skewness is positive, then events with large negative values of $u_i'^3$ are not as frequent as events with large positive values of u_i'; if the flatness is large, then isolated events with large velocity perturbations are possible (see Tennekes and Lumley [47]). For a Gaussian distribution of u_i', the skewness and flatness are respectively 0 and 3.

Figure 3.20 compares the skewness obtained from the present computation, with the experiments of WDV and the DNS of EUW. Results from the present simulation

and PIV measurements show significant disagreement throughout the flow field, attributable to the low precision of the PIV method. LDA results for the streamwise component are in good agreement with both computations except near the wall where the results are obscured by noise. The measurements of DJS (figure 3.21) shows good agreement except for a slight underpredicting of the the streamwise component for $y^+ < 5$. In such a close proximity to the wall, accurate experimental measurements are hard to achieve. Note that because of the normalization by $u_i'^n$, skewness and flatness results for $y^+ = 0$ are excluded, since the numerical limit as the wall is approached is undefined, even though an analytical limit might exist.

Clearly, the most interesting difference is observed between both simulations for the radial component. The present results reveal two zero-crossings ($r \approx 0.8$ and $r \approx 0.97$), whereas EUW obtained only one zero-crossing at $r \approx 0.75$. On the other hand, the present results are in agreement with the results of KMM (not shown) who also obtained two crossings at approximately the same locations. This seems to be confirmed by the LDA results of DJS (figure 3.21) where the trend in the data points to another crossing at $y^+ \approx 3$, although not decisively. The discrepancy between the present results and EUW can only be caused by the coarser near-wall resolution of EUW's computation. Scatter in the azimuthal component is attributable to a poor statistical sample, since this component should be strictly zero by the equal probability of positive and negative u_θ'. Similar scatter can also be seen in the streamwise component closer to the center.

A similar comparison of the flatness (figures 3.22 and 3.23) reveals good agreement between the LDA measurements of WDV and DJS, the simulation of EUW and the present simulation, except in the near-wall region. Typically, for $y^+ < 5$ the experimental measurements become obscured by noise and become unreliable. Coarseness of EUW's grid probably explains the differences between both computations in the near-wall region. For example, EUW computed a flatness of 5.5 at the wall for the streamwise component, whereas the present simulation gives 4.5; this value compares favorably with KMM who obtained 4.2.

The most important discrepancy is observed between the present simulation and

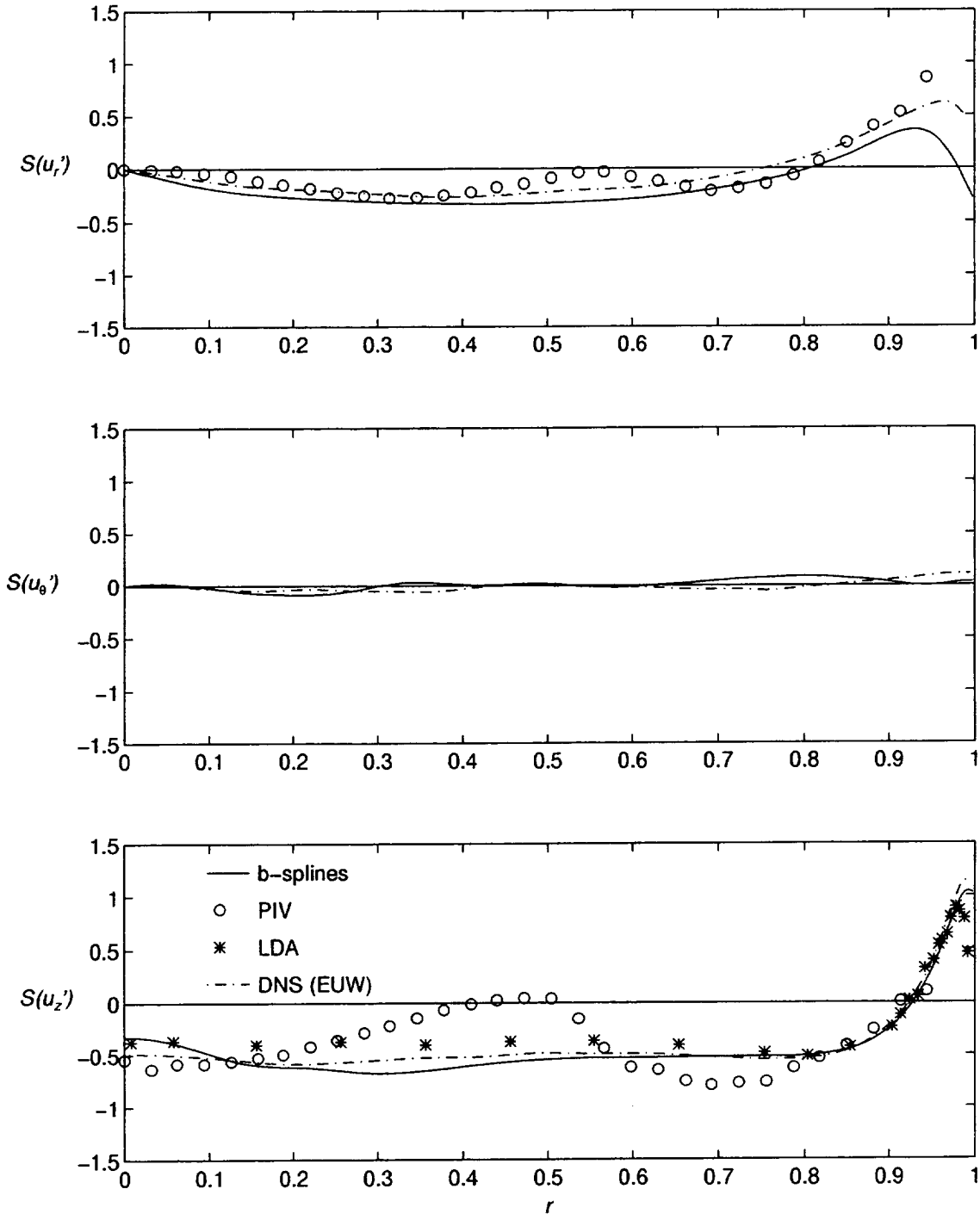

Figure 3.20: Skewness of velocity fluctuations. $S(u_i') = 0$ indicates Gaussian distribution.

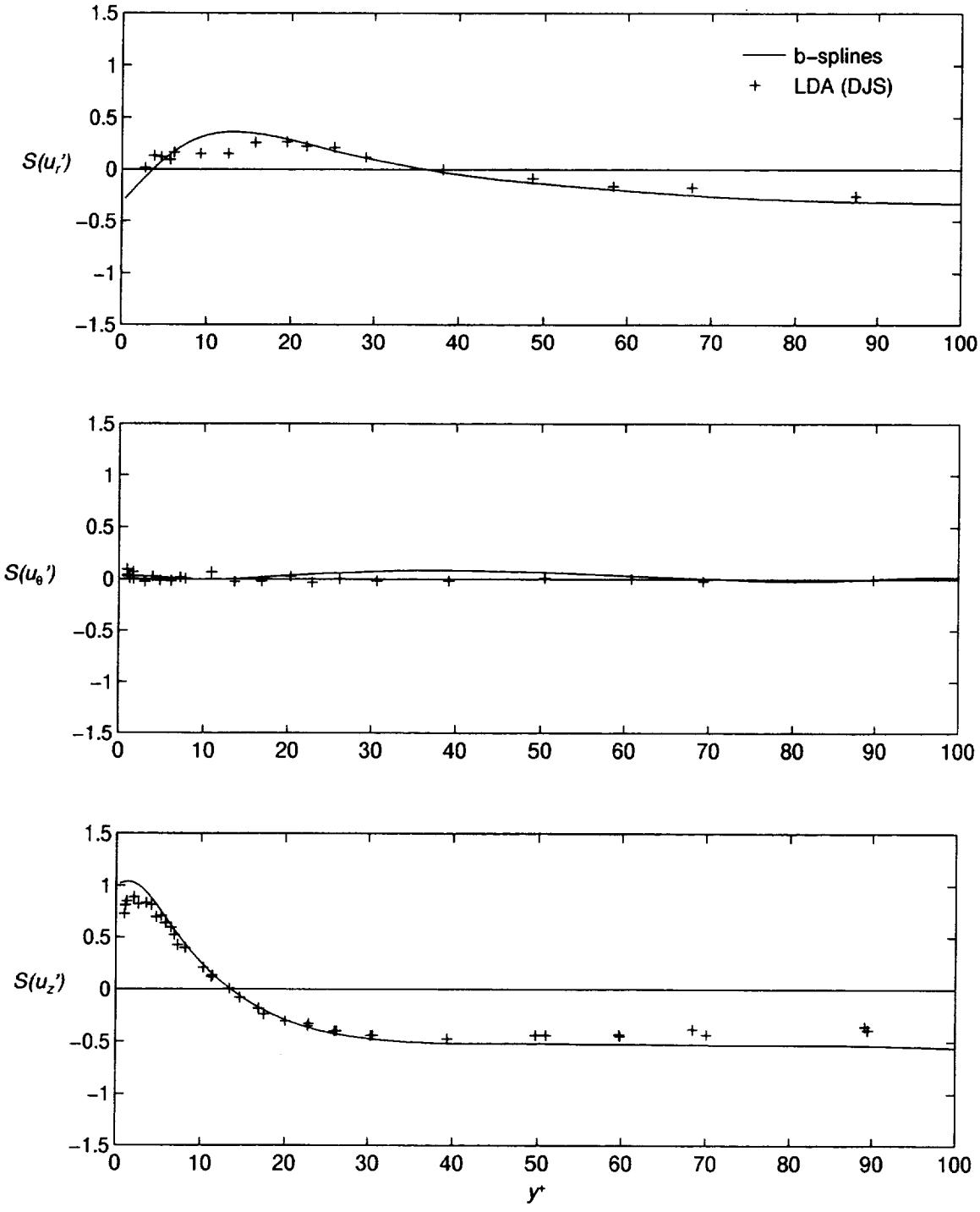

Figure 3.21: Skewness of velocity fluctuations: comparison with near-wall LDA measurements (DJS).

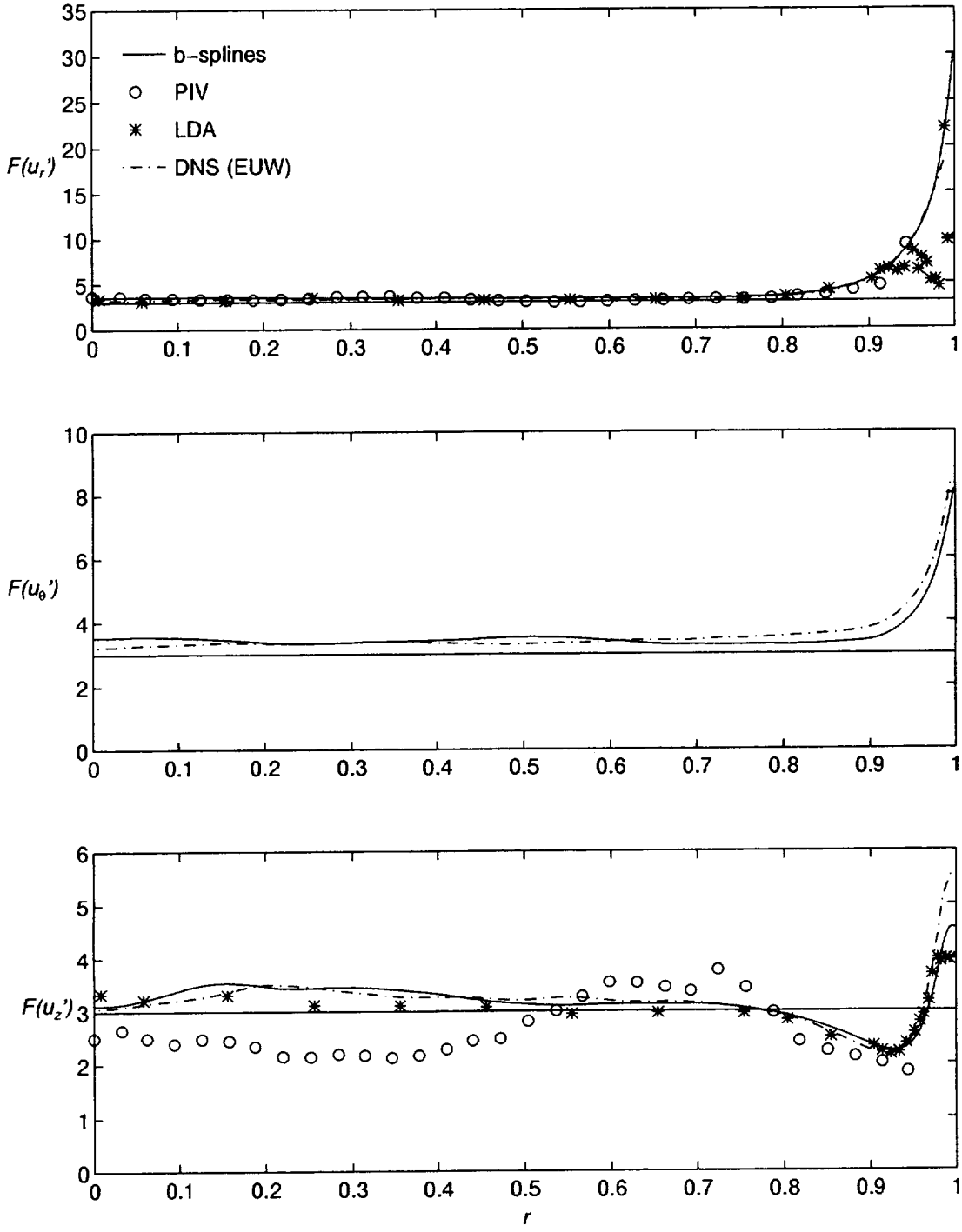

Figure 3.22: Flatness of velocity fluctuations. $F(u_i') = 3$ indicates Gaussian distribution.

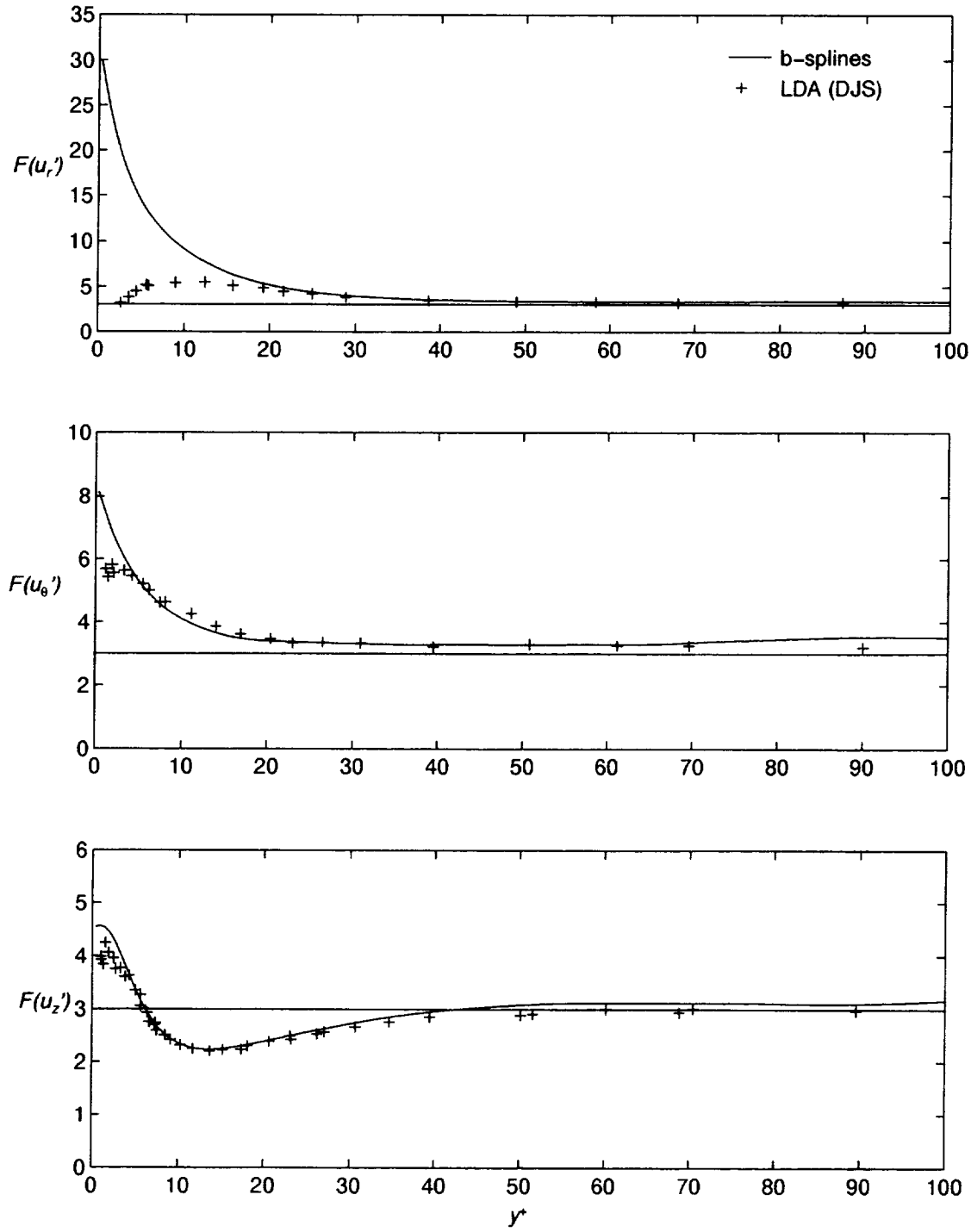

Figure 3.23: Flatness of velocity fluctuations: comparison with near-wall LDA measurements (DJS).

DJS' measurements of the radial component. Whereas the computed flatness increases monotonically reaching a maximum at the wall, DJS' measurements shows a maximum at $y^+ \approx 12$ and then decreases towards a near-Gaussian behavior at the wall. Comparing with KMM's data, which shows the same trend as the present results, DJS speculated that the discrepancy might be caused by the near-wall resolution of KMM's simulation, even referring to KMM's results as "strange". Another explanation for the difference between the simulation and the measurements was given by Westerweel (Private communication). He observed that large fluctuations could be rejected by the filtering in the LDA processor. Xu *et al.* [54] conducted experiments in pipe flow for the sole purpose of determining whether or not large flatness was physical in nature. They were able to determine that events with large radial perturbations are indeed present in the near-wall region ($y^+ < 5$) by taking measurements at very short intervals (1 kHz); they also showed that with DJS' slower sampling (100 Hz), events with large perturbations could be ignored (thus the filtering effect); in addition, DJS interpreted as error and removed any measurement with peak larger than seven times the rms velocity. Those large perturbations, or spikes, can exceed $|u_r'/u_{r\,\mathrm{rms}}| = 10$, with rather short time scales (20 viscous time units based on u_τ^2/ν), which make the observations difficult. The present simulation tends to support Xu *et al.* observations: the large radial velocity perturbation shown in figure 3.14 (b) is equivalent to a ratio $|u_r'/u_{r\,\mathrm{rms}}| = 7.71$ at $y^+ = 5$. Closer to the wall ($y^+ = 0.385$, the first grid point away from the wall) a ratio of 10.60 is obtained; this also points to the relative sensitivity to grid spacing. Recall that with a coarser grid, EUW obtained a smaller flatness (see figure 3.22).

Figure 3.24 (see also figure 8 of Xu *et al.*) shows the effect of filtering on flatness. By removing values larger than a certain factor of the corresponding rms velocity, the flatness can be reduced to match the data of DJS. By dropping all perturbations larger in magnitude than five times the rms velocity, the results of DJS can be reproduced. Note however that DJS use a filter seven times the rms perturbation, but a filter of five is found to give the best agreement. This is probably due to the additional filtering originating from the slower sampling in DJS' measurements.

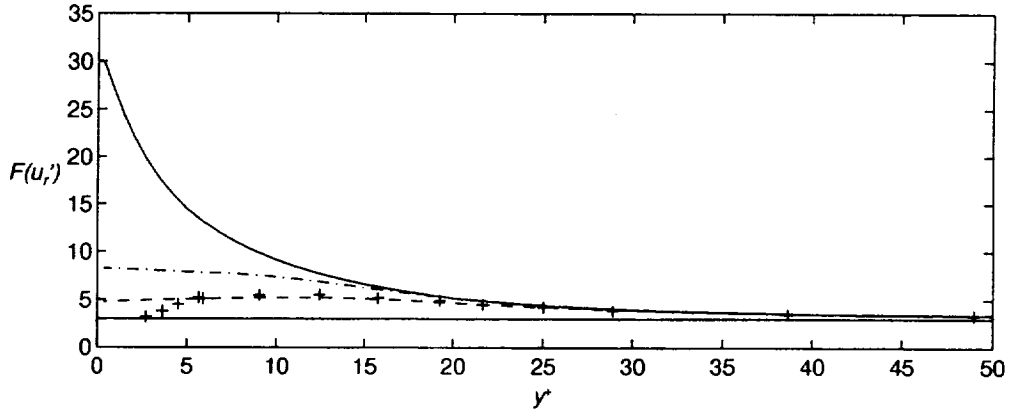

Figure 3.24: Flatness of the radial perturbation with different filters: —— no filter, ---- $|u_r'/u_{r\,\mathrm{rms}}| \leq 5$, -·-·- $|u_r'/u_{r\,\mathrm{rms}}| \leq 7$.

Xu *et al.* attributed the success of DNS in calculating accurate flatness to the nature of the averaging process: for DNS, at each radial location averages are computed on cylindrical surfaces, such as the one shown in figure 3.14, whereas for experiments they are measured on lines, which greatly reduces statistical accuracy.

3.2.5 Budgets of turbulence transport equations

The transport equations for the Reynolds stresses were derived for cylindrical coordinates in Moser and Moin [25]; in tensor form they are given by (e.g. see Mansour *et al.* [22, 23])

$$\frac{\bar{D}}{Dt}\overline{u_i'u_j'} = P_{ij} + T_{ij} + D_{ij} + \Pi_{ij} - \varepsilon_{ij} \tag{3.11}$$

where $\bar{D}/Dt = \partial/\partial t + U_k \partial/\partial x_k$, U_k is the mean velocity and the terms on the right hand side of 3.11 are given by

$P_{ij} = -\left(\overline{u_i'u_k'}U_{j,k} + \overline{u_j'u_k'}U_{i,k}\right)$	Production
$\varepsilon_{ij} = 2\nu\overline{u_{i,k}'u_{j,k}'}$	Dissipation
$T_{ij} = -\left(\overline{u_i'u_j'u_k'}\right)_{,k}$	Turbulent transport
$D_{ij} = \nu\left(\overline{u_i'u_j'}\right)_{,kk}$	Viscous diffusion
$\Pi_{ij} = -\left(\overline{u_i'p_{,j}' + u_j'p_{,i}'}\right)/\rho$	Velocity pressure-gradient

where indices after the comma refer to covariant derivatives. A transport equation for the turbulent kinetic energy, defined as $k = \frac{1}{2}\overline{u_i' u_i'} = \frac{1}{2}(\overline{u_r' u_r'} + \overline{u_\theta' u_\theta'} + \overline{u_z' u_z'})$ (sum on repeated roman indices), can be obtained by taking the trace of 3.11. It is also customary to split the velocity pressure-gradient term into a pressure-strain (ΠS_{ij}) and a pressure-diffusion term (ΠD_{ij}), where

$$\Pi S_{ij} = 2\overline{p' s_{ij}}, \tag{3.12}$$

$s_{ij} = 1/2(u_{i,j}' + u_{j,i}')$ and $\Pi D_{ij} = \Pi_{ij} - \Pi S_{ij}$. In this form, the pressure-strain term redistributes energy among the different components.

Figure 3.25 (a)–(d) give the budgets of the four non-zero stresses. The equations are nondimensionalized by u_τ and ν. One is struck by the close similarity between the pipe and channel results of Mansour, Kim and Moin [22, 23]. Some differences can be seen in the budgets of $\overline{u_r' u_r'}$ and $\overline{u_\theta' u_\theta'}$ but those were found to be very sensitive to the statistical sampling. Many more samples would have to be collected to attribute the differences to geometry. In this low Reynolds number range, nondimensionalization with respect to u_τ and ν will not completely remove Reynolds number effects which probably accounts for most of the discrepancies.

The budget for the $\overline{u_z' u_z'}$ component is dominated by production and dissipation. Production reaches a maximum at $y^+ \approx 12$ and is balanced by dissipation, turbulent transport and viscous diffusion; the minima in turbulent transport and viscous diffusion occur on each side of the peak in production, or respectively $y^+ \approx 14$ and $y^+ \approx 9$, indicating transport away from the point of peak production. At the wall, production, turbulent transport and the velocity pressure-gradient terms are zero by the no-slip condition and viscous diffusion balances dissipation. The velocity pressure-gradient term is negative throughout the pipe indicating a transfer of energy from $\overline{u_z' u_z'}$ to the other components; for the streamwise and azimuthal components, the velocity pressure-gradient and pressure-strain terms are identical. In the budgets of $\overline{u_r' u_r'}$ and $\overline{u_\theta' u_\theta'}$, the velocity pressure-gradient term is the major source of production; with only $\partial U_z/\partial r$ non-zero, production is identically zero for these two components. Figure 3.26 shows the pressure-strain terms for the normal stresses plotted together. The transfer

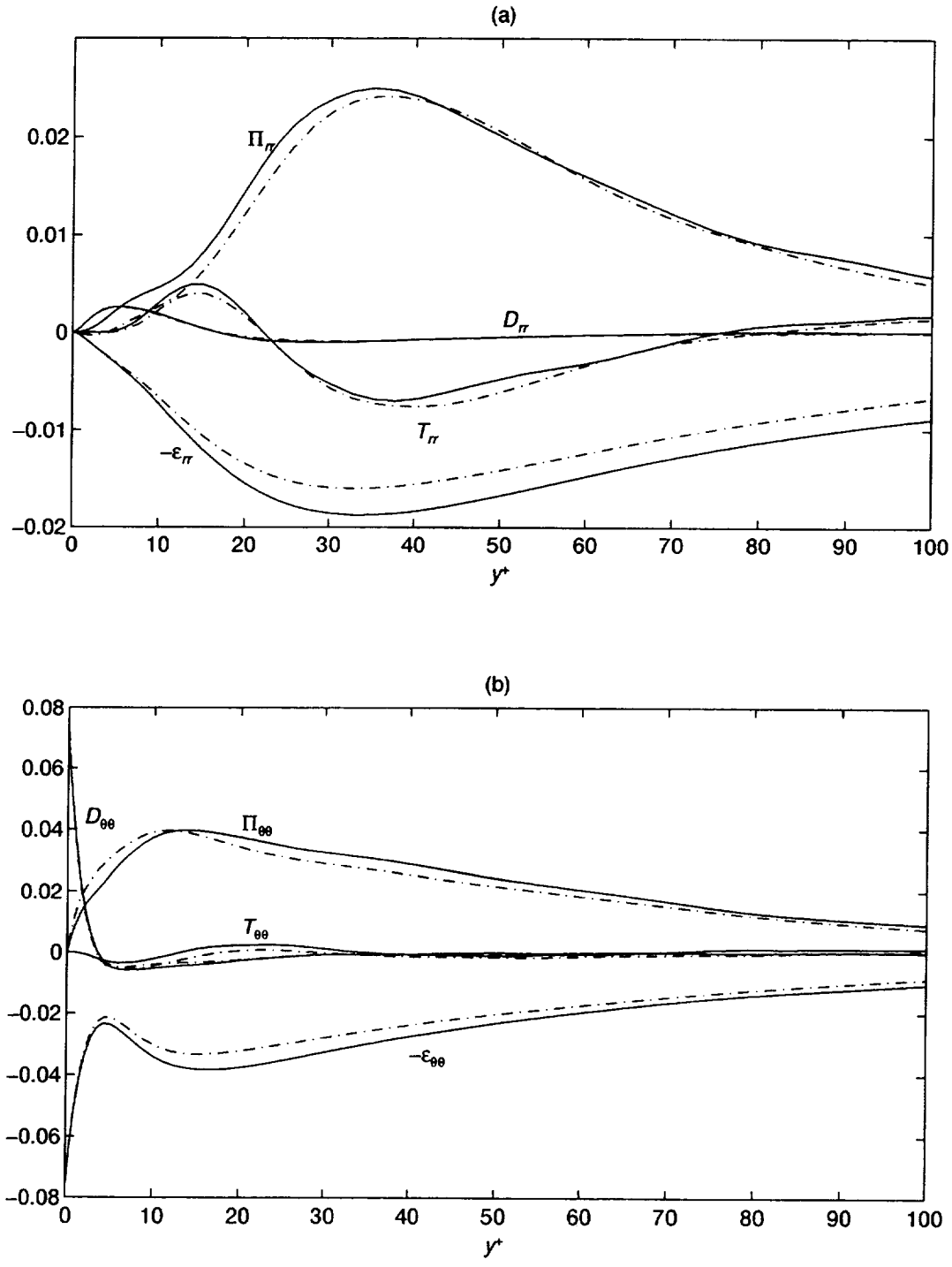

Figure 3.25: See caption page 69.

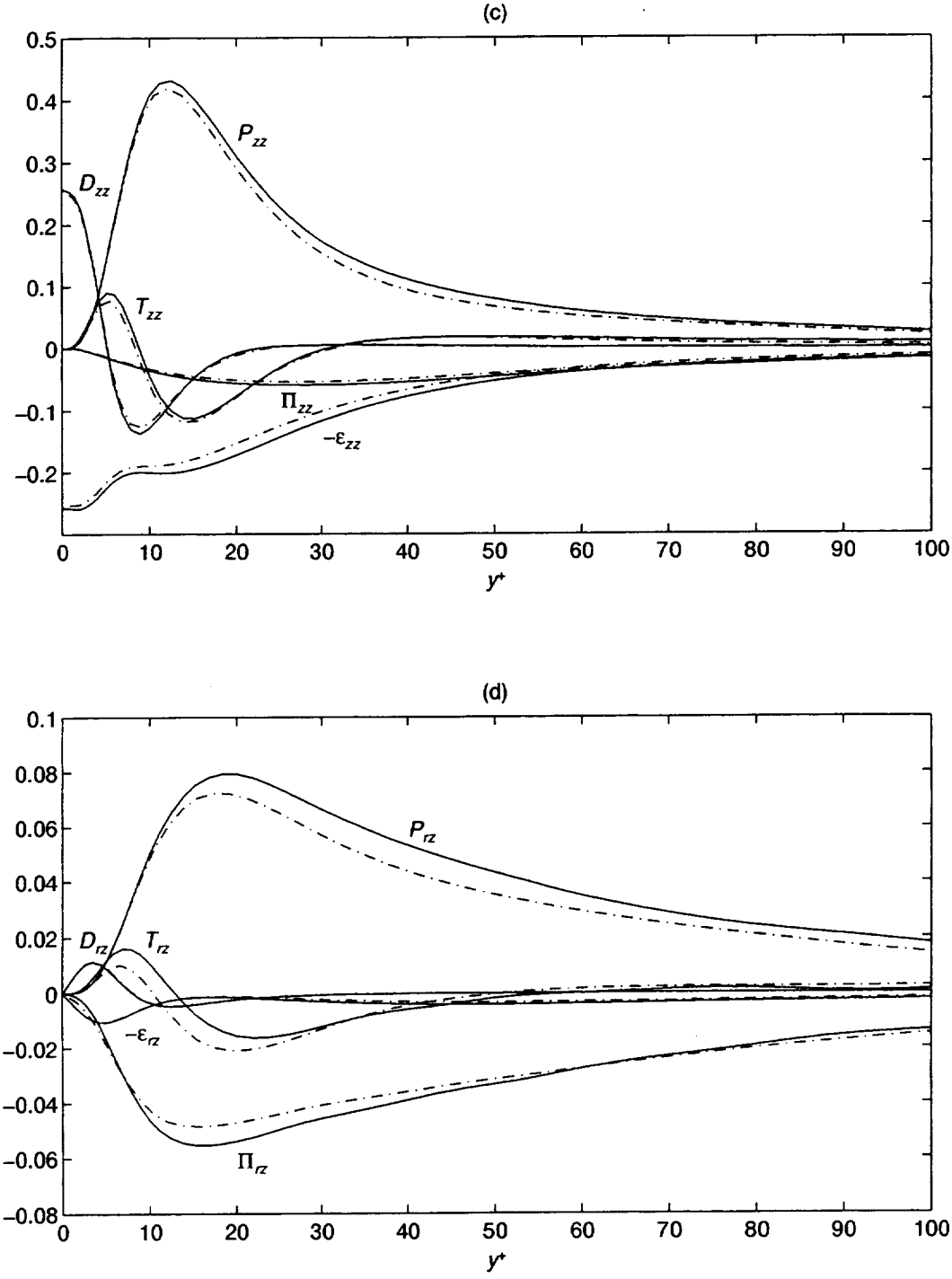

Figure 3.25: Budgets of the Reynolds stress transport equation: (a) $\overline{u_r'u_r'}$, (b) $\overline{u_\theta'u_\theta'}$, (c) $\overline{u_z'u_z'}$ and (d) $\overline{u_r'u_z'}$. B-splines ——, channel (Mansour *et al.* [22, 23]) – · – · –.

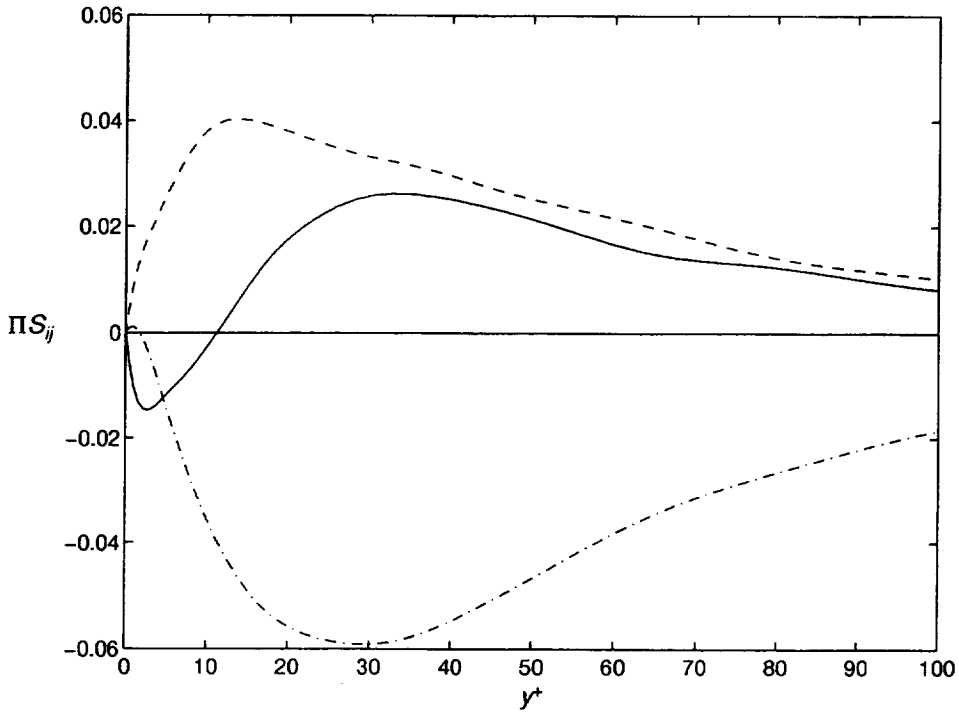

Figure 3.26: Pressure-strain correlation tensor (ΠS_{ij}) for the pipe; ΠS_{rr} ——, $\Pi S_{\theta\theta}$ - - - -, ΠS_{zz} – · – · –.

of energy from the streamwise to the cross-stream components is evident. However, near the wall ($y^+ < 12$) there is a transfer of energy from the radial component to the other two components. This was also observed by Moin and Kim [24] and Moser and Moin [25] in channel flows. Moin and Kim attributed this to the impingement of fluid coming from the center, hitting the wall, and transferring energy to the other components.

Other terms of the budgets for the $\overline{u_r' u_r'}$ and $\overline{u_\theta' u_\theta'}$ components are balanced by dissipation, with the remaining terms playing little role, expect in the case of the azimuthal component where viscous diffusion balances dissipation at the wall. The $\overline{u_r' u_z'}$ budget is almost completely dominated by production and the velocity pressure-gradient terms balancing each other; for $y^+ > 15$, the other terms are virtually zero except for a small residual part coming from the turbulent transport term.

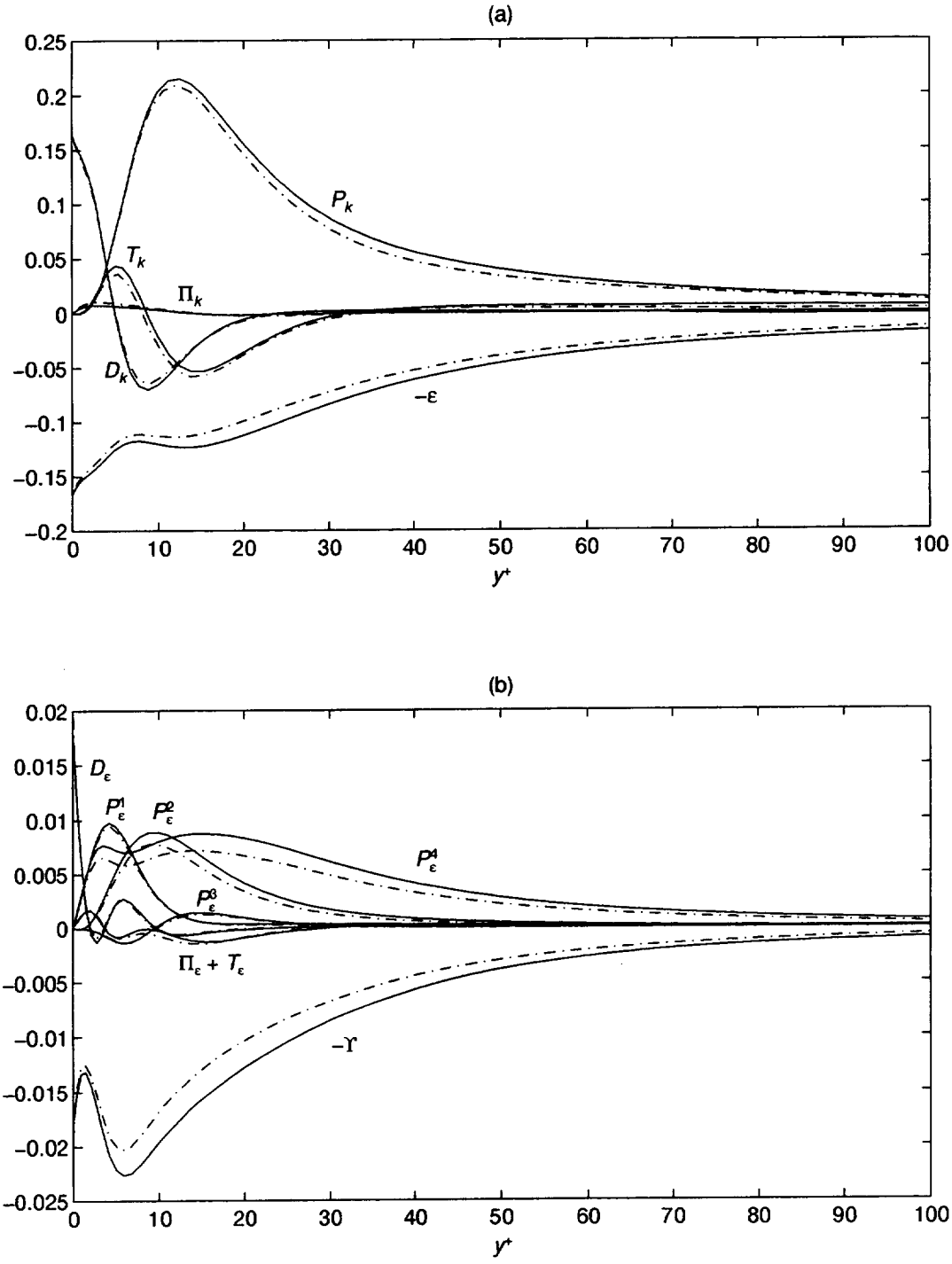

Figure 3.27: Budgets of the turbulent kinetic energy equation (a) and dissipation equation (b). B-splines ——, channel (Mansour *et al.* [22, 23]) – · – · –.

Figure 3.27 give the budgets for the turbulent kinetic energy (a) and dissipation equation (b) (k and ε budgets). Again, similarity with the channel budgets of Mansour, Kim and Moin [22, 23] is evident; differences are most probably caused by Reynolds number effects. The k budget closely resembles the $\overline{u'_z u'_z}$ budget since this term dominates $\overline{u'_r u'_r}$ and $\overline{u'_\theta u'_\theta}$. In the k budget however, the velocity pressure gradient reduces to the pressure-diffusion term, i.e. $\Pi_{ij} \equiv \Pi D_{ij}$, since the trace of the pressure-strain term is identically zero.

If one defines the dissipation of turbulent kinetic energy, $\varepsilon = \varepsilon_{ii}/2$, a transport equation for the dissipation is given by

$$\frac{\bar{D}}{Dt}\varepsilon = P_\varepsilon^1 + P_\varepsilon^2 + P_\varepsilon^3 + P_\varepsilon^4 + T_\varepsilon + \Pi_\varepsilon + D_\varepsilon - \Upsilon \tag{3.13}$$

where

$P_\varepsilon^1 = -\nu\overline{u'_{i,j}u'_{k,j}}S_{ik}$	Mixed production
$P_\varepsilon^2 = -\nu\overline{u'_{i,k}u'_{i,m}}S_{km}$	Production by mean velocity gradient
$P_\varepsilon^3 = -\nu\overline{u'_k u'_{i,m}}U_{i,km}$	Gradient production
$P_\varepsilon^4 = -\nu\overline{u'_{i,k}u'_{i,m}u'_{k,m}}$	Turbulent production
$T_\varepsilon = -(\nu/2)\left(\overline{u'_k u'_{i,m}u'_{i,m}}\right)_{,k}$	Turbulent transport
$\Pi_\varepsilon = -(\nu/\rho)\left(\overline{p'_{,m}u'_{k,m}}\right)_{,k}$	Pressure transport
$D_\varepsilon = (\nu/2)\varepsilon_{,kk}$	Viscous diffusion
$\Upsilon = \nu^2\overline{u'_{i,km}u'_{i,km}}$	Dissipation

where $S_{ij} = 1/2(U_{i,j} + U_{j,i})$ is the mean strain rate tensor.

The ε budget also shows great similarity with the channel. Beyond the buffer layer, dissipation balances turbulent production; closer to the wall, most terms have positive contribution to the ε balance with the dissipation term contributing for the losses. It should be noted that the dissipation term Υ is computed by summing all the terms in the ε equation and not by direct computations (this term involves third order tensors which makes its computation non-trivial). Away from the wall ($y^+ > 30$)

turbulent production (P_ε^4) and dissipation (Υ) dominate the balance. However closer to the wall, both P_ε^1 and P_ε^2 are of the same order as P_ε^4. All terms become zero at the wall except for viscous diffusion which balances dissipation. P_ε^3, $\Pi_\varepsilon + T_\varepsilon$ and D_ε play virtually no role in the balance, except for D_ε which reaches a maximum at the wall to balance Υ.

3.2.6 New structure tensors

Kassinos, Reynolds and Rogers [16] (hereinafter referred to as KRR) (see also Reynolds [35]) introduced a new family of one-point tensors to provide information about the structure, or *dimensionality* of turbulence. Standard turbulence models based on the Reynolds stress transport equation (see above) provide information about the *componentality* of turbulence (e.g. $R_{rr} = R_{r\theta} = R_{zz} = 0$ if $u_r' = 0$) but none about its dimensionality.

KRR defined a family of new tensors based on the turbulent stream function; let

$$u_i' = \epsilon_{ijk}\psi_{k,j}', \quad \text{with} \quad \psi_{i,i}' = 0, \quad \text{which implies} \quad \psi_{i,kk}' = -\omega_i' \tag{3.14}$$

where ϵ_{ijk} is the permutation tensor. Because ψ_i (dropping the primes for convenience) satisfies a Poisson equation, it carries non-local information about the velocity field (like pressure). Using 3.14, KRR defines

$$R_{ij} + D_{ij} + F_{ij} + C_{ij} + C_{ji} = \delta_{ij}q^2 \tag{3.15}$$

where δ_{ij} is the Kronecker delta, $q^2 = R_{ii}$ and

$R_{ij} = \overline{u_i u_j} = \epsilon_{ipq}\epsilon_{jts}\overline{\psi_{q,p}\psi_{s,t}}$	Reynolds stress tensor
$D_{ij} = \overline{\psi_{k,i}\psi_{k,j}}$	Structure dimensionality tensor
$F_{ij} = \overline{\psi_{i,k}\psi_{j,k}}$	Structure circulicity tensor
$C_{ij} = \overline{\psi_{i,k}\psi_{k,j}}$	Structure inhomogeneity tensor

All of the above tensors are symmetric, except for C_{ij}. Although 3.15 involves a

tensor given by $C_{ij} + C_{ji}$ which is itself symmetric.

To compute the stream function ψ_i, instead of solving directly the Poisson equations shown in 3.14, use is made of the stream functions defined in talbe B.1. However, if the definitions shown above are to hold, the stream functions have to be made solenoidal; let

$$\psi_i = \Psi_i + \Phi_{,i} \tag{3.16}$$

where Ψ_i are the stream functions from table B.1 and $\Phi_{,i}$ represents the gradient of an arbitrary scalar potential. Because $\epsilon_{ijk}\Phi_{,kj} = 0$ ($\nabla \times \nabla\Phi = 0$), the velocity is identically given by $u_i = \epsilon_{ijk}\psi_{k,j} = \epsilon_{ijk}\Psi_{k,j}$. Taking the divergence of 3.16, and assuming ψ_i is constant at the wall, the following Poisson equation and associated boundary condition are obtained

$$\Phi_{,ii} = -\Psi_{i,i} \qquad \text{with} \qquad \left.\frac{\partial\Phi}{\partial r}\right|_{R_2} = -\frac{1}{R_2}\int_0^{R_2} \frac{\partial\Psi_r}{\partial r}\, r\, dr \tag{3.17}$$

Thus, solving for Φ requires the solution of only one Poisson equation instead of three for ψ.

Figure 3.28 give the normalized structure circulicity and dimensionality tensors. The circulicity tensor provides information about the vorticity field (for homogeneous turbulence, KRR show that F_{ij} is directly related to the vorticity spectrum Ω_{ij}). As its name imply, D_{ij} reveals information about the dimensionality of the flow. As shown in figure 3.28 (b), the streamwise (d_{zz}) value reaches a minimum at $y^+ \approx 10$ indicating that the streamwise motion is nearly 2D, aligned with the z axis; circulicity (f_{zz}) is also relatively small indicating very little circulation along the axis. This, and the peak in the streamwise component of the normalized Reynolds stress (figure 3.29 (b)) are consistent with the presence of wall streaks; KRR also noted this behavior for the channel. They refer to this type of motion as *jetal*, or jet-like behavior. Also, d_{rr} reaches a maximum and $d_{\theta\theta}$ a minimum at the same location, indicating that the structures vary more rapidly in the radial than in the azimuthal direction, which means the streaks have a larger spanwise than radial extent. As seen in figure 3.29 (a), the wall is also the zone of greatest inhomogeneity, with the normal components

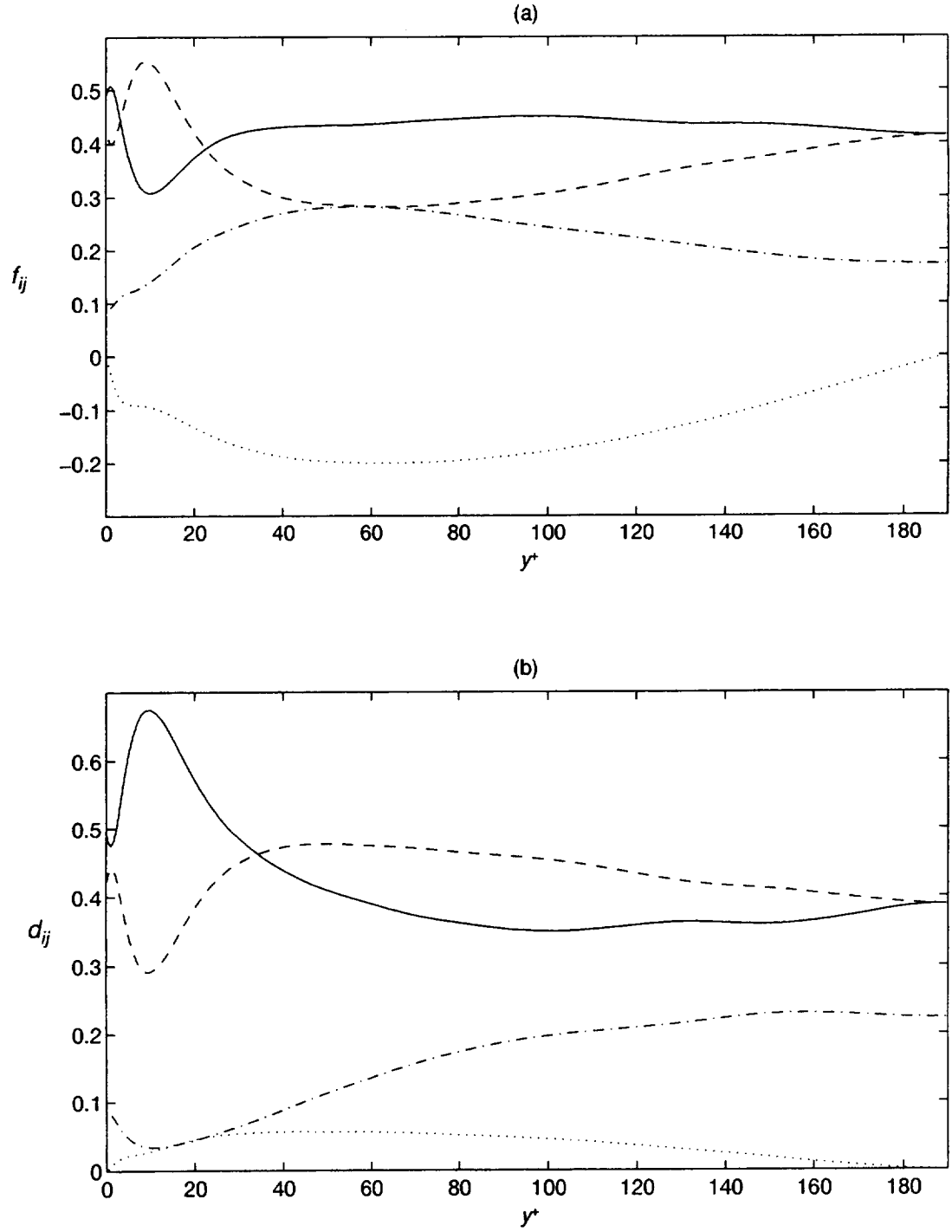

Figure 3.28: Structure circulicity ($f_{ij} = F_{ij}/F_{kk}$) and structure dimensionality ($d_{ij} = D_{ij}/D_{kk}$) tensors; symbols are for radial component ——, azimuthal - - - -, streamwise -·-·- and cross-term ·····.

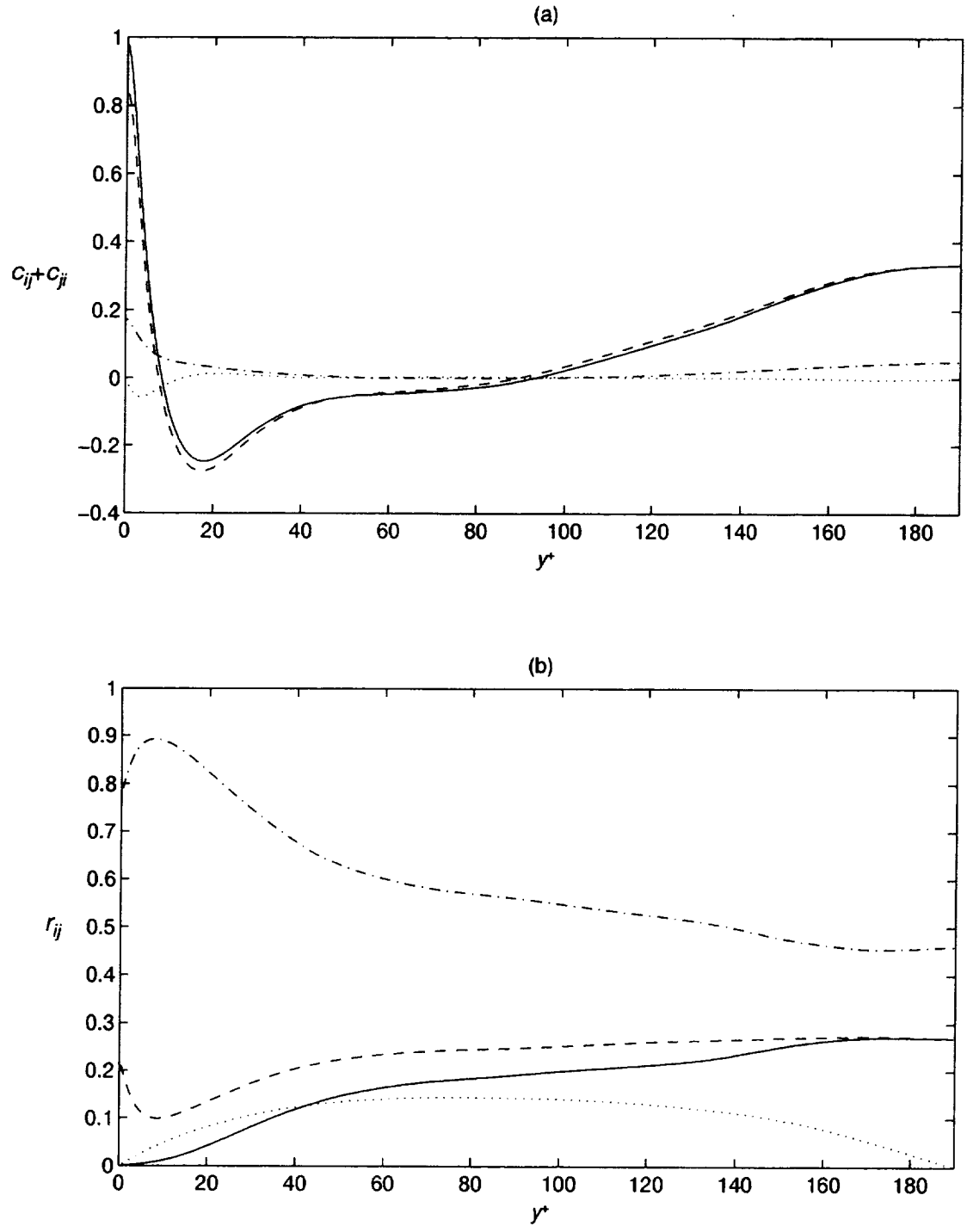

Figure 3.29: Symmetrized structure inhomogeneity ($c_{ij} + c_{ji} = (C_{ij} + C_{ji})/D_{kk}$) and Reynolds stress ($r_{ij} = R_{ij}/q^2$) tensors; symbols as for fig. 3.28.

of the symmetrized inhomogeneity tensor reaching their maxima at the wall.

Close to the center, the flow is more 3D with d_{zz} begin somewhat lower than d_{rr} and $d_{\theta\theta}$; the structure circulicity tensor also exhibits a similar behavior. The flow is still jet-like but less so than near the wall. KRR noted the same behavior of d_{ij} and f_{ij} for the channel. However an important difference is seen in the inhomogeneity tensor: KRR observed that the flow was nearly homogeneous near the center (or at least in the log region) which is not the case for the pipe. Both c_{rr} and $c_{\theta\theta}$ show significant inhomogeneity throughout the pipe.

Chapter 4

Flow Topology

This chapter presents a brief description of a topological method used to analyze flow structures. This method is then applied to flow fields of the fully developed pipe simulation presented in chapter 3.

4.1 Topological Approach

One of the fundamental difficulties in analyzing the structure of turbulent flows computed via numerical simulations is the large amount of information produced by the simulations and the apparent lack of coherence of the flow field. DNS typically contain several million grid points (2.2 million for the present work), on which three velocity components and pressure are computed. To analyze the structure of turbulent flows, Perry and Chong [33] introduced a method based on critical point theory. Their approach was later extended by Chong, Perry and Cantwell [9] who introduced a general classification of flow fields by analyzing the invariants of the velocity gradient tensor. This method reduces complex three-dimensional, incompressible flow fields to two-dimensional plots of joint probability density functions (PDF) of the invariants of the velocity gradient tensor. The information provided by the PDF is essentially qualitative in nature, revealing general, overall trends rather than in depth, or detailed flow features.

4.1.1 Description

A complete description of critical point theory was given in Chong *et al.* [33] and is not repeated here; for the present purpose, a short summary is included for completeness, and closely follows Sondergaard [42] and Blackburn, Mansour and Cantwell [4] (hereinafter referred to as BMC). Define

$$A_{ij} = u_{i,j} \tag{4.1}$$

to be the velocity gradient tensor; again, indices after the comma refer to covariant derivative. A_{ij} can be split into a symmetric and skew-symmetric parts

$$A_{ij} = S_{ij} + W_{ij} \tag{4.2}$$

where

$$S_{ij} = \frac{1}{2}\left(u_{i,j} + u_{j,i}\right) \tag{4.3}$$

is the symmetric strain-rate tensor and

$$W_{ij} = \frac{1}{2}\left(u_{i,j} - u_{j,i}\right) \tag{4.4}$$

is the skew-symmetric rotation-rate tensor. The eigenvalues of A_{ij} satisfy the characteristic equation given by

$$\lambda^3 + P\lambda^2 + Q\lambda + R = 0 \tag{4.5}$$

where P, Q and R are the invariants of A_{ij} and are given by

$$P = -S_{ii} \tag{4.6}$$

$$Q = \frac{1}{2}\left(P^2 - S_{ij}S_{ji} - W_{ij}W_{ji}\right) \tag{4.7}$$

$$R = \frac{1}{3}\left(-P^3 + 3PQ - S_{ij}S_{jk}S_{ki} - 3W_{ij}W_{jk}S_{ki}\right) \tag{4.8}$$

where P, Q and R are respectively the trace, the sum of the determinants of the cofactors, and the determinant of $\mathbf{A}$. For incompressible flow, the first invariant is identically zero by continuity,

$$P = 0 \tag{4.9}$$

and only Q and R determine the eigenvalues of $\mathbf{A}$; the discriminant of 4.5 becomes

$$D = \frac{27}{4}R^2 + Q^3 \tag{4.10}$$

$D > 0$ yields one real and two complex conjugate eigenvalues; $D < 0$ yields three real eigenvalues, and $D = 0$ gives three real eigenvalues, of which two are repeated. For this last case the invariants lie on the lines $R = \pm(2\sqrt{3}/9)(-Q)^{3/2}$.

Figure 4.1 shows the flow topology as a function of Q, R and the discriminant D. Each of the four region can be characterized as follows:

- Stable focus/stretching ($R < 0$, $D > 0$): for this topology, the flow spirals in toward the origin and flows out along an axis perpendicular to the spiraling plane (analogous to vortex stretching).

- Unstable focus/compressing ($R > 0$, $D > 0$): here the flow approaches the origin from one direction and spirals out in a plane perpendicular to the approaching direction.

- Stable node/saddle/saddle ($R < 0$, $D < 0$): the flow approaches the origin from two directions and flows out from the third one (analogous to a stagnation point).

- Unstable node/saddle-saddle ($R > 0$, $D < 0$): the flow approaches the origin from one direction and flows out from the other two.

Other quantities of interest are the invariants of the strain-rate tensor S_{ij}:

$$Q_s = -\frac{1}{2}S_{ij}S_{ji} \tag{4.11}$$

$$R_s = -\frac{1}{3}S_{ij}S_{jk}S_{ki} \tag{4.12}$$

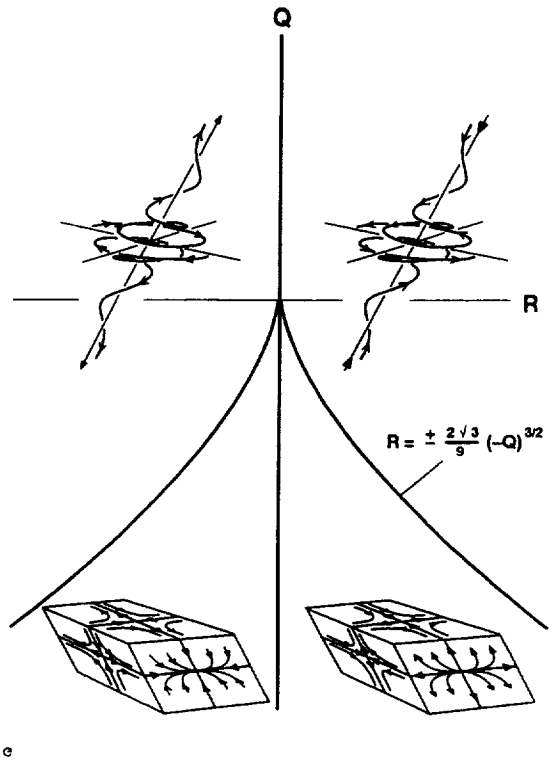

Figure 4.1: Invariant space for incompressible flow. The streamlines give the flow classification: upper left, stable focus/stretching; upper right, unstable focus/compressing; lower left, stable node/saddle/saddle; lower right, unstable node/saddle/saddle.

Because S_{ij} is symmetric, all eigenvalues fall below the line $D = 0$ in figure 4.1. Blackburn *et al.* showed that joint PDF plots in Q_s, R_s space provide information about the principal direction of strains. Using scaling arguments proposed by Chen *et al.* [8], they suggest that fine scale motion should lie far from the origin in Q_s, R_s space. Also, one should note that Q_s is proportional to the mechanical dissipation of kinetic energy $\phi = 2\nu S_{ij}S_{ji} = -4\nu Q_s$, so that regions of large dissipation are identified by regions of large negative values of Q_s.

Also, plots of Q_s versus the second invariant of W_{ij}, Q_w,

$$Q_w = -\frac{1}{2}W_{ij}W_{ji} \tag{4.13}$$

reveal relative importance of straining versus rotation. Since Q_w is proportional to the enstrophy ($\omega_i\omega_i$), it provides information about the rotation of the flow.

4.1.2 Results

The method of using invariants of the velocity gradient and other associated tensors was used by Soria *et al.* [43] to study the topology of incompressible mixing layers, Chen *et al.* [8] for compressible and incompressible mixing layers, Sondergaard [42] for transitional wakes, and BMC for fully developed turbulent channel flow.

Figure 4.2 (a)-(d) give the joint PDF in (Q, R) space for a single realization at four radial locations, each in a different region of the flow: viscous, buffer, logarithmic and wake region. For all regions, except close to the wall, the distribution in (Q, R) space shows a preference for the second and fourth quadrant, while close to the wall the distribution is almost circular with no preference for any quadrant. Cantwell [6] showed that under certain assumptions (one of them being inviscid flow), the preference of the invariants to line-up in the second and fourth quadrants in a "skewed teardrop" shape is an actual solution to the Navier-Stokes equations. These results are in agreement with the findings of BMC in channel flow. The high level of noise near the center is again due to the fewer number of modes which degrades sampling (c.f. figure 3.10). The behavior near the center is consistent with the topology observed in free shear flows, i.e. stable focus/stretching and unstable node/saddle/saddle.

Figure 4.3 (a)-(d) show plots of the second and third invariants of the strain-rate tensor, for the same four radial locations. Since the strain-rate tensor is symmetric, all the eigenvalues are real and lie in the region of negative discriminant ($D < 0$). Away from the wall there is a clear preference for the unstable node/saddle/saddle topology. As the wall is approached, the preference for the unstable node/saddle/saddle topology is no longer observed, and very close to the wall the probability tends to cluster close to the $R_s = 0$ line. This is in agreement with BMC's findings for channel flow; they also showed that at the wall $R_s = 0$. The $R_s = 0$ line corresponds to the case of purely two-dimensional strain; if one orders the eigenvalues of S_{ij} such that $\lambda_1 > \lambda_2 > \lambda_3$, then for $R_s = 0$, correspond $\lambda_2 = 0$. As with the structure tensors

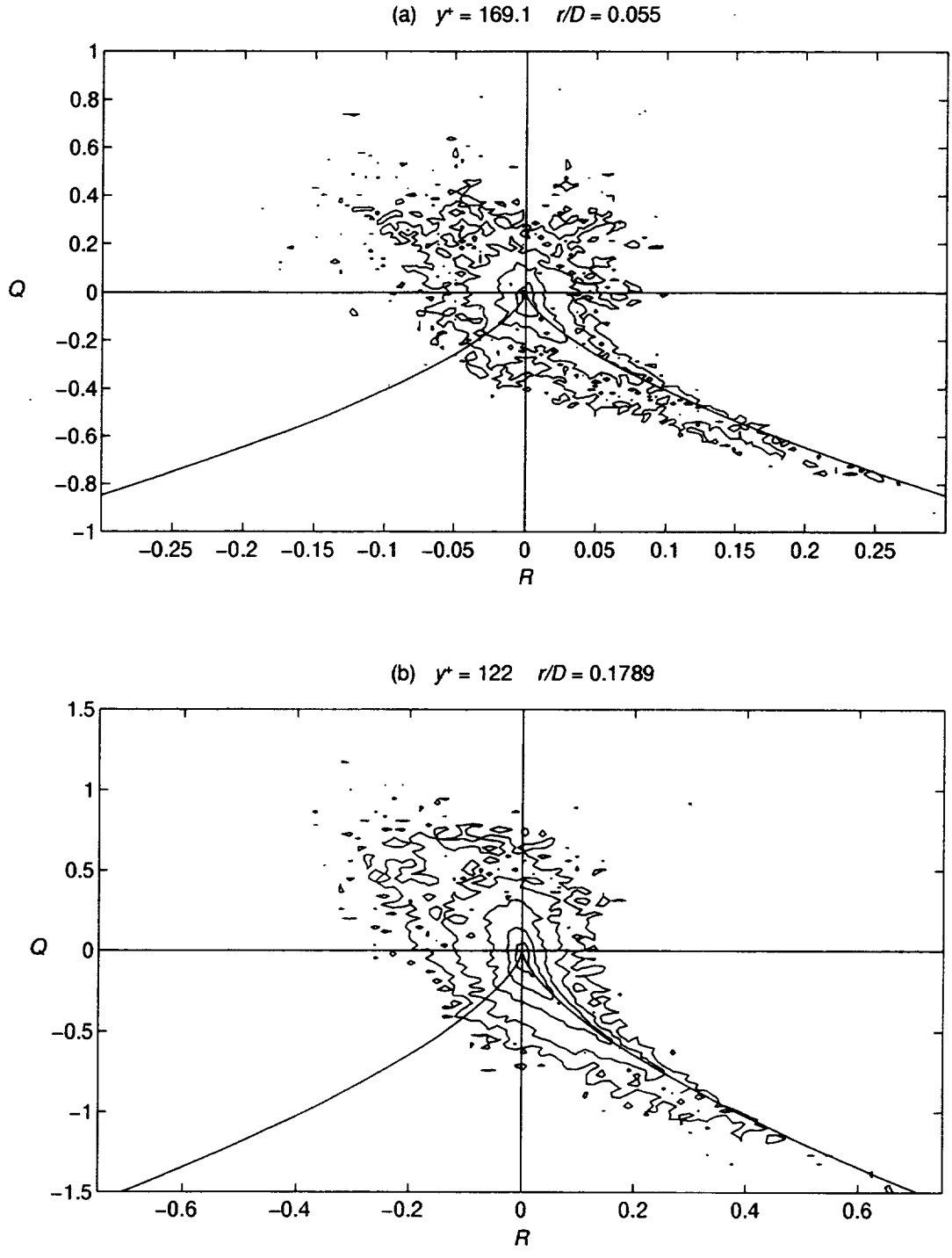

Figure 4.2: See caption page 85.

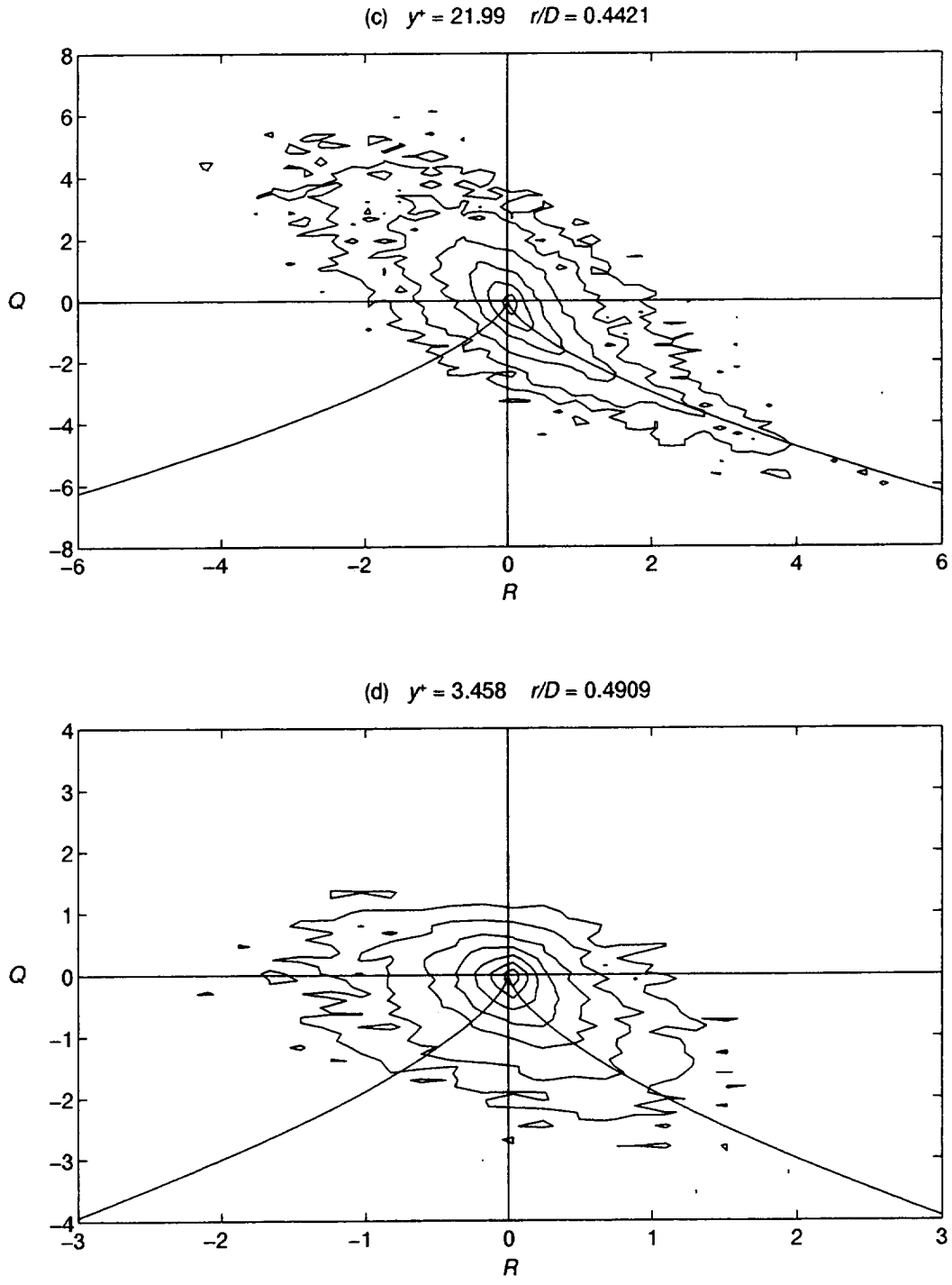

Figure 4.2: Contour plot of joint PDF ($\log_{10}$) of Q and R. Contour levels are from the exterior toward the interior: (a) and (b) 0.5-2.5, (c) 0.5-3.0 and (d) 0.5-3.5 by half decade increments (0.5).

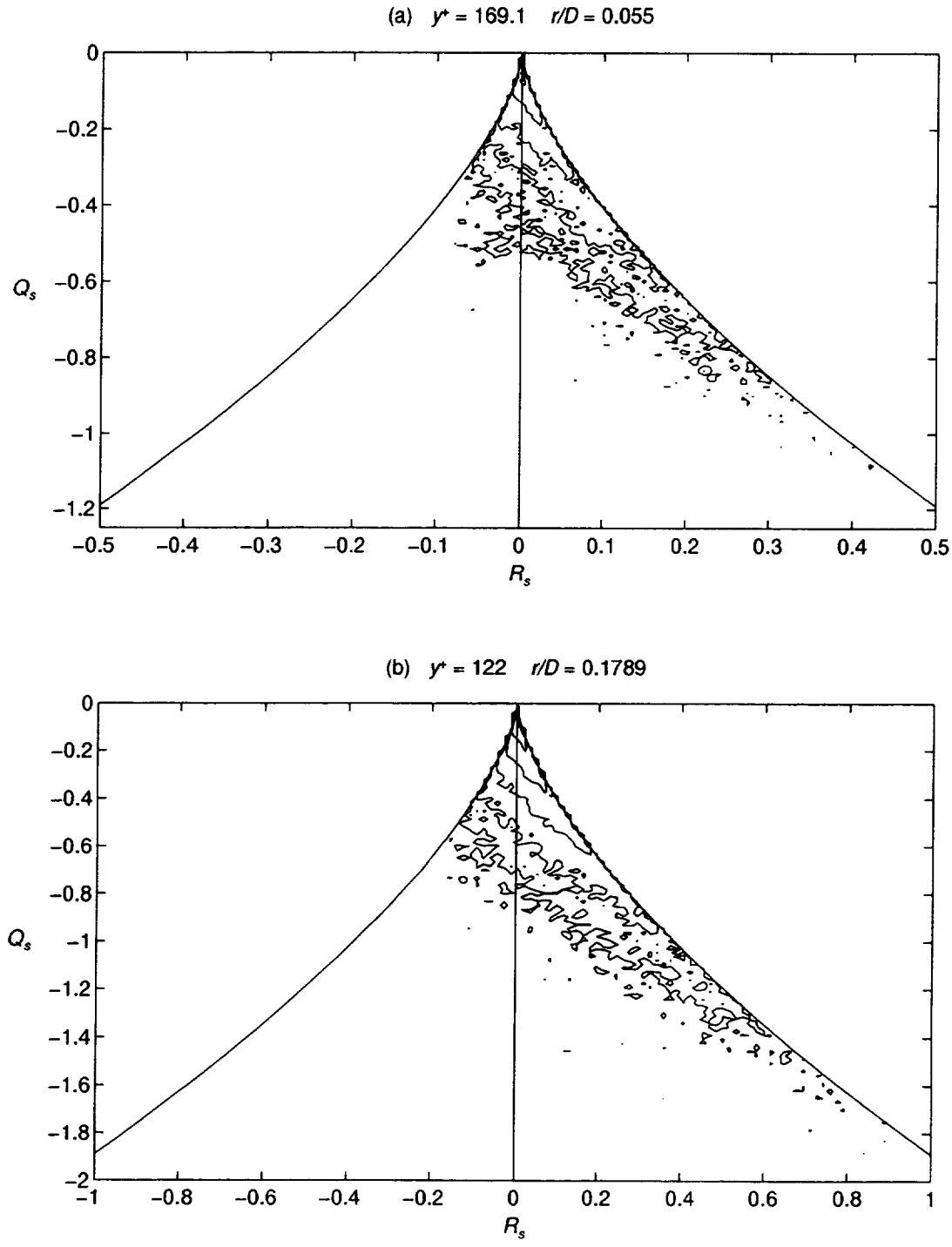

Figure 4.3: See caption page 87.

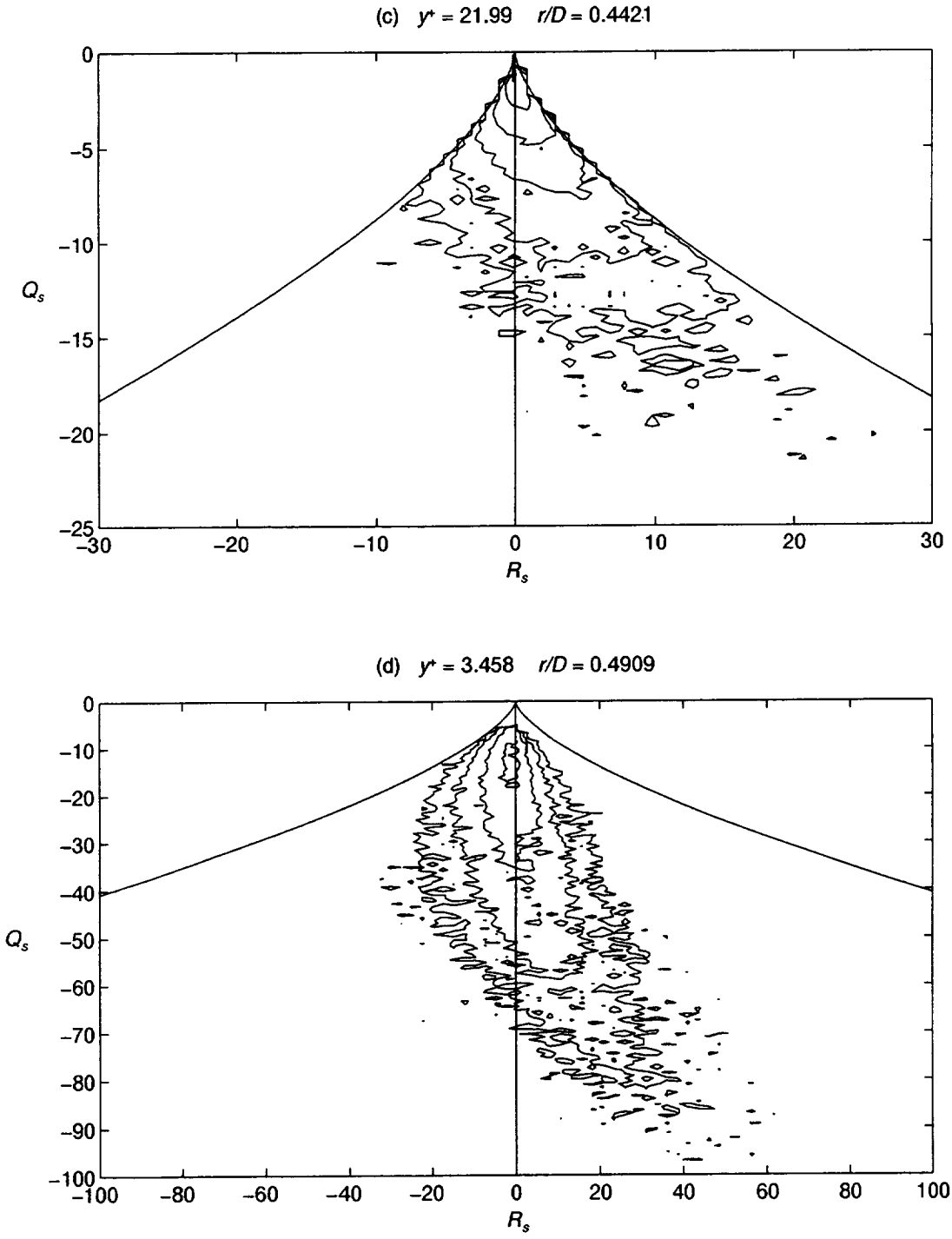

Figure 4.3: Contour plot of joint PDF ($\log_{10}$) of Q_s and R_s. Contour levels are from the bottom toward the origin: (a)-(c) 0.5-2.5, (d) 0.5-2.0 by half decade increments (0.5).

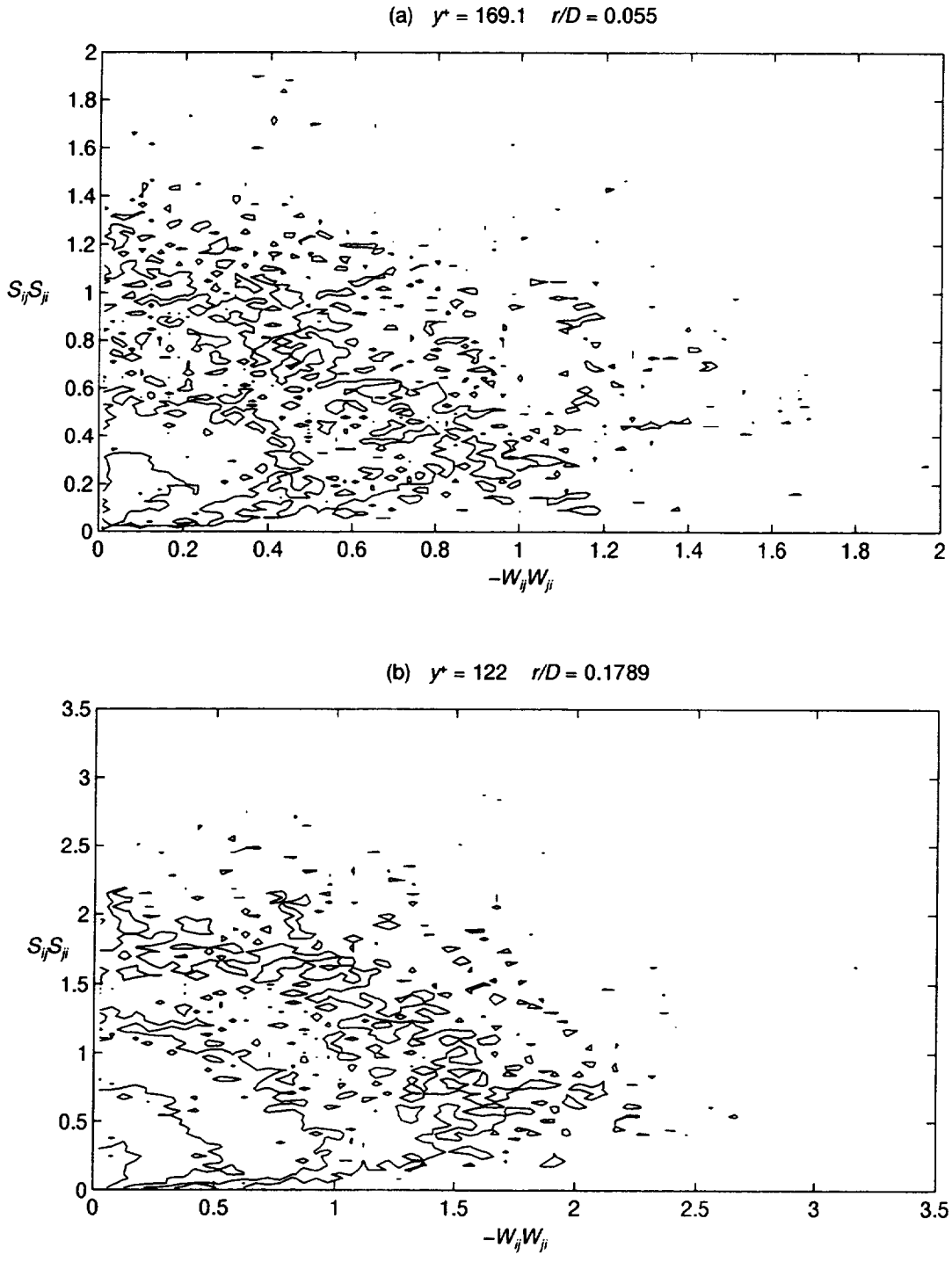

Figure 4.4: See caption page 89.

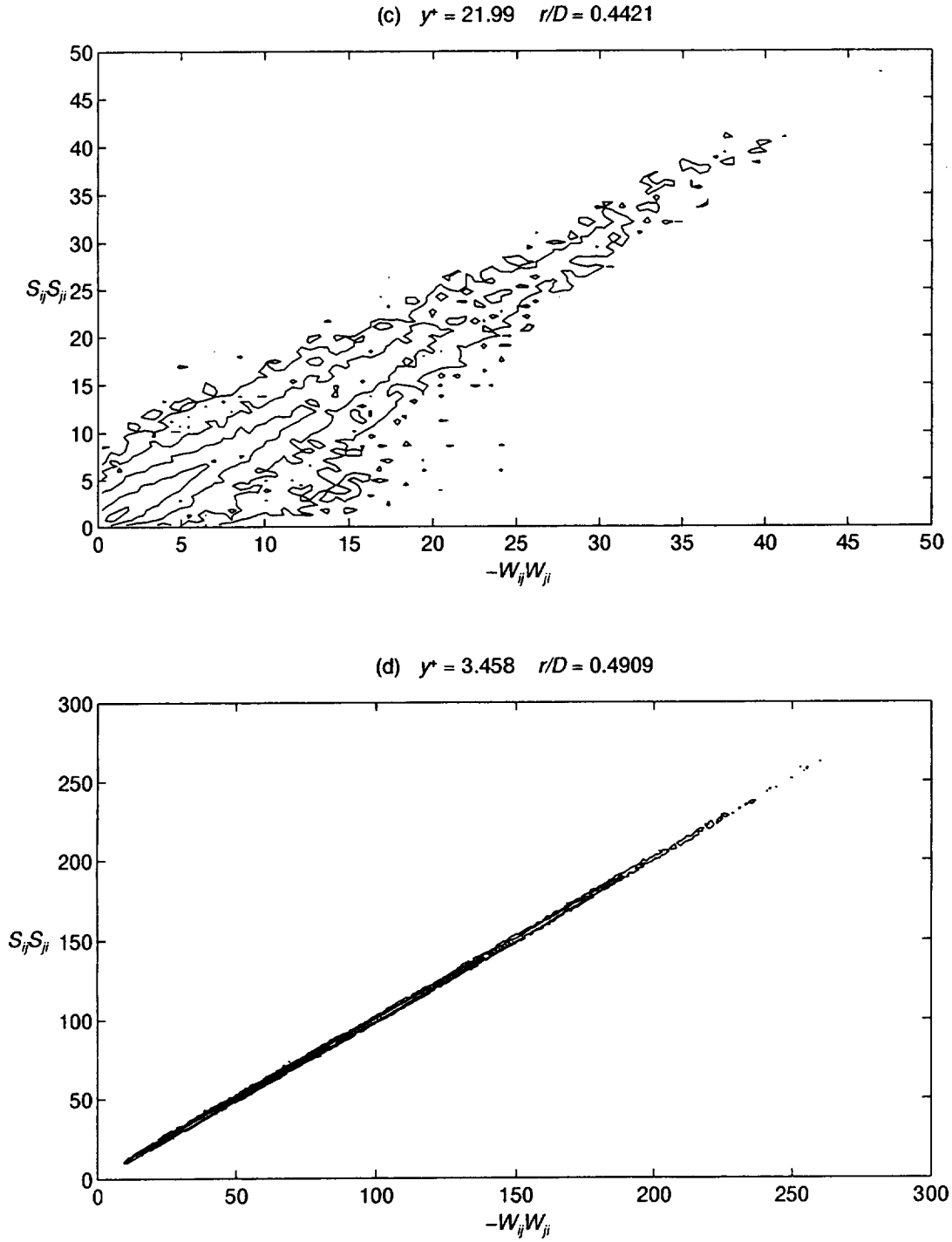

Figure 4.4: Contour plot of joint PDF ($\log_{10}$) of $S_{ij}S_{ji}$ and $-W_{ij}W_{ji}$. Contour levels are from the outside in: (a) 0.5-1.5, (b) 0.5-2 and (c) 0.5-2.5 by half decade increments (0.5). Levels for (d) collapse onto a single 45° line.

(section 3.2.6), the invariants provide information about the dimensionality of the flow field.

Plots of $S_{ij}S_{ij}$ versus $-W_{ij}W_{ij}$ are shown in figures 4.4 (a)-(d). Very close to the wall, the results collapse onto a single 45° line, indicating that dissipation and enstrophy are identical. This type of topology is analogous to a vortex sheet. In the buffer layer, the results still maintain a 45°-like behavior but much more losely, whereas further out in the flow, the results look like that of free shear flows (e.g. Sondergaard [42]). Plots (a) and (b) also show an interesting feature: the contours never reach a value of zero strain, but can reach zero rotation. This implies that although pure strain is possible, no point in the flow is in solid-body rotation.

4.2 Vortices

One of the more interesting features in pipe flow and wall-bounded flows in general, are streamwise vortices. There lies a great difficulty in identifying vortices in turbulent flows, since there is no universally adopted definition of a vortex. For example, if one relies solely on vorticity magnitude, the region near the wall possesses the largest vorticity but yet has no vortex, hence the difference between vortex-sheet and tube-like vortices or vortical eddies (see for example Chong *et al.* or Jeong and Hussain [14]).

A topological method, such as the one used in section 4.1, can be used to identify the regions of the flow where tube-like vortices are present. Figure 4.1 shows that regions with positive discriminant have streamlines spiraling around the principal axis. So regions of the flow with $D > 0$, i.e. where the eigenvalues of A_{ij} are complex, should correspond to regions of (tubular) vorticity. However, Jeong and Hussain [14] suggested that this criterion ($D > 0$) was too general indicating that streamlines can spiral without being a vortex. They proposed an alternate approach based on the eigenvalues of the symmetric tensor

$$T_{ij} \equiv S_{ik}S_{kj} + W_{ik}W_{kj} \tag{4.14}$$

which represents the nonlinear source term of the transport equation for S_{ij}. They define a vortex as a region with two negative eigenvalues of T_{ij}; ordering the eigenvalues such that $\lambda_1 \geq \lambda_2 \geq \lambda_3$, the definition is equivalent to requiring $\lambda_2 < 0$. The potential problem with Jeong and Hussain's definition lies in the arbitrariness of the definition of T_{ij}. A comparison of both approaches (1) $D > 0$ and (2) $\lambda_2 < 0$ is in order.

Figures 4.5 (a) to (c) respectively show iso-surface plots of D, λ_2 and streamwise vorticity ω_z. The direction of the flow is from left to right. Contours levels were adjusted to get the best possible agreement with the vorticity plot. Clearly, the two approaches give similar results when comparing with the vorticity. Most of the dominant features are captured by both methods. As Jeong and Hussain point out, when compared with the plot of D, the eigenvalue plot does leave out some information since it was designed to be more restrictive than the discriminant. Both topological approaches do not include the region of high vorticity at the wall (vortex sheet), such that all features revealed by figures 4.5 (a) and (b) are away from the wall, as desired. The vorticity plot show tube-like structure oriented with the flow, which tend to extend in the flow away from the wall. This behavior is also captured by both topological approaches.

So, both approaches seem to paint a good overall picture of the organized structures of the flow, although they both require some adjustment of the contour levels in order to get a good match. Within the adopted contour levels, the discriminant method gives marginally better results, matching the actual vorticity contours more closely, than Jeong and Hussain's method.

Wall vortex

In section 3.2.2 (see figure 3.14), a short, high intensity wall vortex was shown to produce a high speed streak as it moved downstream in the pipe. A plot of the discriminant for this feature in given in figure 4.7 (a). The discriminant reaches a maximum at the location where the vortex is known to reside (see above). Chacin and Cantwell (private communication) observed by studying the turbulent structure in boundary layer, that the discriminant tends to peak where turbulent production

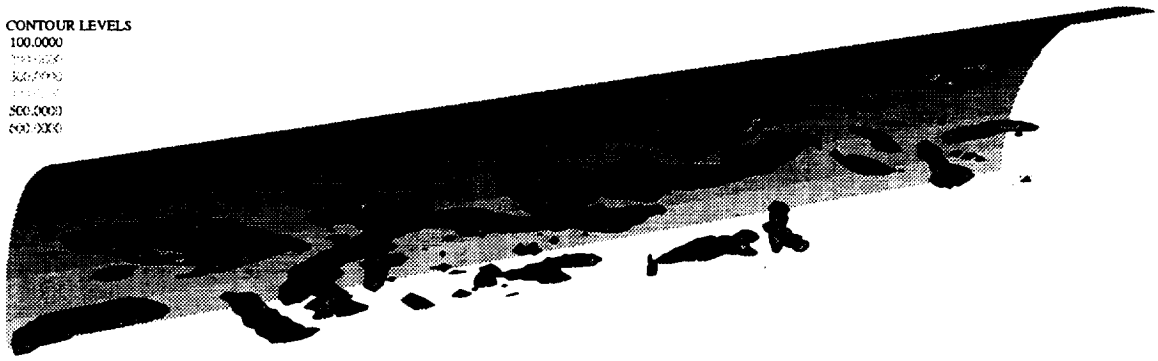

(a) Discriminant

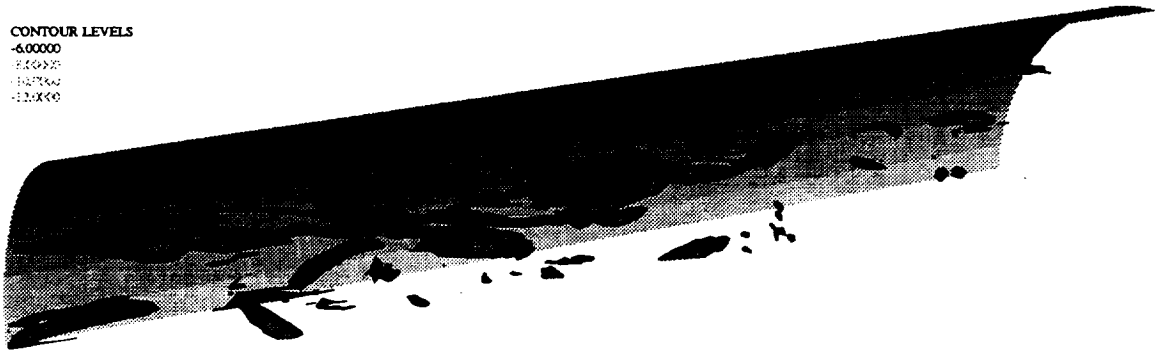

(b) λ_2

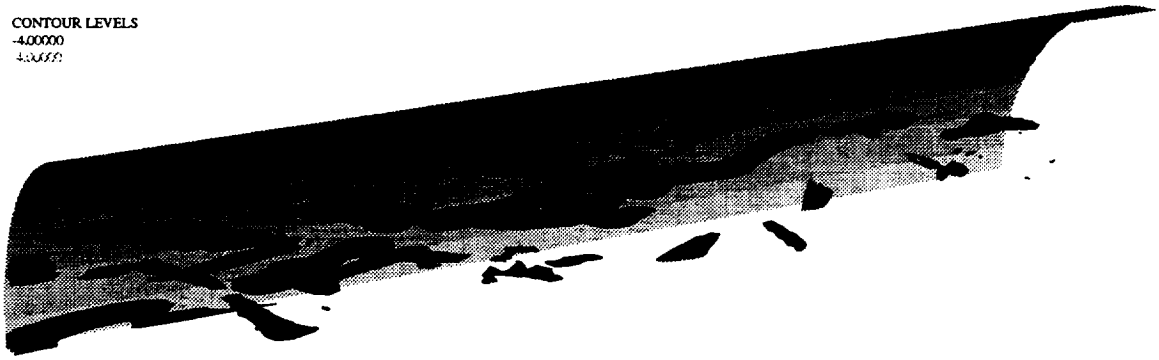

(c) ω_z

Figure 4.5: Iso-surface plots of: (a) the discriminant D, (b) the intermediate eigenvalue λ_2, and (c) the streamwise vorticity ω_z.

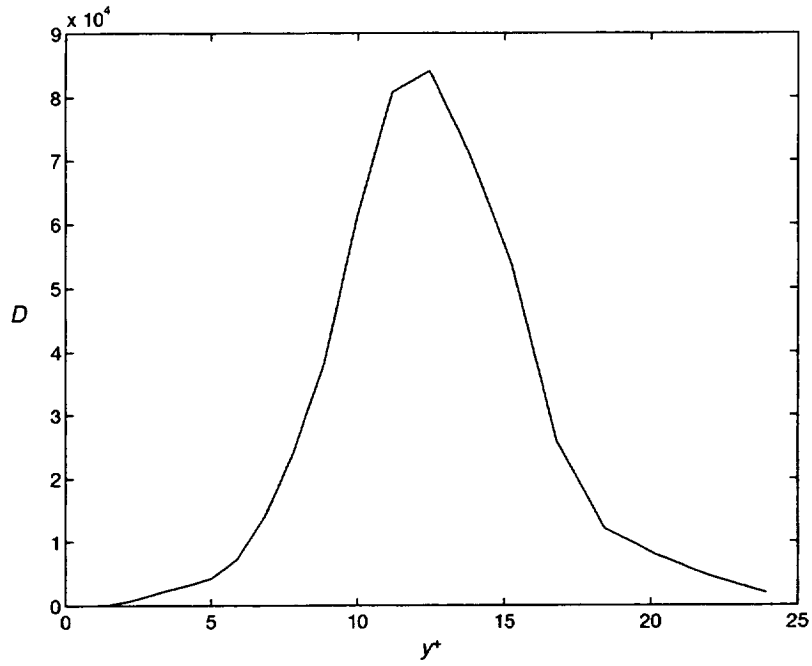

Figure 4.6: Maximum value of the discriminant versus y^+ for the region containing the wall vortex of figure 3.14.

(P_k) also reaches a maximum. Figure 4.7 (b) shows a discriminant plot for $y^+ \approx 12.5$, where turbulent production is maximum (see figure 3.27), and the overall trend of the maximum value of the discriminant is shown on figure 4.6, clearly showing the peak at $y^+ \approx 12.5$. The maximum value is taken from the region containing the wall vortex. The results are consistent with Chacin and Cantwell's observations, with a maximum discriminant an order of magnitude larger than that observed at $y^+ \approx 5$.

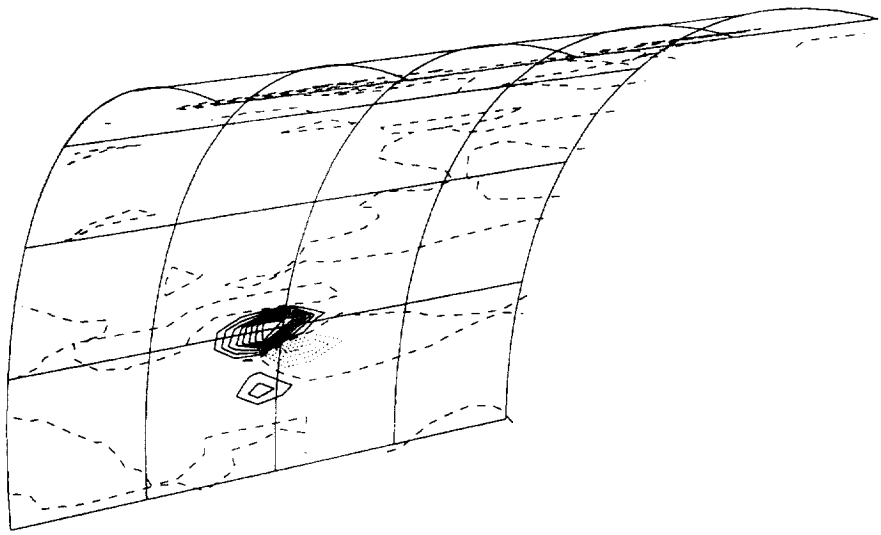

(a) $y^+ \approx 5$

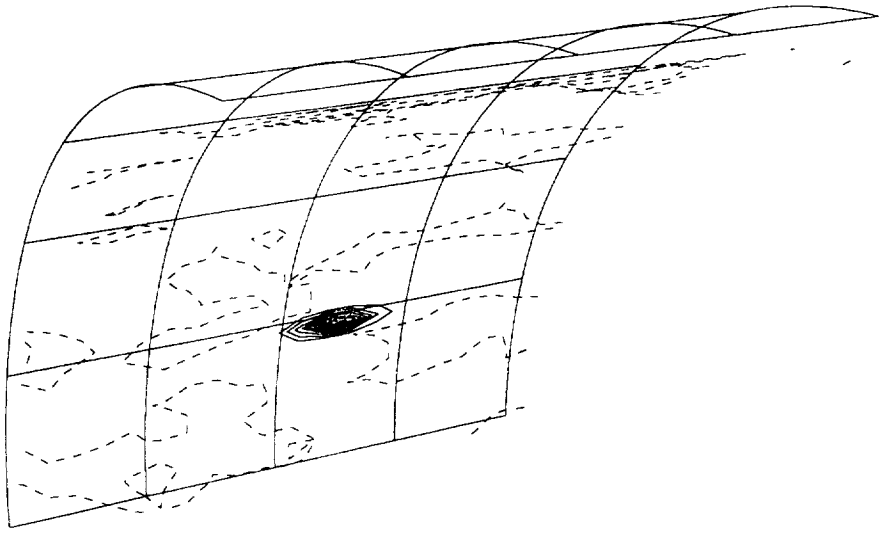

(b) $y^+ \approx 12$

Figure 4.7: Contour plots of the discriminant for the vortex shown on figure 3.14: (a) contour levels range from -2500 to 4500 by steps of 500; (b) levels range from 0 to 90000 by steps of 10000.

Chapter 5

Conclusions

This chapter concludes the present work with an overview of the development of the numerical method and the results of the pipe flow simulation. Some recommendations for future work are also made.

5.1 Numerical Method

A new numerical method for the computation of incompressible flows in cylindrical geometries was developed. The method is based on a vector Galerkin weighted residual method, using divergence-free expansion and weight vectors. With continuity satisfied *a priori* and pressure dropping out of the formulation, this approach reduces the number of unknowns from four to two, making memory management straightforward. The method makes use of b-splines polynomials to represent the radial direction and of Fourier transforms for the other two directions. This approach was found to possess spectral-like accuracy while providing a flexibility unavailable in standard spectral methods. In fact, comparing with results obtained from a finite difference simulation demonstrated the superiority of the present approach. The flexibility of the method was used to guarantee that the expansions were regular near the origin by satisfying a set of conditions. Also, a procedure was implemented to alleviate the restriction put on the time step by removing unnecessary b-splines near the origin.

5.2 Pipe Flow Simulation

A direct numerical simulation of incompressible pipe flow was successfully carried out using the method described above. The simulation was run at a Reynolds number of 5600 based on the diameter and bulk velocity, in line with several experiments and other simulations of both pipe and channel flows. The most important observation is that pipe flow and channel flow have very similar turbulent statistics. Differences between both flows are nevertheless apparent in the mean profiles with pipe flow not obeying the log-law (in this low Reynolds number range). The spectra and two-point correlations revealed that the flow was well resolved, although the pipe length is a little too short. However this does not seem to have played significantly as all results agree very well with experiments.

Turbulent intensities and higher order moments agreed generally well with experiments and other simulations. For higher order moments however, the present simulation with its high resolution and accuracy revealed some shortcomings of near wall measurements. Furthermore, it was shown that flatness levels predicted with the b-splines approach are more reliable than the ones experimentally measured or computed by finite differences; high levels of flatness in the near wall region are physical. A possible explanation for the formation of high speed streaks in the near wall region was provided by the presence of short streamwise eddies ($l_z \approx 65$ wall units) inducing positive streamwise velocity perturbations in its wake. Budgets of turbulence transport equations were again very similar to the channel's, which means that standard turbulence models should perform reasonably well in pipe flow, having proven their adequacy in channel flow. New structure tensors were computed and revealed that contrary to channel flow, the logarithmic region of pipe flow is not homogeneous (for this Reynolds number).

A topological method consisting in a classification of the second and third invariants of the velocity gradient tensor revealed that the flow (away from the wall) tends to adopt a preference for the stable focus/stretching and unstable node/saddle/saddle topologies, similar to that of free shear flows. Closer to the wall, the flow was found to have no preference. It was also shown that iso-surface plots of determinant proved

very useful in visualizing flow structures, mainly vortical eddies.

5.3 Recommendations for Future Work

Building on the present work, several avenues could be taken in the future:

- Study the time evolution of turbulent structures in pipe flow. Such work would clarify the relationship (causality) between streamwise vorticity and wall streaks, while enlarging the statistical sampling of the simulation, thus resolving some of the observed irregularities of the present simulation.

- Increase the Reynolds number of the pipe. This would provide for an interesting comparison between two different Reynolds numbers, and should be less sensitive to the present pipe length.

- Explore several classes of free shear flows, mainly jet flow. By implementing a set of free shear boundary conditions and using the pipe flow simulation as a starting point, it will be possible to study the development of a fully turbulent round jet. Free shear flows should also not be affected by the short domain size, since streamwise coherence should not by preserved in the absence of the wall.

Some work could also be performed on the computer code itself, such as improving the performance of the parallel version.

Appendix A

Few Facts About B-splines

This appendix introduces some of the basic properties of b-splines. The information provided here should be sufficient to understand most of the issues relevant to this work. For more information on the subject, the reader is invited to consult de Boor [10] (primarily) and also Shariff and Moser [41].

A.1 Background

Although similar in concept to standard finite element polynomials, b-splines offer spectral-like accuracy and are C^{S-1} continuous, where S is the order (or degree) of spline being used; this means that derivatives of velocity, such as vorticity, are smoothly and accurately represented. The higher the order, the greater the accuracy, storage requirements and computational cost. A trade-off must be reached between reasonable accuracy and fast computations. The spectral accuracy of b-splines is shown on figure A.1, where both eigenvalues of first and second order derivative operator are shown. For higher degree splines (third or fourth) over two third of the spectrum of the first order derivative operator (or modified wave number), and virtually the entire spectrum of the second order operator are reproduced accurately by the b-splines. Standard second order finite difference results are shown for reference.

By construction, a b-spline is required to have zero value and zero first $S-1$ derivatives at the edges of the intervals where it has support (see figure A.2); as such,

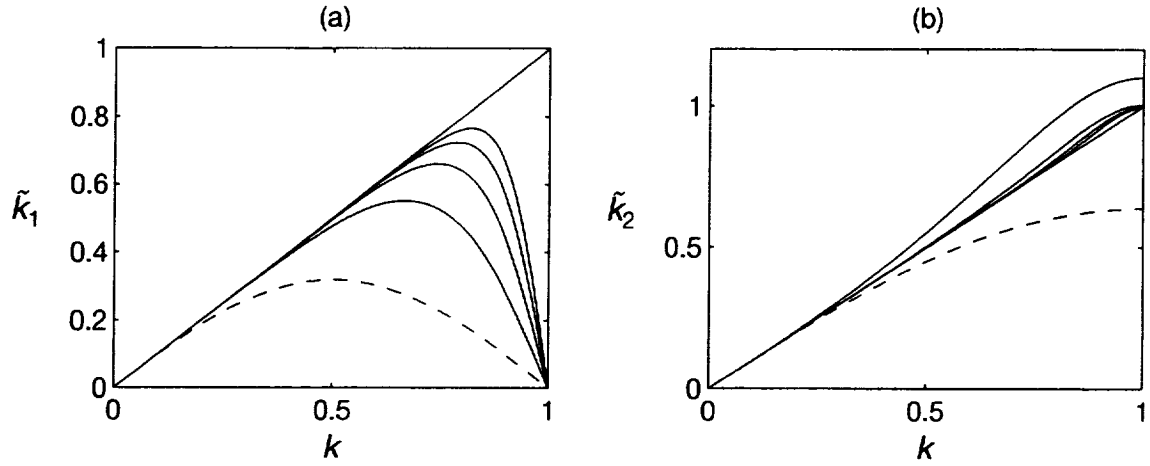

Figure A.1: Spectral accuracy of b-splines of degrees 1 through 4: (a) Modified wave number, or eigenvalue of the first order derivative operator; (b) eigenvalue of the second order derivative operator. The straight line is the exact or spectral limit and higher degree are closer to exact. The dashed line is the second order finite difference.

b-splines are the *smoothest* type of splines. As their name imply, b-splines form a basis, such that any smooth function f can be represented as a linear combination of b-splines; defining α_l to be the expansion coefficients and g_l the b-splines polynomials, we write the linear combination

$$f(r) = \sum_{l=1}^{N_r} \alpha_l g_l(r) \tag{A.1}$$

where N_r is the number of b-splines and it is implied that the b-spline basis is built such that

$$\sum_{l=1}^{N_r} g_l(r) = 1 \tag{A.2}$$

The α_l coefficients can then be determined by using an L_2 projection

$$\boldsymbol{\alpha} = \mathbf{A}^{-1}\mathbf{b} \tag{A.3}$$

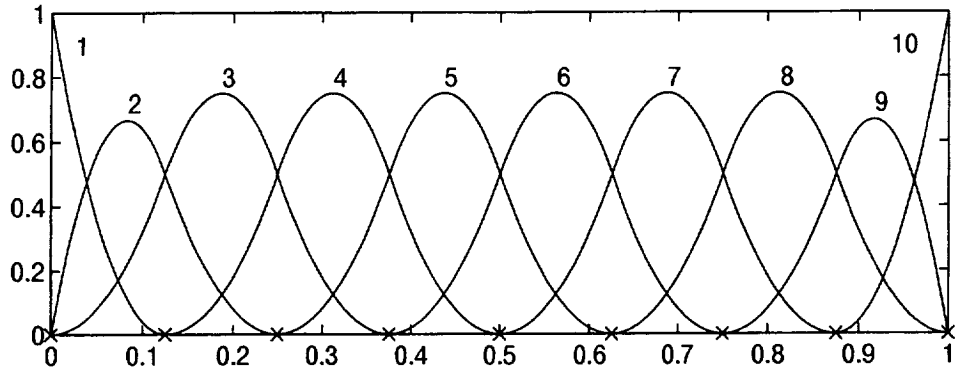

Figure A.2: Quadratic b-splines on an equispaced grid. The × symbols represent the knots which delimit the intervals over which b-splines have support.

where $\mathbf{A}$ is the $N_r \times N_r$ mass matrix

$$\mathbf{A} = \{a_{l'l}\} = \int_0^L g_{l'}(r) g_l(r)\, r\, dr \tag{A.4}$$

$$\mathbf{b} = \{b_{l'}\} = \int_0^L g_{l'}(r) f(r)\, r\, dr \tag{A.5}$$

and $\boldsymbol{\alpha} = \{\alpha_1, \alpha_2, \ldots, \alpha_{N_r}\}$.

A.2 B-splines Construction

Traditionally, splines are constructed by solving a linear set of equations. However, in the methodology established by de Boor [10], constructing b-splines is done by solving a simple recurrence relationship. First, defining

$$g_{l;0}(r) = \begin{cases} 1 & , \eta_l \leq r < \eta_{l+1} \\ 0 & , \text{otherwise} \end{cases} \tag{A.6}$$

where $g_{l;n}$ is the l^{th} b-spline of degree n and η_l is the knot coordinate. Knots are used to delimit the intervals over which b-splines have support. It should be noted that A.6 is a direct consequence of A.2. The recurrence relation becomes (see de Boor

page 131)

$$g_{l;n+1}(r) = \frac{r - \eta_l}{\eta_{l+n} - \eta_l} g_{l;n}(r) + \frac{\eta_{l+n-1} - r}{\eta_{l+n-1} - \eta_{l+1}} g_{l+1;n}(r) \tag{A.7}$$

To construct b-splines near the boundaries, de Boor introduced the concept of degenerate or multiple knots. At the boundaries fewer continuity constraints have to be met; multiple knots are used in the context of the recurrence relation A.6 and A.7 to cancel the high degree of continuity of b-splines. Figure A.3 shows the multiple knots at the boundaries; for a b-spline of degree S, there are S multiple knots at the boundaries.

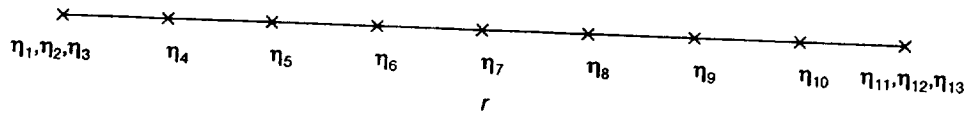

Figure A.3: Knots used in constructing the basis of figure A.2. Note the degenerate knots at the boundaries.

In order to delineate the procedure, let us construct the first two b-splines shown in figure A.2. In order to prevent divisions by zero, the first step consists in letting

$$g_{1;0} = g_{2;0} = 0 \tag{A.8}$$

$$g_{1;1} = 0 \tag{A.9}$$

The zeroth order or constant b-splines are shown in figure A.4 (a), with the numbering starting at $l = 3$ and the splines given by A.6. The first order b-splines are constructed from the zeroth order one using A.6 and A.7. They are given by

$$g_{2;1}(r) = \begin{cases} \frac{\eta_4 - r}{\eta_4 - \eta_3} & , \eta_3 \leq r < \eta_4 \\ 0 & , \text{otherwise} \end{cases} \tag{A.10}$$

$$g_{3;1}(r) = \begin{cases} \frac{r - \eta_3}{\eta_4 - \eta_3} & , \eta_3 \leq r < \eta_4 \\ \frac{\eta_5 - r}{\eta_5 - \eta_4} & , \eta_4 \leq r < \eta_5 \\ 0 & , \text{otherwise} \end{cases} \tag{A.11}$$

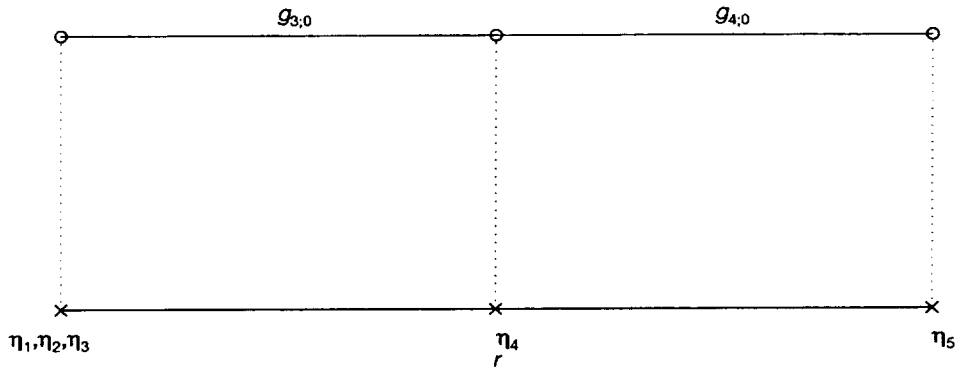

(a) Constant b-splines

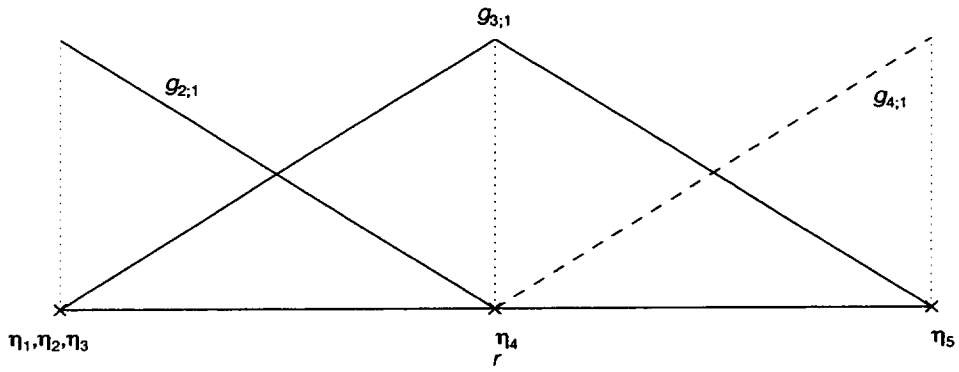

(b) Linear b-splines

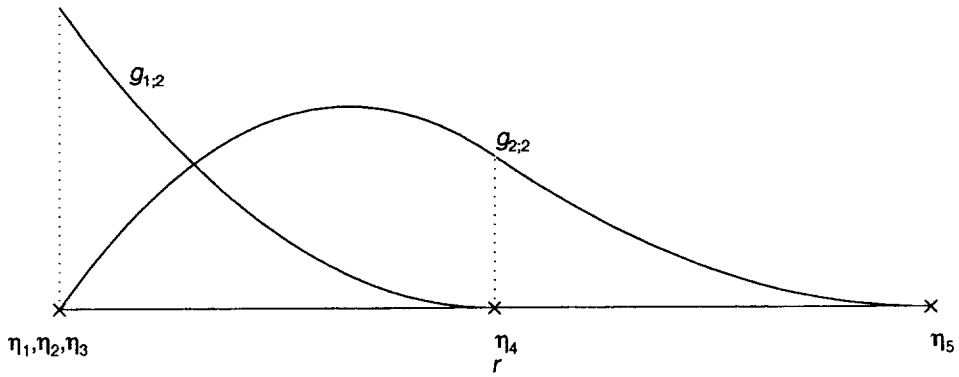

(c) Quadratic b-splines

Figure A.4: Constructing quadratic b-splines by recurrence.

Figure A.4 (b) shows the first linear b-splines. It is interesting to note that linear b-splines are identical to standard linear finite element polynomials. Lastly, the quadratic b-splines are obtained from the linear b-splines; the functions are given by:

$$g_{1;2}(r) = \begin{cases} \frac{(\eta_4 - r)^2}{(\eta_4 - \eta_3)^2} & , \eta_3 \leq r < \eta_4 \\ 0 & , \text{otherwise} \end{cases} \tag{A.12}$$

$$g_{2;2}(r) = \begin{cases} \frac{(r-\eta_3)(\eta_4 - r)}{(\eta_4 - \eta_3)^2} + \frac{(\eta_5 - r)(r - \eta_3)}{(\eta_5 - \eta_3)(\eta_4 - \eta_3)} & , \eta_3 \leq r < \eta_4 \\ \frac{(\eta_5 - r)^2}{(\eta_5 - \eta_3)(\eta_5 - \eta_4)} & , \eta_4 \leq r < \eta_5 \\ 0 & , \text{otherwise} \end{cases} \tag{A.13}$$

with the functions shown in figure A.4 (c).

A.3 Support Rules

Because b-splines have local support, the bandwidth of the mass matrix, or any other matrix which results from an inner product operation, will depend on the degree of b-splines used. Figure A.2 shows quadratic b-splines: each b-spline has support on three intervals, which are delimited by knots. For example, b-spline 6 has support on intervals shared by splines 4, 5, 7 and 8. This implies that the inner product computed in A.4 will have a bandwidth of 5. In general, a b-spline of degree S will have support on $S+1$ intervals (except near the boundaries where b-splines have support on fewer intervals since there are fewer continuity constraints to be met) translating in the inner product having a bandwidth of $2S+1$; the total number of non-degenerate (or single) knots, N_k, is then $N_k = N_r - S + 1$, where N_r is the number of b-splines.

The behavior of the b-splines near the boundaries of the domain is extremely important in understanding how to manipulate the expansion coefficients to implement the boundary conditions. A general formula for the b-spline support at $r = 0$ is given by,

$$g_l^{(q)}(0) = 0 \qquad \text{for} \quad l > q + 1 \qquad \text{and} \quad q = 0, 1, 2, \ldots, S \tag{A.14}$$

where the superscript q refers to the q^{th} derivative. Similarly, at the other boundary,

$r = 1$

$$g_l^{(q)}(1) = 0 \qquad \text{for} \quad l > N_r + q \qquad \text{and} \quad q = 0, 1, 2, \ldots, S \tag{A.15}$$

Both A.14 and A.15 can be tabulated to yield:

Table A.1: Support rule for b-splines at $r = 0$. For $r = 1$ the table is identical except that the index i in $g_i^{(q)}$ is replaced by $N_r - (i-1)$. The "x" represents non-zero values.

q	$g_1^{(q)}$	$g_2^{(q)}$	$g_3^{(q)}$	$g_4^{(q)}$	$\cdots$	$g_S^{(q)}$	$g_{S+1}^{(q)}$	$g_{S+2}^{(q)}$	$\cdots$
0	x	0	$\cdots$						
1	x	x	0	$\cdots$					
2	x	x	x	0	$\cdots$				
$\vdots$				$\ddots$					
S	x	x	x	x	$\cdots$	x	x	0	$\cdots$

Using A.2, A.14 and A.15 two important special cases can be derived; first

$$g_1(0) = g_{N_r}(1) = 1 \tag{A.16}$$

and taking the derivative of A.2 to yield $\sum_{l=1}^{N_r} g_l'(r) = 0$, we get

$$g_1(0) = -g_2(0) \tag{A.17}$$

$$g_{N_r}(1) = -g_{N_r-1}(1) \tag{A.18}$$

Appendix B

Regularity Conditions

In section 2.3.2 of chapter 2 we introduced the concept that any vector field written in cylindrical coordinates must meet a certain number of conditions in order to be regular near the origin. The purpose of this appendix is to examine in greater details how these conditions come into play when the vector expansion functions are constructed. An example is also included to delineate the whole procedure.

B.1 Regularity Conditions

Shariff (private communication) derived the regularity conditions presented in this appendix. For completeness, we include the derivation of the conditions for u_z; the conditions for the other two components can be obtained in a similar manner. Let $\mathbf{u}$ be any vector field in cylindrical coordinates:

$$u_z = \hat{u}_z(r; k_\theta, k_z) e^{i(k_\theta \theta + k_z z)} \tag{B.1}$$

$$u_r = \hat{u}_r(r; k_\theta, k_z) e^{i(k_\theta \theta + k_z z)} \tag{B.2}$$

$$u_\theta = \hat{u}_\theta(r; k_\theta, k_z) e^{i(k_\theta \theta + k_z z)} \tag{B.3}$$

Shariff's method consists in starting from a vector field in cylindrical coordinates and transforming it to cartesian coordinates by paying attention to the behavior at the

origin. Define

$$\hat{u}_z = ar^p \tag{B.4}$$

where a is a complex constant which depends on p, k_θ and k_z. In the complex plane, the transformation between cartesian and cylindrical coordinates is given by $x = r\cos\theta$ and $iy = ir\sin\theta$ such that $e^{ik_\theta\theta}$ can be rewritten as

$$e^{ik_\theta\theta} = \frac{\zeta}{r} \tag{B.5}$$

where $\zeta = x + iy$ and $r = |\zeta| = \sqrt{x^2+y^2}$. $\hat{u}_z$ becomes

$$\hat{u}_z = a\,\zeta^{k_\theta} r^{p-k_\theta} e^{ik_z z} \tag{B.6}$$

Clearly, ζ^{k_θ} is regular for $k_\theta \geq 0$ and r^{p-k_θ} is regular only for $p - k_\theta = 0, 2, 4, 6, \ldots$ since derivatives of odd powers of r can involve terms in $r^{-1/2}$ which are not regular at $r = 0$. So, we get

$$p = k_\theta + 2n \qquad \text{where} \qquad n = 0, 1, 2, \ldots \tag{B.7}$$

and the regularity condition for $\hat{u}_z$ follows

$$\hat{u}_z(r; k_\theta, k_z) = a(k_\theta, k_z)\; r^{k_\theta} P_z(r^2; k_\theta, k_z), \quad k_\theta \geq 0 \tag{B.8}$$

where $P_z(r^2; k_\theta, k_z)$ is a polynomial in r^2. Regularity conditions for the other components are given by

$$\hat{u}_r(r; k_\theta, k_z) = b(k_\theta, k_z)\; r^{k_\theta - 1} P_r(r^2; k_\theta, k_z), \quad k_\theta \geq 1 \tag{B.9}$$

$$\hat{u}_\theta(r; k_\theta, k_z) = ib(k_\theta, k_z)\; r^{k_\theta - 1} P_\theta(r^2; k_\theta, k_z), \quad k_\theta \geq 1 \tag{B.10}$$

and when $k_\theta = 0$,

$$\hat{u}_r(r; 0, k_z) = b(0, k_z)\; r P_r(r^2; 0, k_z) \tag{B.11}$$

$$\hat{u}_\theta(r; 0, k_z) = c(k_z)\; r P_\theta(r^2; 0, k_z) \tag{B.12}$$

where a, b and c are constants that can depend on the wave numbers, $P_i(r^2; k_\theta, k_z)$ are polynomials in r^2, and $P_i(0; k_\theta, k_z) = 1$. Conditions B.8 through B.12 do not account for negative azimuthal wave numbers, since these are obtained by symmetry and not by direct computations.

B.2 Regularity of the velocity vectors

After dividing the expansions into plus and minus modes, the following vectors were adopted

$$\mathbf{u}_l{}^+(r; k_\theta, k_z) = \widehat{\nabla} \times \mathbf{\Psi}_l^+(r; k_\theta, k_z) \tag{B.13}$$

$$= \widehat{\nabla} \times \begin{pmatrix} 0 \\ 0 \\ -k_z r g_l \end{pmatrix} \tag{B.14}$$

and

$$\mathbf{u}_l{}^-(r; k_\theta, k_z) = \widehat{\nabla} \times \mathbf{\Psi}_l^-(r; k_\theta, k_z) \tag{B.15}$$

$$= \widehat{\nabla} \times \begin{pmatrix} -i g_l \\ g_l \\ 0 \end{pmatrix} \tag{B.16}$$

and because the above vectors are incomplete when $k_z = 0$ *

$$\mathbf{u}_l{}^+(r; k_\theta, 0) = \widehat{\nabla} \times \mathbf{\Psi}_l^+(r; k_\theta, 0) \tag{B.17}$$

$$= \widehat{\nabla} \times \begin{pmatrix} 0 \\ 0 \\ -r g_l \end{pmatrix} \tag{B.18}$$

*Since $k_z = 0$ causes completeness problems, one might question the need for k_z to be present in B.14 in the first place. With k_z present in B.14, and later in B.21, the mass and viscous matrices are independent of the sign of k_z (they depend on some powers of ${k_z}^2$), which reduces the computations since both matrices only have to be computed for half of the k_z spectrum. It should be noted that the exact solution to the Stokes problem is also independent of the sign of k_z, a fact which must be reflected in the numerical approximation.

and $\mathbf{u}_l^-$ unchanged.

In order for the velocities $\mathbf{u}_l^+$ and $\mathbf{u}_l^-$ to be regular, the vector stream functions $\mathbf{\Psi}_l^+$ and $\mathbf{\Psi}_l^-$ must also be regular, since taking the curl will not affect regularity of the vectors either favorably or unfavorably. It is clear that the first condition which requires the radial and azimuthal components to be constrained to each other is satisfied (B.9 and B.10). The second condition which requires a certain behavior in r near the origin is generally not satisfied by the b-splines (g_l). To alleviate this, the expansion coefficients $\alpha_{jml}^{\pm}$ are constrained such that the linear combination of b-splines does have the correct behavior in r. For the vectors B.14, B.16 and B.18 this constraint can be written as

$$\sum_{l=1}^{N_r} \alpha_{jml}^{\pm} g_l(r) \sim r^{k_\theta - 1} P(r^2) \tag{B.19}$$

To ease implementation of the constraint in the computer code, special care was taken when designing the expansion vectors so the constraint would be identical for both the plus and minus modes. B.19 implies that not only the values of the splines must be constrained, but also a certain number of derivatives. If S is the order of b-splines being used, knowing that there are $S-1$ continuous derivatives at any given point, B.19 can be generalized as follows

$$\begin{aligned}
\textstyle\sum_l \alpha_{jml}^{\pm} g_l(0) &= \alpha_{jm1}^{\pm} g_1(0) = \alpha_{jm1}^{\pm} &&\sim r^{k_\theta - 1} P(r^2)\Big|_{r=0} \\
\textstyle\sum_l \alpha_{jml}^{\pm} g_l'(0) &= \alpha_{jm1}^{\pm} g_1'(0) + \alpha_{jm2}^{\pm} g_2'(0) &&\sim \tfrac{d}{dr}(r^{k_\theta - 1} P(r^2))\Big|_{r=0} \\
&\vdots &&\vdots \\
\textstyle\sum_l \alpha_{jml}^{\pm} g_l^{(S-1)}(0) &= \alpha_{jm1}^{\pm} g_1^{(S-1)}(0) + \cdots + \alpha_{jmS}^{\pm} g_S^{(S-1)}(0) &&\sim \tfrac{d^{S-1}}{dr^{S-1}}(r^{k_\theta - 1} P(r^2))\Big|_{r=0}
\end{aligned} \tag{B.20}$$

where A.14 was used to simplify the left hand side

When the right hand side of B.20 is nonzero the $\alpha_{jml}^{\pm}$ coefficients are unconstrained, otherwise the sum is set to zero. From B.20, when $k_\theta \geq S+1$, the first S coefficients are automatically zero. The constraints are implemented by modifying the necessary lines of the mass and viscous matrices in 2.18 (at most the first S lines), such that the modified mass and viscous matrices reflect the constraint in B.20.

For the cases when $k_\theta = 0$, the constraints in B.20 cannot be applied to B.14, B.16 and B.18 since they involve terms in r^{-1}. Two additional vectors must be used for this case

$$\mathbf{u}_l{}^+ = \begin{pmatrix} 0 \\ k_z g_l \\ 0 \end{pmatrix} \tag{B.21}$$

with $\mathbf{u}_l{}^-$ still unchanged. When $k_z = 0$ the vectors are again incomplete and another set of vectors is used

$$\mathbf{u}_l{}^+ = \begin{pmatrix} 0 \\ g_l \\ 0 \end{pmatrix} \quad \text{and} \quad \mathbf{u}_l{}^- = \begin{pmatrix} 0 \\ 0 \\ \frac{g_l}{r} \end{pmatrix} \tag{B.22}$$

For these last cases ($k_\theta = 0$), the expansion coefficients $\alpha^{\pm}_{0ml}$ are constrained by using $rP(r^2)$ as the right hand side in B.20 instead of $r^{k_\theta - 1}P(r^2)$. Again, the constraints are identical for both the plus and minus modes.

With the expansion vectors given in table B.1 and the constraints B.20, we observe that constraining the first $S-1$ derivatives also results in constraining the first $S-1$ derivatives of u_r and u_θ, but only the first $S-2$ derivatives of u_z, since u_z already involves a derivative of g_l. Even though u_θ also involves a derivative of g_l, it is multiplied by r, such that at the origin this term vanishes.

Mode Redundancy

A problem exists with the expansion vectors shown in table B.1 for $k_\theta > 0$: there are four coefficients which have support at the boundary, but only three velocity components. This was found to cause conditioning problems with the mass matrix rendering it singular (uninvertable). To alleviate this problem, we simply set

$$\alpha^{-}_{jmN_r} = 0 \qquad \text{for} \qquad k_\theta > 0 \tag{B.23}$$

A possible explanation for this problem comes from the presence of derivatives of b-splines in both vectors. Recall the expression for the number of knots in section A

$$N_k = N_r - S + 1 \tag{B.24}$$

Table B.1: Summary of expansion vectors and associated stream functions

	$k_\theta = 0$	$k_\theta > 0$
$k_z = 0$	$\mathbf{u}_l^+ = \begin{pmatrix} 0 \\ g_l \\ 0 \end{pmatrix}$, $\mathbf{u}_l^- = \begin{pmatrix} 0 \\ 0 \\ \frac{g_l}{r} \end{pmatrix}$ $\mathbf{\Psi}_l^+, \mathbf{\Psi}_l^-$ undetermined[a]	$\mathbf{u}_l^+ = \begin{pmatrix} -ik_\theta g_l \\ (rg_l)' \\ 0 \end{pmatrix}$, $\mathbf{u}_l^- = \begin{pmatrix} 0 \\ 0 \\ g_l' + \frac{(1-k_\theta)}{r} g_l \end{pmatrix}$ $\mathbf{\Psi}_l^+ = \begin{pmatrix} 0 \\ 0 \\ -rg_l \end{pmatrix}$, $\mathbf{\Psi}_l^- = \begin{pmatrix} -ig_l \\ g_l \\ 0 \end{pmatrix}$
$k_z \neq 0$	$\mathbf{u}_l^+ = \begin{pmatrix} 0 \\ k_z g_l \\ 0 \end{pmatrix}$, $\mathbf{u}_l^- = \begin{pmatrix} -ik_z g_l \\ k_z g_l \\ g_l' + \frac{g_l}{r} \end{pmatrix}$ $\mathbf{\Psi}_l^+ = \begin{pmatrix} -ig_l \\ 0 \\ 0 \end{pmatrix}$, $\mathbf{\Psi}_l^- = \begin{pmatrix} -ig_l \\ g_l \\ 0 \end{pmatrix}$	$\mathbf{u}_l^+ = k_z \begin{pmatrix} -ik_\theta g_l \\ (rg_l)' \\ 0 \end{pmatrix}$, $\mathbf{u}_l^- = \begin{pmatrix} -ik_z g_l \\ k_z g_l \\ g_l' + \frac{(1-k_\theta)}{r} g_l \end{pmatrix}$ $\mathbf{\Psi}_l^+ = \begin{pmatrix} 0 \\ 0 \\ -k_z r g_l \end{pmatrix}$, $\mathbf{\Psi}_l^- = \begin{pmatrix} -ig_l \\ g_l \\ 0 \end{pmatrix}$

[a]The stream functions are only known up to a constant.

Since the number of knots is constant, with derivatives of b-splines of degree S exactly representable by b-splines of degree $S-1$, in order to keep the number of knots constant, only $N_r - 1$ b-splines of degree $S-1$ are necessary, hence the extra b-spline.

B.3 Regularity of the weight vectors

Because a Galerkin method is used, the weight vectors $\mathbf{w}_{l'}$ are the complex conjugate of the velocity vectors $\mathbf{u}_l$ given in table B.1; this means that regularity of the weight vectors must also be ensured. Here again, the idea is to take a linear combination of

weight vectors, similar to B.19, such that the linear combination be regular

$$\tilde{\mathbf{w}}_{l'}^{\pm} = \sum_{n=1}^{N_r} \beta_{nl'} \mathbf{w}_n^{\pm} \tag{B.25}$$

where $\tilde{\mathbf{w}}_{l'}$ is the regular weight vector. With the weight vectors obtained from the velocity vectors, B.25 is equivalent to B.19 and B.20 such that

$$\sum_{n=1}^{N_r} \beta_{nl'} g_n(r) \sim r^{k_\theta - 1} P(r^2) \tag{B.26}$$

except when $k_\theta = 0$ where the right hand side of B.26 becomes $rP(r^2)$. By expanding B.26 as in B.20, a system of the form $\mathbf{G}\boldsymbol{\beta} = \mathbf{0}$ is obtained, where $\boldsymbol{\beta}$ is a matrix whose columns are the null vectors of $\mathbf{G}$, the matrix of constraints. Each component of the null vectors are the β coefficients in B.26. Because the null space of $\mathbf{G}$ is non unique, the following choices are made depending on the azimuthal wave number and the degree of b-splines being used (those β coefficients are computed once at the beginning of the code).

•k_θ and S **odd**:

$$\begin{pmatrix} g_1' & g_2' & 0 & 0 & 0 & \dots & 0 & 0 \\ g_1''' & g_2''' & g_3''' & g_4''' & 0 & \dots & 0 & 0 \\ \vdots & & \ddots & & & \vdots & & \\ g_1^{(p)} & g_2^{(p)} & g_3^{(p)} & g_4^{(p)} & g_5^{(p)} & \dots & g_{S-1}^{(p)} & 0 \end{pmatrix} \begin{pmatrix} 1 & 0 & & 0 \\ \beta_{11} & 0 & & 0 \\ 0 & 1 & \dots & 0 \\ \beta_{12} & \beta_{21} & & 0 \\ 0 & 0 & & 0 \\ & \vdots & & \\ \beta_{1d} & \beta_{2(d-1)} & \dots & 0 \\ 0 & 0 & & 1 \end{pmatrix} = \mathbf{0} \tag{B.27}$$

where $p = S - 2$, $d = (S-1)/2$ and all the splines are evaluated at the origin, i.e. $g_i^{(n)} \equiv \frac{d^n g_i(r)}{dr^n}\Big|_{r=0}$. With this particular form of null space, B.25 is written as

$$\tilde{\mathbf{w}}_{l'}^{\pm} = \mathbf{w}_{l'}{}^{\pm} + \sum_{\substack{n=l'+1 \\ n \text{ even}}}^{S} \beta_{(\frac{l'+1}{2})(\frac{1+n-l'}{2})} \mathbf{w}_n^{\pm} \qquad l' \leq S \text{ and } l' \text{ odd} \tag{B.28}$$

•k_θ **odd** and S **even**:

$$\begin{pmatrix} g_1' & g_2' & 0 & 0 & 0 & \dots & 0 \\ g_1''' & g_2''' & g_3''' & g_4''' & 0 & \dots & 0 \\ \vdots & & \ddots & & & \vdots & \\ g_1^{(p)} & g_2^{(p)} & g_3^{(p)} & g_4^{(p)} & g_5^{(p)} & \dots & g_S^{(p)} \end{pmatrix} \begin{pmatrix} 1 & 0 & & 0 \\ \beta_{11} & 0 & & 0 \\ 0 & 1 & \dots & 0 \\ \beta_{12} & \beta_{21} & & 0 \\ & \vdots & & \\ 0 & 0 & & 1 \\ \beta_{1d} & \beta_{2(d-1)} & \dots & \beta_{d1} \end{pmatrix} = \mathbf{0} \quad \text{(B.29)}$$

where $p = S - 1$ and $d = S/2$. In this case, $\tilde{\mathbf{w}}_{l'}^{\pm}$ is written as in B.28.

•k_θ **even** and S **odd**:

$$\begin{pmatrix} g_1 & 0 & 0 & 0 & 0 & \dots & 0 \\ g_1'' & g_2'' & g_3'' & 0 & 0 & \dots & 0 \\ \vdots & & \ddots & & & \vdots & \\ g_1^{(p)} & g_2^{(p)} & g_3^{(p)} & g_4^{(p)} & g_5^{(p)} & \dots & g_S^{(p)} \end{pmatrix} \begin{pmatrix} 0 & 0 & & 0 \\ 1 & 0 & & 0 \\ \beta_{11} & 0 & & 0 \\ 0 & 1 & \dots & 0 \\ \beta_{12} & \beta_{21} & & 0 \\ & \vdots & & \\ 0 & 0 & & 1 \\ \beta_{1d} & \beta_{2(d-1)} & \dots & \beta_{d1} \end{pmatrix} = \mathbf{0} \quad \text{(B.30)}$$

where $p = S - 1$ and $d = (S-1)/2$ and B.25 is given by

$$\tilde{\mathbf{w}}_{l'}^{\pm} = \mathbf{w}_{l'}{}^{\pm} + \sum_{\substack{n=l'+1 \\ n \text{ odd}}}^{S} \beta_{(\frac{l'}{2})(\frac{1+n-l'}{2})} \mathbf{w}_n^{\pm} \qquad l' \leq S \text{ and } l' \text{ even} \qquad \text{(B.31)}$$

•k_θ and S **even:**

$$\begin{pmatrix} g_1 & 0 & 0 & 0 & 0 & \dots & 0 & 0 \\ g_1'' & g_2'' & g_3'' & 0 & 0 & \dots & 0 & 0 \\ \vdots & & \ddots & & & \vdots & & \\ g_1^{(p)} & g_2^{(p)} & g_3^{(p)} & g_4^{(p)} & g_5^{(p)} & \dots & g_{(S-1)}^{(p)} & 0 \end{pmatrix} \begin{pmatrix} 0 & 0 & & 0 \\ 1 & 0 & & 0 \\ \beta_{11} & 0 & & 0 \\ 0 & 1 & \dots & 0 \\ \beta_{12} & \beta_{21} & & 0 \\ & \vdots & & \\ \beta_{1d} & \beta_{2(d-1)} & \dots & 0 \\ 0 & 0 & & 1 \end{pmatrix} = \mathbf{0} \tag{B.32}$$

where $p = S-2$ and $d = (S-2)/2$ and the weigth vectors

$$\tilde{\mathbf{w}}_{l'}^{\pm} = \mathbf{w}_{l'}{}^{\pm} + \sum_{\substack{n=l'+1 \\ n \text{ odd}}}^{S-2} \beta_{(\frac{l'}{2})(\frac{1+n-l'}{2})} \mathbf{w}_n^{\pm} \qquad l' \leq S-2 \text{ and } l' \text{ even} \tag{B.33}$$

So, for a given b-spline of degree S, there are two families of β coefficients: one for even and one for odd azimuthal wave numbers.

B.4 Example

The best way to illustrate how to implement the above conditions is through an example. Suppose we wish to solve for

$$\mathbf{A}\alpha = \mathbf{b} \tag{B.34}$$

Typically, this problem can arise when solving the Poisson equation for the pressure. Consider $S = 3$ (cubic b-splines) and $k_\theta = 1$; B.27 reduces to

$$\begin{pmatrix} g_1' & g_2' & 0 \end{pmatrix} \begin{pmatrix} 1 & 0 \\ \beta_{11} & 0 \\ 0 & 1 \end{pmatrix} = \mathbf{0} \tag{B.35}$$

Solving yields $\beta_{11} = -g'_1/g'_2$. Consider now the upper portion of the original system B.34; writing the matrix $\mathbf{A}$ with a bandwidth $2S+1$,

$$\begin{pmatrix} a_{11} & a_{12} & a_{13} & a_{14} & & \\ a_{21} & a_{22} & a_{23} & a_{24} & a_{25} & \\ a_{31} & a_{32} & a_{33} & a_{34} & a_{35} & a_{36} \\ & & & \ddots & & \end{pmatrix} \begin{pmatrix} \alpha_1 \\ \alpha_2 \\ \alpha_3 \\ \vdots \end{pmatrix} = \begin{pmatrix} b_1 \\ b_2 \\ b_3 \\ \vdots \end{pmatrix} \tag{B.36}$$

The first step is to make $\mathbf{w}_{l'}$ regular by taking a linear combination; using B.28

$$\begin{aligned} \tilde{\mathbf{w}}_1 &= \mathbf{w}_1 + \beta_{11}\mathbf{w}_2 \\ \tilde{\mathbf{w}}_3 &= \mathbf{w}_3 \end{aligned} \tag{B.37}$$

which means that only the first line of B.34 will be modified, since the index of the weight functions (l') corresponds to the line number of the matrices or the vectors.

$$\begin{pmatrix} \tilde{a}_{11} & \tilde{a}_{12} & \tilde{a}_{13} & \tilde{a}_{14} & \tilde{a}_{15} & \\ a_{21} & a_{22} & a_{23} & a_{24} & a_{25} & \\ a_{31} & a_{32} & a_{33} & a_{34} & a_{35} & a_{36} \\ & & & \ddots & & \end{pmatrix} \begin{pmatrix} \alpha_1 \\ \alpha_2 \\ \alpha_3 \\ \vdots \end{pmatrix} = \begin{pmatrix} \tilde{b}_1 \\ b_2 \\ b_3 \\ \vdots \end{pmatrix} \tag{B.38}$$

where following B.37, $\tilde{a}_{1j} = a_{1j} + \beta_{11}a_{2j}$ and $\tilde{b}_1 = b_1 + \beta_{11}b_2$.

The second step is to ensure regularity of the expansion functions by constraining the α_l coefficients. Using B.20 the only relevant constraint, i.e. for which the right hand side of B.20 is zero, is

$$\alpha_1 g'_1 + \alpha_2 g'_2 = 0 \tag{B.39}$$

and building that constraint into the system of equations yields

$$\begin{pmatrix} \tilde{a}_{11} & \tilde{a}_{12} & \tilde{a}_{13} & \tilde{a}_{14} & \tilde{a}_{15} & \\ g'_1 & g'_2 & 0 & 0 & 0 & \\ a_{31} & a_{32} & a_{33} & a_{34} & a_{35} & a_{36} \\ & & & \ddots & & \end{pmatrix} \begin{pmatrix} \alpha_1 \\ \alpha_2 \\ \alpha_3 \\ \vdots \end{pmatrix} = \begin{pmatrix} \tilde{b}_1 \\ 0 \\ b_3 \\ \vdots \end{pmatrix} \tag{B.40}$$

which is the system that will ensure that the expansion possesses the correct behavior

at the origin.

We conclude this section with two important comments. First, from this example it is clear that with this particular form of null space, no information was lost by imposing the regularity conditions, i.e. the expansion is still complete. Even though B.39 was imposed by removing the second line of the matrix, the information that was contained was absorbed before hand in the first line of the matrix with B.37.

Second, the conditioning of the matrix can be adversely affected by the regularity conditions. This is especially true if splines of high degree are used, since as can be seen from B.20, with higher degree splines it is possible to impose constraints of higher order. With derivatives being approximated by

$$g_p^{(q)}(0) \sim O(\Delta r^{-q}) \tag{B.41}$$

it is easy to see that when Δr is small, higher order derivatives can quickly become very large[†]. The consequence of this is to limit the highest degree of b-splines to about four or five. In order to preserve accuracy of the solution, double precision must be used throughout the computations; the standard approach on the CRAY super computer which consists in truncating variables to single precision when stored on disk must be avoided (see Moser and Moin [25]).

[†]This problem is made more difficult by the fact that even when the regularity conditions are not applied, the conditioning of the matrices is degraded when Δr is made smaller. This is a standard result in finite element analysis which is also observed here (see Strang and Fix [46], section 5.2).

Appendix C

Implementation

In this appendix, we present the full definition of the mass and viscous matrices and complete the details on how the nonlinear term is computed. Extensive use of *Mathematica*, a symbolic manipulation package, greatly reduced the effort in deriving what follows.

C.1 Mass and Viscous Matrices

The mass and viscous matrices are constructed from the following *elemental* matrices which are computed (to machine accuracy) once at the beginning of the code using Gauss quadratures. The complete mass and viscous matrices have to be reassembled at every time step, since it would require too much memory to store them. The following expressions are obtained by substituting the vector expansion functions (see table B.1) in 2.19 and 2.21; noting that $g_l \equiv g_l(r)$, the following are defined:

$$\mathbf{m}_1 = \int_0^{R2} \frac{g_l g_{l'}}{r}\, dr \qquad \mathbf{m}_2 = \int_0^{R2} g_l{}' g_{l'}{}'\, r\, dr$$

$$\mathbf{m}_3 = \int_0^{R2} g_l g_{l'}\, r\, dr \qquad \mathbf{m}_4 = \int_0^{R2} g_l{}' g_{l'}{}' r^3\, dr + R_2^2 g_l(R_2) g_{l'}(R_2)$$

$$\mathbf{m}_5 = \int_0^{R2} g_l{}' g_{l'}\, r^2\, dr \qquad \mathbf{m}_6 = \int_0^{R2} g_l g_{l'}{}' r^2\, dr$$

$$\mathbf{m}_7 = \int_0^{R2} \frac{g_l g_{l'}}{r^3}\, dr - g_l'(0) g_{l'}'(0) \qquad \mathbf{m}_8 = \int_0^{R2} \frac{g_l' g_{l'}'}{r}\, dr$$

$$\mathbf{m}_9 = \int_0^{R2} g_l'' g_{l'}''\, r\, dr - R_2 g_l''(R_2) g_{l'}'(R_2) \qquad \mathbf{m}_{10} = \int_0^{R2} g_l'' g_{l'}''\, r^3\, dr - (R_2^3 g_l''(R_2) g_{l'}'(R_2) + R_2^2 g_l''(R_2) g_{l'}(R_2))$$

$$\mathbf{m}_{11} = \int_0^{R2} g_l' g_{l'}\, dr \qquad \mathbf{m}_{12} = \int_0^{R2} g_l g_{l'}'\, dr$$

$$\mathbf{m}_{13} = \int_0^{R2} g_l'' g_{l'}'\, r^2\, dr - R_2^2 g_l''(R_2) g_{l'}(R_2) \qquad \mathbf{m}_{14} = \int_0^{R2} g_l' g_{l'}''\, r^2\, dr - R_2^2 g_l'(R_2) g_{l'}'(R_2)$$

furthermore, the following boundary terms are also defined (matrices which only have non-zero elements on the last line, i.e. $l' = N_r$, by virtue of A.14)

$$\mathbf{bt}_1 = g_l(R_2) g_{l'}(R_2), \qquad \mathbf{bt}_2 = R_2 g_l'(R_2) g_{l'}(R_2), \qquad \mathbf{bt}_3 = \frac{g_l(R_2) g_{l'}(R_2)}{R_2^2}$$

$$\mathbf{bt}_4 = \frac{g_l'(R_2) g_{l'}(R_2)}{R_2} + g_l''(R_2) g_{l'}(R_2), \qquad \mathbf{bt}_5 = \frac{g_l'(R_2) g_{l'}(R_2)}{R_2} - \frac{g_l(R_2) g_{l'}(R_2)}{R_2^2}$$

Note that the boundary term in $\mathbf{m}_7$ was obtained by applying L'Hôpital rule to boundary terms containing a $1/r^n$ factor. Other boundary terms at $r = 0$ cancel either because they are absorbed by the imposition of the regularity conditions, or contain an r^n factor.

C.1.1 Mass Matrices

The mass matrix is assembled from the following matrices (see 2.24 and 2.25).

• $k_z \neq 0$, $k_\theta \neq 0$:

$$\mathbf{A}_+^+ = \{a_{+l'l}^+\} = {k_z}^2 \left[({k_\theta}^2 - 1)\mathbf{m}_3 + \mathbf{m}_4 \right]$$

$$\mathbf{A}_-^- = \{a_{-l'l}^-\} = \left[2{k_z}^2 \mathbf{m}_3 + (k_\theta - 1)^2 \mathbf{m}_1 + \mathbf{m}_2 + (1 - k_\theta)\mathbf{bt}_1 \right]$$

$$\mathbf{A}_-^+ = \{a_{-l'l}^+\} = {k_z}^2 \left[(k_\theta + 1)\mathbf{m}_3 + \mathbf{m}_5 \right]$$

$$\mathbf{A}_{+}^{-} = \{a_{+l'l}^{-}\} = {k_z}^2\Big[(k_\theta + 1)\mathbf{m}_3 + \mathbf{m}_6\Big]$$

- $k_z = 0,\ k_\theta \neq 0$:

$$\mathbf{A}_{+}^{+} = \Big[({k_\theta}^2 - 1)\mathbf{m}_3 + \mathbf{m}_4\Big]$$

$$\mathbf{A}_{-}^{-} = \Big[(k_\theta - 1)^2\mathbf{m}_1 + \mathbf{m}_2 + (1 - k_\theta)\mathbf{bt}_1\Big]$$

$$\mathbf{A}_{-}^{+} = \mathbf{A}_{+}^{-} = \mathbf{0}$$

- $k_z \neq 0,\ k_\theta = 0$:

$$\mathbf{A}_{+}^{+} = \mathbf{A}_{-}^{+} = \mathbf{A}_{+}^{-} = {k_z}^2\mathbf{m}_3$$

$$\mathbf{A}_{-}^{-} = \Big[2{k_z}^2\mathbf{m}_3 + \mathbf{m}_1 + \mathbf{m}_2 + \mathbf{bt}_1\Big]$$

- $k_z = 0,\ k_\theta = 0$:

$$\mathbf{A}_{+}^{+} = \mathbf{m}_3$$

$$\mathbf{A}_{-}^{-} = \mathbf{m}_1$$

$$\mathbf{A}_{-}^{+} = \mathbf{A}_{+}^{-} = \mathbf{0}$$

In order to minimize storage, the mass matrix is stored in banded form, following the structure shown on figure C.1. Each element of the matrix takes its value from the four sub-matrices defined above. The elements denoted by an "X" appear after the imposition of the regularity conditions. As seen in the example of section B.4, imposing those conditions will locally increase the bandwidth of the matrix. Because of this unusual feature, special banded matrix solver and matrix-vector multiply routines were written to account for these extra terms. With the mass and viscous matrices constructed in such a way, the $\boldsymbol{\alpha}$ and $\mathbf{f}_{\mathbf{nl}}$ vectors in 2.18 have to be ordered with the + and − modes alternating, i.e. $\boldsymbol{\alpha} = \{\alpha_1^+, \alpha_1^-, \alpha_2^+, \ldots\}$.

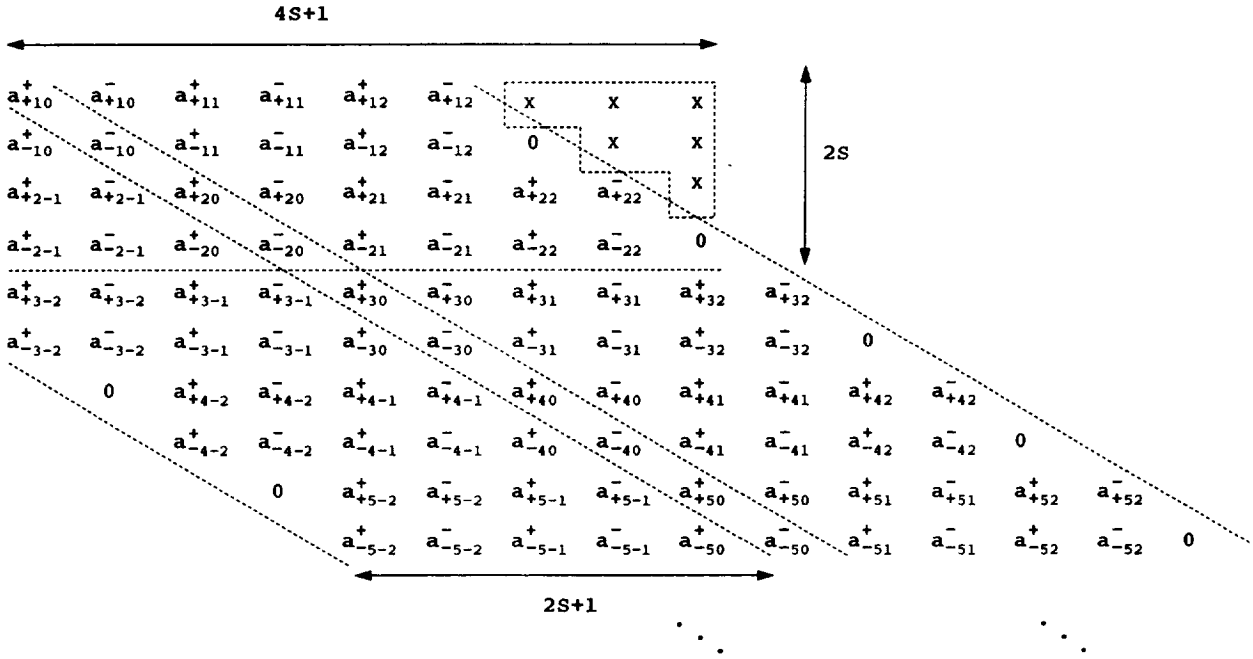

Figure C.1: Mass matrix as defined in 2.18. It is assumed that a second degree spline has been used, but the dimensions are shown for a spline of degree S.

C.1.2 Viscous Matrices

In a similar way to the mass matrix, the viscous matrix is assembled from the following:

• $k_z \neq 0$, $k_\theta \neq 0$:

$$\begin{aligned}
\mathbf{B}_+^+ &= -\frac{{k_z}^2}{Re}\Big[{k_z}^2((k_\theta{}^2-1)\mathbf{m}_3+\mathbf{m}_4)+(k_\theta{}^2-1)^2\mathbf{m}_1+(2k_\theta{}^2+1)\mathbf{m}_2+\mathbf{m}_{10}+\\
&\qquad (1-k_\theta{}^2)\mathbf{bt}_1-(2+k_\theta{}^2)\mathbf{bt}_2\Big]\\
\mathbf{B}_-^- &= -\frac{1}{Re}\Big[2{k_z}^4\mathbf{m}_3+(-3+4k_\theta+2k_\theta{}^2-4k_\theta{}^3+k_\theta{}^4)\mathbf{m}_7+\\
&\qquad 3{k_z}^2((k_\theta-1)^2\mathbf{m}_1+\mathbf{m}_2)+(3-4k_\theta+2k_\theta{}^2)\mathbf{m}_8+\mathbf{m}_9+\\
&\qquad {k_z}^2((1-k_\theta)\mathbf{bt}_1-2\mathbf{bt}_2)+(-2+3k_\theta-k_\theta{}^3)\mathbf{bt}_3+\\
&\qquad (k_\theta-1)(\mathbf{bt}4-(k_\theta-1)\mathbf{bt}_5)\Big]
\end{aligned}$$

$$\mathbf{B}_{-}^{+} = -\frac{{k_z}^2}{Re}\Big[{k_z}^2((k_\theta+1)\mathbf{m}_3+\mathbf{m}_5)+(k_\theta-1)^2((k_\theta+1)\mathbf{m}_1+\mathbf{m}_{11})+ (k_\theta+2)\mathbf{m}_2+\mathbf{m}_{13}-(2+k_\theta)\mathbf{bt}_2\Big]$$

$$\mathbf{B}_{+}^{-} = -\frac{{k_z}^2}{Re}\Big[{k_z}^2((k_\theta+1)\mathbf{m}_3+\mathbf{m}_6)+(k_\theta-1)^2((k_\theta+1)\mathbf{m}_1+\mathbf{m}_{12})+ (k_\theta+2)\mathbf{m}_2+\mathbf{m}_{14}-(1+k_\theta)\mathbf{bt}_2\Big]$$

• $k_z = 0$, $k_\theta \neq 0$:

$$\mathbf{B}_{+}^{+} = -\frac{1}{Re}\Big[({k_\theta}^2-1)^2\mathbf{m}_1+(2{k_\theta}^2+1)\mathbf{m}_2+\mathbf{m}_{10}+(1-{k_\theta}^2)\mathbf{bt}_1-(2+{k_\theta}^2)\mathbf{bt}_2\Big]$$

$$\mathbf{B}_{-}^{-} = -\frac{1}{Re}\Big[(-3+4k_\theta+2{k_\theta}^2-4{k_\theta}^3+{k_\theta}^4)\mathbf{m}_7+(3-4k_\theta+2{k_\theta}^2)\mathbf{m}_8+\mathbf{m}_9+ (-2+3k_\theta-{k_\theta}^3)\mathbf{bt}_3+(k_\theta-1)(\mathbf{bt}_4-(k_\theta-1)\mathbf{bt}_5)\Big]$$

$$\mathbf{B}_{-}^{+} = \mathbf{B}_{+}^{-} = \mathbf{0}$$

• $k_z \neq 0$, $k_\theta = 0$:

$$\mathbf{B}_{+}^{+} = \mathbf{B}_{-}^{+} = \mathbf{B}_{+}^{-} = -\frac{{k_z}^2}{Re}\Big[{k_z}^2\mathbf{m}_3+\mathbf{m}_1+\mathbf{m}_2-\mathbf{bt}_2\Big]$$

$$\mathbf{B}_{-}^{-} = -\frac{1}{Re}\Big[2{k_z}^4\mathbf{m}_3-3(\mathbf{m}_7-\mathbf{m}_8)+3{k_z}^2(\mathbf{m}_1+\mathbf{m}_2)+\mathbf{m}_9+ {k_z}^2(\mathbf{bt}_1-2\mathbf{bt}_2)-2\mathbf{bt}_3-\mathbf{bt}_4-\mathbf{bt}_5\Big]$$

• $k_z = 0$, $k_\theta = 0$:

$$\mathbf{B}_{+}^{+} = -\frac{1}{Re}\Big[\mathbf{m}_1+\mathbf{m}_2-\mathbf{bt}_2\Big]$$

$$\mathbf{B}_{-}^{-} = -\frac{1}{Re}\Big[\mathbf{m}_8-\mathbf{m}_7-\mathbf{bt}_5-\mathbf{bt}_3\Big]$$

$$\mathbf{B}_{-}^{+} = \mathbf{B}_{+}^{-} = \mathbf{0}$$

C.2 Nonlinear Term

Computing the nonlinear term is by far the most computationally intensive operation of the code; typically it requires over 85% of the computing time. This is due mostly to the radial direction which is a "slow" direction (requiring N_r^2 operations), whereas the azimuthal and streamwise directions are "fast".

The first step is to compute the vorticity and velocity components. Using the vectors in table B.1,

$$\omega_r(r,\theta,z,t) = A_l\, g_l(r) + B_l\, r g_l'(r) + C_l\, \frac{g_l(r)}{r^2} + D_l\, \frac{g_l'(r)}{r} \tag{C.1}$$

$$\omega_\theta(r,\theta,z,t) = E_l\, g_l(r) + F_l \left(\frac{g_l'(r)}{r} - \frac{g_l(r)}{r^2} \right) + G_l\, g_l''(r) \tag{C.2}$$

$$\omega_z(r,\theta,z,t) = H_l\, \frac{g_l(r)}{r} + (I_l + 2J_l)\, g_l'(r) + J_l\, r g_l''(r) \tag{C.3}$$

$$v_r(r,\theta,z,t) = K_l\, g_l(r) \tag{C.4}$$

$$v_\theta(r,\theta,z,t) = J_l\, r g_l'(r) + I_l\, g_l(r) \tag{C.5}$$

$$v_z(r,\theta,z,t) = -G_l\, g_l'(r) - F_l\, \frac{g_l(r)}{r} \tag{C.6}$$

where, the summation convention was used for repeated indices ($a_l b_l = \sum_l^{N_r} a_l b_l$), and the following were defined

$$A_l(\theta,z,t) = \sum_{k_\theta} \sum_{k_z} -i {k_z}^2 (\alpha_l^+ + \alpha_l^-)\, e^{i(k_\theta \theta + k_z z)}$$

dropping the summation signs and the exponential

$$B_l(\theta,z,t) = \begin{cases} -i {k_z}^2 \alpha_l^+ \\ 0 \qquad\qquad , k_\theta = 0 \end{cases}$$

$$C_l(\theta,z,t) = -i k_\theta (k_\theta - 1) \alpha_l^-$$

$$D_l(\theta,z,t) = i k_\theta \alpha_l^-$$

$$E_l(\theta,z,t) = {k_z}^2 (k_\theta \alpha_l^+ + \alpha_l^-)$$

$$
\begin{aligned}
F_l(\theta,z,t) &= (k_\theta - 1)\alpha_l^- \\
G_l(\theta,z,t) &= \begin{cases} -\alpha_l^- \\ 0 \qquad , k_\theta = k_z = 0 \end{cases} \\
H_l(\theta,z,t) &= \begin{cases} k_z(1-k_\theta)((1+k_\theta)\alpha_l^+ + \alpha_l^-) \\ (1-{k_\theta}^2)\alpha_l^+ \qquad\qquad\qquad , k_z = 0 \end{cases} \\
I_l(\theta,z,t) &= \begin{cases} k_z(\alpha_l^+ + \alpha_l^-) \\ \alpha_l^+ \qquad\qquad , k_z = 0 \end{cases} \\
J_l(\theta,z,t) &= \begin{cases} k_z\alpha_l^+ \quad , kz \neq 0 \text{ and } k_\theta \neq 0 \\ \alpha_l^+ \quad , k_z = 0 \text{ and } k_\theta \neq 0 \\ 0 \quad , k_\theta = 0 \end{cases} \\
K_l(\theta,z,t) &= \begin{cases} -ik_z(k_\theta\alpha_l^+ + \alpha_l^-) \\ -ik_\theta\alpha_l^+ \qquad\qquad , k_z = 0 \text{ and } k_\theta \neq 0 \\ 0 \qquad\qquad\qquad , k_z = k_\theta = 0 \end{cases}
\end{aligned}
$$

Once all those terms have been computed, they are transformed to physical space where the second step consists in computing the product $\mathbf{w}_{l''}{}^{\pm} \cdot (\mathbf{v} \times \boldsymbol{\omega})$. Defining the following three-dimensional (nonlinear) matrices

$$
\begin{aligned}
\mathbf{f}_1 &= \int_0^{R2} g_{l''} g_l g_m dr \qquad \mathbf{f}_2 = \int_0^{R2} g_{l''} g_l{}' g_m dr \qquad \mathbf{f}_3 = \int_0^{R2} g_{l''}{}' g_l g_m dr \\
\mathbf{f}_4 &= \int_0^{R2} g_{l''}{}' g_l{}' g_m dr \qquad \mathbf{f}_5 = \int_0^{R2} g_{l''} g_l g_m{}' dr \qquad \mathbf{f}_6 = \int_0^{R2} g_{l''} g_l{}' g_m{}' dr \\
\mathbf{f}_7 &= \int_0^{R2} g_{l''}{}' g_l g_m{}' dr \qquad \mathbf{f}_8 = \int_0^{R2} g_{l''}{}' g_l{}' g_m{}' dr \qquad \mathbf{f}_9 = \int_0^{R2} g_{l''} g_l g_m{}'' dr \\
\mathbf{f}_{10} &= \int_0^{R2} g_{l''} g_l{}' g_m{}'' dr \qquad \mathbf{f}_{11} = \int_0^{R2} g_{l''}{}' g_l g_m{}'' dr
\end{aligned}
$$

then, we also define:

$$
\begin{aligned}
\gamma_{l''}^+ &= (E_m F_l + H_m I_l)\,\mathbf{f}_1 + (E_m G_l + H_m J_l)\,r\mathbf{f}_2 + \\
&\quad (I_m + 2J_m)\,(I_l\, r\mathbf{f}_5 + J_l\, r^2\mathbf{f}_6) + F_m \left(F_l \left(\frac{\mathbf{f}_5}{r} - \frac{\mathbf{f}_1}{r^2} \right) + G_l \left(\mathbf{f}_6 - \frac{\mathbf{f}_2}{r} \right) \right) +
\end{aligned}
$$

$$G_m(F_l\,\mathbf{f}_9 + G_l\,r\mathbf{f}_{10}) + J_m(I_l\,r^2\mathbf{f}_9 + J_l\,r^3\mathbf{f}_{10})$$

$$\begin{aligned}\beta^-_{l'} &= (A_m I_l - E_m K_l)\,\mathbf{f}_1 + (C_m I_l + F_m K_l)\,\frac{\mathbf{f}_1}{r^2} + A_m J_l\,r\mathbf{f}_2 + C_m J_l\,\frac{\mathbf{f}_2}{r} + \\ &\quad D_m J_l\,\mathbf{f}_6 - G_m K_l\,\mathbf{f}_9 + B_m(I_l\,r\mathbf{f}_5 + J_l\,r^2\mathbf{f}_6) + (D_m I_l - F_m K_l)\,\frac{\mathbf{f}_5}{r}\end{aligned}$$

$$\begin{aligned}\Upsilon^-_{l'} &= (A_m F_l + H_m K_l)\,\mathbf{f}_1 + A_m G_l r\,\mathbf{f}_2 + C_m\left(F_l\,\frac{\mathbf{f}_1}{r^2} + G_l\,\frac{\mathbf{f}_2}{r}\right) + B_m G_l\,r^2\mathbf{f}_6 + \\ &\quad (B_m F_l + I_m K_l + 2J_m K_l)\,r\mathbf{f}_5 + D_m\left(F_l\,\frac{\mathbf{f}_5}{r} + G_l\,\mathbf{f}_6\right) + J_m K_l\,r^2\mathbf{f}_9\end{aligned}$$

$$\begin{aligned}\tilde{\Upsilon}_{l'} &= (A_m F_l + H_m K_l)\,r\mathbf{f}_3 + A_m G_l r^2\,\mathbf{f}_4 + C_m\left(F_l\,\frac{\mathbf{f}_3}{r} + G_l\,\mathbf{f}_4\right) + B_m G_l\,r^3\mathbf{f}_8 + \\ &\quad (B_m F_l + I_m K_l + 2J_m K_l)\,r^2\mathbf{f}_7 + D_m\,(F_l\,\mathbf{f}_7 + G_l\,r\mathbf{f}_8) + J_m K_l\,r^3\mathbf{f}_{11}\end{aligned}$$

$$\begin{aligned}\tilde{\delta}_{l'} &= (A_m I_l - E_m K_l)\,r\mathbf{f}_3 + (C_m I_l + F_m K_l)\,\frac{\mathbf{f}_3}{r} + C_m J_l\,\mathbf{f}_4 + A_m J_l\,r^2\mathbf{f}_4 + \\ &\quad (D_m I_l - F_m K_l)\,\mathbf{f}_7 + B_m\,(I_l\,r^2\mathbf{f}_7 + J_l\,r^3\mathbf{f}_8) + D_m J_l\,r\mathbf{f}_8 - G_m K_l\,r\mathbf{f}_{11}\end{aligned}$$

where all the products $\mathbf{f}_i\,r^n$ are done under the integral sign, and the m and l indices have been summed; for example

$$B_m G_l\,r^2\mathbf{f}_6 \equiv \sum_m^{N_r}\sum_l^{N_r} B_m G_l \int_0^{R2} g_{l'}\,g_l{}'\,g_m{}'\,r^2\,dr \tag{C.7}$$

This means there are in fact twenty four different integrals, which are also precomputed at the beginning of the code (some of them can be simply obtained by symmetry). Once $\gamma^+_{l'}$, $\beta^-_{l'}$, $\Upsilon^-_{l'}$, $\tilde{\Upsilon}_{l'}$ and $\tilde{\delta}_{l'}$ are computed, they are transformed to Fourier space ($\gamma^+_{l'} \equiv \gamma^+_{l'}(k_\theta, k_z)$, ...) where the final answer is obtained:

$$\begin{aligned}f^+_{\mathrm{n}l'} &= \frac{1}{2\pi L_z}\int_0^{L_z}\int_0^{2\pi}\int_0^{R_2} \mathbf{w}_{l'}{}^+ \cdot (\mathbf{v}\times\boldsymbol{\omega})\,e^{-i(k_\theta{}'\theta + k_z{}'z)}\,r\,dr\,d\theta\,dz \\ &= I^+(ik_\theta\gamma^+_{l'} - \Upsilon^-_{l'}) - J^+\tilde{\Upsilon}_{l'}\end{aligned} \tag{C.8}$$

$$f^-_{\mathrm{n}l'} = \frac{1}{2\pi L_z}\int_0^{L_z}\int_0^{2\pi}\int_0^{R_2} \mathbf{w}_{l'}{}^- \cdot (\mathbf{v}\times\boldsymbol{\omega})\,e^{-i(k_\theta{}'\theta + k_z{}'z)}\,r\,dr\,d\theta\,dz$$

$$= I^-(i\gamma_{l'}^+ - \Upsilon_{l'}^-) + F^-\beta_{l'}^- - G^-\tilde{\delta}_{l'} \tag{C.9}$$

where

$$I^+ = \begin{cases} k_z \\ 1 \quad , k_z = 0 \end{cases} , \qquad J^+ = \begin{cases} k_z \\ 1 \quad , k_z = 0 \text{ and } k_\theta \neq 0 \\ 0 \quad , k_\theta = 0 \end{cases}$$

$$I^- = k_z \, , \qquad F^- = k_\theta - 1 \, , \qquad G^- = \begin{cases} 1 \\ 0 \quad , k_\theta = k_z = 0 \end{cases}$$

C.3 FFT's and Modal Reduction

In section 2.3.4, the concept of modal reduction was introduced to alleviate the concentration of modes near the origin. Implementing this procedure in the context of the computation of the nonlinear term requires special attention. Consider figure C.2, which consists of an equispaced grid with 18 b-splines.

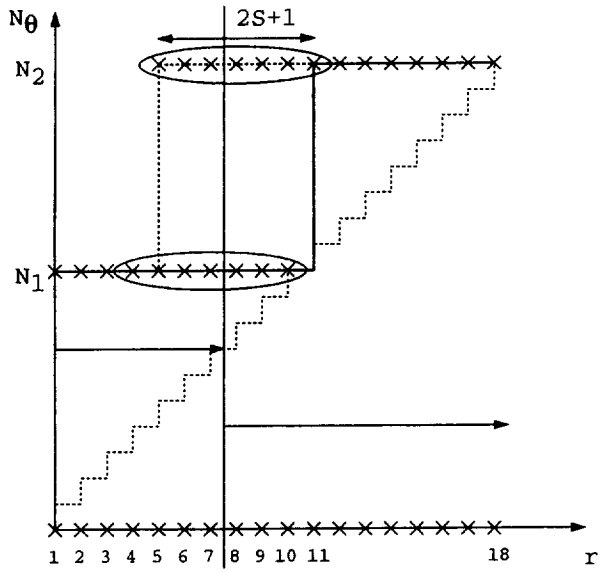

Figure C.2: Modal reduction and Fourier transform size; the ordinate represents the number of Fourier modes.

Azimuthal modes which fall below the staircase shaped dotted line represent the

only non-zero modes. Computing the product C.7 requires all the terms to be transformed on a physical grid with an equal number of points. It is clear that transforming all 18 modes on a grid containing N_2 points, would result in a large waste of computations, since roughly half the values to be transformed are zero. To reduce the length of the FFT's, radial positions are defined where the lengths of the transforms are cutoff: for example, in figure C.2 the radial position equivalent to spline 11 is the cutoff value. Any mode lower than 11 would be computed on a grid of N_1, and from 11 onward, on a grid of N_2.

Even though this approach is simple in principle, special care must be taken when approaching the overlapping region near the cutoff position. As seen in section A all integrals of the form shown in C.7 have support on $2S+1$ intervals, which means that computing the nonlinear term for $l' = 8$ requires information from $5 \leq l' \leq 11$. This can be a problem since modes 5–10 lie on a different grid than 11. The trick is then to FFT modes 5–10 to Fourier space with N_1 modes and back to physical space again but on a grid of size N_2. Only when this is done can modes 8 and up be computed. For $l' \leq 7$, all the computations are performed on a grid of N_1.

In practice, the code allows for up to six different cutoff levels; more than six shows no significant gain due to the extra work required by the remapping near the overlapping regions.

C.4 Time Advance

When the time advance method given in 2.30–2.32 is applied to 2.18, it becomes

$$\widetilde{\mathbf{A}}_1\boldsymbol{\alpha}' = \tilde{\mathbf{B}}_1\boldsymbol{\alpha}_n + \Delta t\gamma_1\mathbf{f}_{\rm nl}(\boldsymbol{\alpha}_n) \tag{C.10}$$

$$\widetilde{\mathbf{A}}_2\boldsymbol{\alpha}'' = \tilde{\mathbf{B}}_2\boldsymbol{\alpha}' + \Delta t\left[\gamma_2\mathbf{f}_{\rm nl}(\boldsymbol{\alpha}') + \zeta_1\mathbf{f}_{\rm nl}(\boldsymbol{\alpha}_n)\right] \tag{C.11}$$

$$\widetilde{\mathbf{A}}_3\boldsymbol{\alpha}_{n+1} = \tilde{\mathbf{B}}_3\boldsymbol{\alpha}'' + \Delta t\left[\gamma_3\mathbf{f}_{\rm nl}(\boldsymbol{\alpha}'') + \zeta_2\mathbf{f}_{\rm nl}(\boldsymbol{\alpha}')\right] \tag{C.12}$$

where $\widetilde{\mathbf{A}}_i$ and $\tilde{\mathbf{B}}_i$ are respectively the effective mass and viscous matrices defined as

$$\widetilde{\mathbf{A}}_i = \mathbf{A} - \beta_i\Delta t\mathbf{B} \qquad \text{and} \qquad \tilde{\mathbf{B}}_i = \mathbf{A} + \alpha_i\Delta t\mathbf{B} \tag{C.13}$$

To minimize storage, the above method is implemented in the following way: defining $\boldsymbol{\alpha}_{\text{old}}$ and $\boldsymbol{\alpha}_{\text{act}}$ to be two storage variables the following algorithm is implemented

- From the previous time step, set $\boldsymbol{\alpha}_{\text{act}} = \boldsymbol{\alpha}_{\text{old}} = \boldsymbol{\alpha}_n$.
- First RK sub–step:
  1. Compute the new Δt
  2. $\boldsymbol{\alpha}_{\text{act}} = \mathbf{f}_{\text{nl}}(\boldsymbol{\alpha}_{\text{act}})$
  3. $\boldsymbol{\alpha}_{\text{old}} = \tilde{\mathbf{B}}_1 \boldsymbol{\alpha}_{\text{old}}$
  4. $\boldsymbol{\alpha}_{\text{act}} = \boldsymbol{\alpha}_{\text{old}} + \gamma_1 \Delta t \boldsymbol{\alpha}_{\text{act}}$
  5. $\boldsymbol{\alpha}_{\text{old}} = \frac{\boldsymbol{\alpha}_{\text{act}} - \boldsymbol{\alpha}_{\text{old}}}{\gamma_1 \Delta t} \quad (= \mathbf{f}_{\text{nl}}(\boldsymbol{\alpha}_n))$
  6. Enforce the boundary conditions (BC) on $\boldsymbol{\alpha}_{\text{act}}$
  7. $\boldsymbol{\alpha}_{\text{act}} = \widetilde{\mathbf{A}}_1^{-1} \boldsymbol{\alpha}_{\text{act}}$
  8. $\boldsymbol{\alpha}_{\text{old}} = \tilde{\mathbf{B}}_2 \boldsymbol{\alpha}_{\text{act}} + \zeta_1 \Delta t \boldsymbol{\alpha}_{\text{old}}$
  9. Enforce BC on $\boldsymbol{\alpha}_{\text{old}}$
- Second RK sub–step:
  1. $\boldsymbol{\alpha}_{\text{act}} = \mathbf{f}_{\text{nl}}(\boldsymbol{\alpha}_{\text{act}})$
  2. $\boldsymbol{\alpha}_{\text{act}} = \boldsymbol{\alpha}_{\text{old}} + \gamma_2 \Delta t \boldsymbol{\alpha}_{\text{act}}$
  3. $\boldsymbol{\alpha}_{\text{old}} = \frac{\boldsymbol{\alpha}_{\text{act}} - \boldsymbol{\alpha}_{\text{old}}}{\gamma_2 \Delta t} \quad (= \mathbf{f}_{\text{nl}}(\boldsymbol{\alpha}'))$
  4. Enforce BC on $\boldsymbol{\alpha}_{\text{act}}$
  5. $\boldsymbol{\alpha}_{\text{act}} = \widetilde{\mathbf{A}}_2^{-1} \boldsymbol{\alpha}_{\text{act}}$
  6. $\boldsymbol{\alpha}_{\text{old}} = \tilde{\mathbf{B}}_3 \boldsymbol{\alpha}_{\text{act}} + \zeta_2 \Delta t \boldsymbol{\alpha}_{\text{old}}$
  7. Enforce BC on $\boldsymbol{\alpha}_{\text{old}}$
- Third RK sub–step:
  1. $\boldsymbol{\alpha}_{\text{act}} = \mathbf{f}_{\text{nl}}(\boldsymbol{\alpha}_{\text{act}})$
  2. $\boldsymbol{\alpha}_{\text{act}} = \boldsymbol{\alpha}_{\text{old}} + \gamma_3 \Delta t \boldsymbol{\alpha}_{\text{act}}$

3. Enforce BC on $\boldsymbol{\alpha}_{\text{act}}$
4. $\boldsymbol{\alpha}_{\text{act}} = \widetilde{\mathbf{A}}_3^{-1}\boldsymbol{\alpha}_{\text{act}} \qquad (= \boldsymbol{\alpha}_{n+1})$
5. $\boldsymbol{\alpha}_{\text{old}} = \boldsymbol{\alpha}_{\text{act}} \qquad (= \boldsymbol{\alpha}_{n+1})$

- Proceed to next time step

Constant mass flow

In order for the mass flow to be constant, a pressure gradient must be applied in the streamwise direction on the mean flow, i.e the $(0,0)$ mode. Let us symbolically rewrite any of the steps in C.10– C.12 as

$$\mathcal{L}v_{z_{n+1}} = RHS + \left(\mathbf{w}_{l'}{}^{-}(r;0,0), f\mathbf{e_z}\right) \tag{C.14}$$

where RHS refers to any right hand side, $f\mathbf{e_z}$ is the streamwise pressure gradient and $v_z \equiv \hat{v}_z(r,t;0,0)$. Since this pressure gradient is not explicitely known, Moser (Private communication) suggests the following: split the solution step such that

$$\mathcal{L}\check{v}_{z_{n+1}} = RHS \tag{C.15}$$

$$\mathcal{L}\tilde{v}_{z_{n+1}} = \left(\mathbf{w}_{l'}{}^{-}(r;0,0), \mathbf{e_z}\right) \tag{C.16}$$

where the $\mathbf{e_z}$ on the right hand side of C.16 refers to a unit pressure gradient. Once $\check{v}_{z_{n+1}}$ and $\tilde{v}_{z_{n+1}}$ have been computed, the actual $v_{z_{n+1}}$ can be obtained by

$$v_{z_{n+1}} = \check{v}_{z_{n+1}} + \delta\tilde{v}_{z_{n+1}} \tag{C.17}$$

All that remains to be computed is δ; defining

$$C^* = \int_0^{R_2} v_z \, r \, dr \tag{C.18}$$

which is no more than the integral in 2.3 that has to be made constant $\forall\, t$, and

$$\check{\dot{m}} = \int_0^{R_2} \check{v}_{z_{n+1}} \, r \, dr \qquad \text{and} \qquad \tilde{\dot{m}} = \int_0^{R_2} \tilde{v}_{z_{n+1}} \, r \, dr \tag{C.19}$$

then,

$$\delta = \frac{C^* - \overset{\circ}{\dot{m}}}{\overset{\circ}{\dot{m}}} \tag{C.20}$$

Finally, note that splitting the solution in two steps does not require more memory: since the imaginary part of the (0,0) mode is zero, we can use that memory location to solve for C.16.

Appendix D

Benchmark Solutions

In this appendix we present benchmark problems which were used to validate the computational procedure: Stokes problem and linear stability theory.

D.1 Solution to Stokes Problem

Stokes flow represents the low Reynolds number limit of the Navier-Stokes equations. Since diffusion dominates convection, it is possible to neglect the nonlinear convective term from the equations rendering them linear. Defining λ_s to be the eigenvalues (assuming the solution obeys $\mathbf{u} \sim e^{\lambda_s t}\mathbf{u}_s$ such that $\partial/\partial t \equiv \lambda_s$) and $\mathbf{u}_s$ and p_s the eigenfunctions of the Stokes equations,

$$\nabla \cdot \mathbf{u}_s = 0 \tag{D.1}$$

$$\lambda_s \mathbf{u}_s + \nabla p_s = \frac{1}{Re_b}\nabla \cdot \nabla \mathbf{u}_s \tag{D.2}$$

with $\mathbf{u}_s = 0$ on $r = R_2 = 1$.

D.1.1 Exact Solution

This problem was solved by Salwen and Grosch [40] by means of vector and scalar potentials. Their solution was restricted for $k_z \neq 0$ but was extended to include all wave numbers.

• $|k_z| > 0$

The eigenvalues are

$$\lambda_s = -\frac{1}{Re_b}({k_z}^2 + \beta_s^2) \tag{D.3}$$

where the β_s are the roots of the following transcendental equation

$$\beta\left(\frac{J'_{k_\theta}(\beta)}{J_{k_\theta}(\beta)}\right)\left(\frac{J'_{k_\theta}(\beta)}{\beta J_{k_\theta}(\beta)} + \frac{I'_{k_\theta}(k_z)}{k_z I_{k_\theta}(k_z)}\right) - \frac{{k_\theta}^2({k_z}^2 + \beta^2)}{{k_z}^2\beta^2} = 0 \tag{D.4}$$

and J_{k_θ} are Bessel functions and I_{k_θ} are modified Bessel functions both of the first kind (see Abramowitz and Stegun [1] chapter 9). Also, it is implied in D.4 and what follows, that $k_z \equiv |k_z|$ since the equations do not depend on the sign of k_z. Since the eigenvalues λ_s represent the decay rate of the eigenfunctions, they are all real and negative. The eigenfunctions were obtained using *Mathematica* and are given by

$$\hat{u}_{r_s}(r; k_\theta, k_z) = k_z I'_{k_\theta}(k_z r) + a J_{k_\theta+1}(\beta_s r) - b J_{k_\theta-1}(\beta_s r) \tag{D.5}$$

$$\hat{u}_{\theta_s}(r; k_\theta, k_z) = k_\theta \frac{I_{k_\theta}(k_z r)}{r} - a J_{k_\theta+1}(\beta_s r) - b J_{k_\theta-1}(\beta_s r) \tag{D.6}$$

and

$$\begin{aligned}\hat{u}_{z_s}(r; k_\theta, k_z) \;=\; & k_z I_{k_\theta}(k_z r) + \frac{a}{k_z}\left[(k_\theta + 1)\frac{J_{k_\theta+1}(\beta_s r)}{r} + \beta_s J'_{k_\theta+1}(\beta_s r)\right] + \\ & \frac{b}{k_z}\left[(k_\theta - 1)\frac{J_{k_\theta-1}(\beta_s r)}{r} - \beta_s J'_{k_\theta-1}(\beta_s r)\right]\end{aligned} \tag{D.7}$$

where

$$a \equiv \frac{k_\theta I_{k_\theta}(k_z) - k_z I'_{k_\theta}(k_z)}{2J_{k_\theta+1}(\beta_s)} \tag{D.8}$$

$$b \equiv \frac{k_\theta I_{k_\theta}(k_z) + k_z I'_{k_\theta}(k_z)}{2J_{k_\theta-1}(\beta_s)} \tag{D.9}$$

When $k_\theta = 0$, D.6 yields a trivial solution ($\hat{u}_{\theta_s} = 0$); for this case the following form is used

$$\hat{u}_{\theta_s}(r; 0, k_z) = J_1(\beta_s r) \tag{D.10}$$

where $\beta_s = j_{1,s}$ and $j_{n,s}$ is the s^{th} zero of the Bessel function of the first kind of degree

n (i.e. $J_n(j_{n,s}) = 0$, $s = 1, 2, \ldots$).

•$\mathbf{k_z = 0}$

The eigenvalues and eigenfunctions are

$$\lambda_s = -\frac{j_{k_\theta+1,s}^2}{Re_b} \tag{D.11}$$

$$\hat{u}_{r_s}(r; k_\theta, 0) = k_\theta r^{(k_\theta-1)} - k_\theta \frac{J_{k_\theta}(j_{k_\theta+1,s} r)}{r J_{k_\theta}(j_{k_\theta+1,s})} \tag{D.12}$$

$$\hat{u}_{k_{\theta_s}}(r; k_\theta, 0) = k_\theta r^{(k_\theta-1)} - j_{k_\theta+1,s} \frac{J'_{k_\theta}(j_{k_\theta+1,s} r)}{J_{k_\theta}(j_{k_\theta+1,s})} \tag{D.13}$$

When $k_z = 0$ the streamwise component decouples from the other two components,

$$\hat{u}_{z_s}(r; k_\theta, 0) = J_{k_\theta}(j_{k_\theta,s} r) \tag{D.14}$$

with the eigenvalue $\lambda_s = -j_{k_\theta,s}^2 / Re_b$.

D.1.2 Numerical Solution

The numerical approximation to this problem is identical to what was developed in 2.18–2.20. With the mass and viscous matrices computed and assembled as shown in appendix C, a generalized eigenvalue problem is obtained by replacing $\dot{\boldsymbol{\alpha}}$ by $\lambda\boldsymbol{\alpha}$; 2.18 becomes

$$\lambda \mathbf{A}\boldsymbol{\alpha} = \mathbf{B}\boldsymbol{\alpha} \tag{D.15}$$

where $\boldsymbol{\alpha}$ is the eigenvector and λ the eigenvalue. The eigenvectors are in fact b-splines coefficients that can be summed following 2.16 to yield the corresponding eigenfunction. D.15 was solved using *MATLAB* which implements the *EISPACK* libraries.

D.2 Linear Stability

Linear stability theory concerns itself with equilibrium solutions to the Navier-Stokes equations and examines the effect of growth or decay of perturbations (see Canuto [7]). Let $\mathbf{u}$ and p be solutions to the Navier-Stokes equations; define $\mathbf{U}$ and P as the equilibrium solutions and $\mathbf{u}$ and p as the perturbations such that the velocity and pressure are given by $\mathbf{U} + \mathbf{u}'$ and $P + p'$. By substituting these definitions in the Navier-Stokes equations (2.1–2.2) and neglecting quadratic terms, the linearized Navier-Stokes equations are obtained

$$\nabla \cdot \mathbf{u} = 0 \tag{D.16}$$

$$\frac{\partial \mathbf{u}}{\partial t} + \mathbf{U} \cdot \nabla \mathbf{u} + \mathbf{u} \cdot \nabla \mathbf{U} + \nabla p = \frac{1}{Re_b} \nabla \cdot \nabla \mathbf{u} \tag{D.17}$$

In studying stability of pipe flow, it is customary (see for example Salwen *et al.* [40, 39]) to adopt

$$\mathbf{U} = (1 - r^2)\mathbf{e_z} \tag{D.18}$$

with a forcing term as defined in 2.2 given by $f = 4/Re_b$, i.e. this value of f ensures that the mean flow D.18 is preserved. By assuming that perturbations have a solution of the form

$$\mathbf{u} = \hat{\mathbf{u}}(r) e^{i(k_\theta \theta + k_z z) - i\omega t} \tag{D.19}$$

D.17 can be written in a form similar to Stokes' problem

$$\lambda \mathbf{u} + \mathbf{U} \cdot \nabla \mathbf{u} + \mathbf{u} \cdot \nabla \mathbf{U} + \nabla p = \frac{1}{Re_b} \nabla \cdot \nabla \mathbf{u} \tag{D.20}$$

where $\lambda = -i\omega$. Perturbations are said to be stable if $\mathrm{Im}(\omega) < 0$. Equations D.20 is now a generalized eigenvalue problem that is solved similarly to D.15

$$\lambda \mathbf{A}\boldsymbol{\alpha} = (\mathbf{B} - \mathbf{O})\boldsymbol{\alpha} \tag{D.21}$$

with the added matrix $\mathbf{O}$ defined as

$$\mathbf{O} = \int_0^{R_2} \mathbf{w}_{l'}{}^{\pm} \cdot (\mathbf{U} \cdot \nabla \mathbf{u}_l{}^{\pm} + \mathbf{u}_l{}^{\pm} \cdot \nabla \mathbf{U})\, r\, dr \tag{D.22}$$

As for Stokes flow, the eigenvectors $\boldsymbol{\alpha}$ are b-splines coefficients that can be summed following C.4–C.6 to yield the so-called Orr-Sommerfeld waves.

Because D.22 represent a term which must be added to the computer code in order to solve D.21, it must also be validated. Leonard and Wray [20] computed λ with their fully spectral code for $Re_b = 9600$, $k_\theta = k_z = 1$; by ordering the eigenvalues such that $\mathrm{Re}(\lambda_1) \geq \mathrm{Re}(\lambda_2) \geq \ldots$, they obtained $\lambda_1 = -0.023170795764 - i\,0.950481396668$ with $N_r = 37$ Jacobi polynomials. This value compares well with Salwen *et al.* [39] who obtained $\lambda_1 = -0.02317 - i\,0.95048$ by solving D.16 and D.20 using expansions in terms of Stokes eigenfunctions.

Table D.1 gives the difference between the b-splines and the Jacobi polynomials, using the same number of functions (albeit on an equispaced grid for the splines). It is interesting to note that for $S = 7$, the fully spectral Jacobi polynomial code and the b-splines method give virtually the same answer.

Table D.1: Relative difference between b-splines of different degrees and Jacobi polynomials ($N_r = 37$).

S	$-\mathrm{Re}(\tilde{\lambda}_1)$	$-\mathrm{Im}(\tilde{\lambda}_1)$	$\lvert\tilde{\lambda}_1 - \lambda_1\rvert/\lvert\lambda_1\rvert$
3	0.023169	0.9504816	1.51×10^{-6}
4	0.0231708	0.95048142	2.06×10^{-8}
5	0.0231707960	0.9504813968	3.35×10^{-10}
6	0.023170795752	0.950481396672	1.31×10^{-11}
7	0.023170795766	0.950481396674	6.75×10^{-12}

Bibliography

[1] M. Abramowitz and I. A. Stegun. *Handbook of mathematical functions.* Dover, New York, N.Y., 1965.

[2] G.I. Barenblatt. Scaling laws for fully developed turbulent shear flows. Part 1. Basic hypotheses and analysis. *J. Fluid Mech.*, 248:513–520, 1993.

[3] G.I. Barenblatt and V.M. Prostokishin. Scaling laws for fully developed turbulent shear flows. Part 2. Processing of experimental data. *J. Fluid Mech.*, 248:521–529, 1993.

[4] H.M. Blackburn, N.N. Mansour, and B.J. Cantwell. Topology of fine-scale motions in turbulent channel flow. *J. Fluid Mech.*, 310:269–292, 1996.

[5] B.J. Cantwell. Organized motion in turbulent flow. *Ann. Rev. Fluid Mech.*, 13:457–515, 1981.

[6] B.J. Cantwell. Exact solution of a restricted Euler equation for the velocity gradient tensor. *Phys. Fluids*, 4(4):782–793, 1991.

[7] C. Canuto, M.Y. Hussaini, A. Quarteroni, and T.A. Zang. *Spectral Methods in Fluid Dynamics.* Springer-Verlag, Berlin, 1988.

[8] J.H. Chen, M.S. Chong, J. Soria, R. Sondergaard, A.E. Perry, M. Rogers, R.D. Moser, and B.J. Cantwell. A study of the topology of dissipating motions in direct numerical simulations of time-developing compressible and incompressible mixing layers. In *Studying turbulence using numerical simulation databases - III.*

Proceedings of the 1990 Summer Program, pages 139–161. NASA Ames Research Center–Stanford University, 1990.

[9] M.S. Chong, A.E. Perry, and B.J. Cantwell. A general classification of three-dimensional flow fields. *Phys. Fluids*, 2(5):765–777, 1990.

[10] C. de Boor. *A practical guide to splines.* Spinger-Verlag, Berlin, 1978.

[11] F. Durst, J. Jovanović, and J. Sender. LDA measurements in the near-wall region of a turbulent pipe flow. *J. Fluid Mech.*, 295:305–335, 1995.

[12] J.G.M. Eggels, F. Unger, M.H. Weiss, J. Westerweel, R.J. Adrian, R. Friedrich, and F.T.M. Nieuwstadt. Fully developed turbulent pipe flow: a comparison between direct numerical simulation and experiment. *J. Fluid Mech.*, 268:175–209, 1994.

[13] T.J.R. Hughes. *The finite element methods. Linear static and dynamic finite element analysis.* Prentice-Hall, Englewood Cliffs, NJ, 1987.

[14] J. Jeong and F. Hussain. On the identification of a vortex. *J. Fluid Mech.*, 285:69–94, 1995.

[15] C. Johnson. *Numerical solution of partial differential equations by the finite element method.* Cambridge University press, Cambridge, 1987.

[16] S.C. Kassinos, W.C. Reynolds, and M.M. Rogers. A study of one-point turbulent structure tensors using direct numerical simulation. To appear: J. Fluid Mech.

[17] J. Kim, P. Moin, and R.D. Moser. Turbulence statistics in a fully developed channel flow at low reynolds number. *J .Fluid Mech.*, 177:133–166, 1987.

[18] S.J. Kline, W.C. Reynolds, F.A. Schraub, and P. Runstadler. The structure of turbulent boundary layers. *J. Fluid Mech.*, 30:741–773, 1967.

[19] A. Leonard. Numerical simulation of turbulent fluid flows. *NASA Technical Memorandum 84320*, 1983.

[20] A. Leonard and A. Wray. A new numerical method for the simulation of three-dimensinal flow in a Pipe. *NASA Technical Memorandum 84267*, 1982.

[21] N.N. Mansour, J.H. Ferziger, and W.C. Reynolds. Large-eddy simulation of a turbulent mixing layer. Technical Report TF-11, Thermoscience division, Department of Mechanical Engineering, Stanford University, Stanford, CA 94305, April 1978.

[22] N.N. Mansour, J. Kim, and P. Moin. Reynolds-stress and dissipation-rate budgets in a turbulent channel flow. *J. Fluid Mech.*, 194:15–44, 1988.

[23] N.N. Mansour, J. Kim, and P. Moin. Near-wall $k-\varepsilon$ turbulence modeling. *AIAA Journal*, 27(8):1068–1073, 1989.

[24] P. Moin and J. Kim. Numerical investigation of turbulent channel flow. *J. Fluid Mech.*, 118:341–377, 1982.

[25] R.D. Moser and P. Moin. Direct numerical simulation of curved turbulent channel flow. Technical Report TF-20, Thermoscience division, Department of Mechanical Engineering, Stanford University, Stanford, CA 94305, July 1984.

[26] R.D. Moser, P. Moin, and A. Leonard. A spectral numerical method for the Navier-Stokes equations with applications to Taylor-Couette flow. *J. Comp. Phys.*, 52(3):524–544, 1983.

[27] P. Orlandi and M. Fatica. Direct simulation of a turbulent pipe rotating along the axis. *J. Fluid Mech.*, 1995. To appear.

[28] S.A. Orszag and L.C. Kells. Transition to turbulence in plane Poiseuille and plane Couette flow. *J. Fluid Mech.*, 96:159–205, 1980.

[29] S.A. Orszag and A.T. Patera. Secondary instability in wall-bounded shear flows. *J. Fluid Mech.*, 128:347–385, 1983.

[30] P.L. O'Sullivan and K.S. Breuer. Transient growth in circular pipe flow. I. Linear disturbances. *Phys. Fluids*, 6(11):3643–3651, 1994.

[31] P.L. O'Sullivan and K.S. Breuer. Transient growth in circular pipe flow. II. Nonlinear development. *Phys. Fluids*, 6(11):3652–3664, 1994.

[32] V.C. Patel and M.R. Head. Some observations on skin friction and velocity profiles in fully developed pipe and channel flows. *J. Fluid Mech.*, 38:181–201, 1969.

[33] A.E. Perry and M.S. Chong. A description of eddying motions and flow patterns using critical-point concepts. *Ann. Rev. Fluid Mech.*, 19:125–155, 1987.

[34] O. Reynolds. An experimental investigation of the circumstances which determine whether the motion of water shall be direct or sinuous, and the law of resistance in parallel channels. *Philos. Trans. Roy. Soc. Lon.*, 174:935–982, 1883.

[35] W.C. Reynolds. Fundamentals of turbulence for turbulence modeling and simulation. Class notes for ME 261B, Stanford University, Department of Mechanical Engineering, Spring 1995.

[36] W. Rodi and N.N. Mansour. Low Reynolds number $k-\varepsilon$ modelling with the aid of direct simulation data. *J. Fluid Mech.*, 250:509–529, 1993.

[37] R. S. Rogallo. Numerical experiments in homogeneous turbulence. *NASA Technical Memorandum 81315*, 1981.

[38] M.M. Rogers and R.D. Moser. Direct simulation of a self-similar turbulent mixing layer. *Phys. Fluids*, 6 (2):903–923, 1994.

[39] H. Salwen, F.W. Cotton, and C.E. Grosch. Linear stability of poiseuille flow in circular pipe. *J. Fluid Mech.*, 98:273–284, 1980.

[40] H. Salwen and C.E. Grosch. The stability of poiseuille flow in a pipe of circular cross-section. *J. Fluid Mech.*, 54:93–112, 1972.

[41] K. Shariff and R.D. Moser. Two-dimensional mesh embedding for Galerkin b-spline methods. *NASA Technical Memorandum 110361*, 1995.

[42] R. Sondergaard. *Direct numerical simulation of a temporally evolving incompressible wake: effect of initial conditions on evolution and topology.* PhD thesis, Stanford University, Stanford, CA 94305, March 1995. Also available as Stanford University, Department of Aeronautics and Astronautics, report no. SUDAAR 667.

[43] J. Soria, R. Sondergaard, B.J. Cantwell, M.S. Chong, and A.E. Perry. A study of the fine-scale motions of incompressible time-developing mixing layers. *Phys. Fluids*, 6(2):871–884, 1994. Part II.

[44] P.R. Spalart, R.D. Moser, and M.M. Rogers. Spectral methods for the Navier-Stokes equations with one infinite and two periodic directions. *J. Comp. Phys.*, 96(2):297–324, 1991.

[45] S.K. Stanaway, B.J. Cantwell, and P.R. Spalart. A numerical study of viscous vortex rings using a spectral method. *NASA Technical Memorandum 101041*, 1988.

[46] G. Strang and G. J. Fix. *An analysis of the finite element method.* Prentice-Hall, Englewood Cliffs, N.J., 1973.

[47] H. Tennekes and J.L. Lumley. *A first course in yurbulence.* MIT Press, Cambridge, Mas., 1972.

[48] R. Verzicco and P. Orlandi. Direct simulations of the transitional regime of a circular jet. *Phys. Fluids*, 6(2):751–759, 1994. Part 2.

[49] R. Verzicco and P. Orlandi. A finite-difference scheme for three-dimensional incompressible flows in cylindrical coordinates. *J. Comp. Phys.*, 123:402–414, 1996.

[50] J. Westerweel, A.A. Draad, J.G.Th.van der Hoeven, and J. van Oord. Measurement of fully-developed turbulent pipe flow with digital particle image velocimetry. to appear in Experiments in Fluids.

[51] A. A. Wray. A manual of the vectoral language. Private communication, 1995.

[52] I.J. Wygnanski and F.H. Champagne. On transition in a pipe part 1. the origin of puffs and slugs and the flow in a turbulent slug. *J. Fluid Mech.*, 59:281–335, 1973.

[53] I.J. Wygnanski, M. Sokolov, and D. Friedman. On transition in a pipe 2. the equilibrium puff. *J. Fluid Mech.*, 69:283–304, 1975.

[54] C. Xu, J.M.J. den Toonder, F.T.M. Nieuwstadt, and Z. Zhang. Origin of high kurtosis levels in the viscous sublayer. Direct numerical simulation & experiment. To appear: Phys. Fluids.

[55] Y. Zhang, A. Gandhi, A.G. Tomboulides, and S.A. Orszag. Simulation of pipe flow. In *Symposium on application of direct and large eddy simulation to transition and turbulence*, volume CP-551, pages 17.1–17.9. AGARD, 1994.

REPORT DOCUMENTATION PAGE

Form Approved
OMB No. 0704-0188

Public reporting burden for this collection of information is estimated to average 1 hour per response, including the time for reviewing instructions, searching existing data sources, gathering and maintaining the data needed, and completing and reviewing the collection of information. Send comments regarding this burden estimate or any other aspect of this collection of information, including suggestions for reducing this burden, to Washington Headquarters Services, Directorate for information Operations and Reports, 1215 Jefferson Davis Highway, Suite 1204, Arlington, VA 22202-4302, and to the Office of Management and Budget, Paperwork Reduction Project (0704-0188), Washington, DC 20503.

1. AGENCY USE ONLY *(Leave blank)*	2. REPORT DATE	3. REPORT TYPE AND DATES COVERED
	February 1997	Technical Memorandum

4. TITLE AND SUBTITLE

Direct Numerical Simulation of Incompressible Pipe Flow Using a B-Spline Spectral Method

5. FUNDING NUMBERS

505-59-53

6. AUTHOR(S)

Patrick Loulou,* Robert D. Moser, Nagi N. Mansour, and Brian J. Cantwell*

7. PERFORMING ORGANIZATION NAME(S) AND ADDRESS(ES)

Ames Research Center
Moffett Field, CA 94035-1000

8. PERFORMING ORGANIZATION REPORT NUMBER

A-975743

9. SPONSORING/MONITORING AGENCY NAME(S) AND ADDRESS(ES)

National Aeronautics and Space Administration
Washington, DC 20546-0001

10. SPONSORING/MONITORING AGENCY REPORT NUMBER

NASA TM-110436

11. SUPPLEMENTARY NOTES

Point of Contact: Nagi N. Mansour, Ames Research Center, MS 202A-1, Moffett Field, CA 94035-1000
(415) 604-6420
*Stanford University, Stanford, California

12a. DISTRIBUTION/AVAILABILITY STATEMENT

Unclassified — Unlimited
Subject Category 34

12b. DISTRIBUTION CODE

13. ABSTRACT *(Maximum 200 words)*

A numerical method based on b-spline polynomials was developed to study incompressible flows in cylindrical geometries. A b-spline method has the advantages of possessing spectral accuracy and the flexibility of standard finite element methods. Using this method it was possible to ensure regularity of the solution near the origin, i.e. smoothness and boundedness. Using the natural periodicity in the azimuthal direction and approximating the streamwise direction as periodic, so-called time evolving flow, greatly reduced the cost and complexity of the computations.

A direct numerical simulation of pipe flow was carried out using the method described above at a Reynolds number of 5600 based on diameter and bulk velocity. Budgets of Reynolds stress transport equations showed close similarity with those of channel flow. However contrary to channel flow, the log layer of pipe flow is not homogeneous for the present Reynolds number. A topological method based on a classification of the invariants of the velocity gradient tensor was used. Plotting iso-surfaces of the discriminant of the invariants proved to be a good method for identifying vortical eddies in the flow field.

14. SUBJECT TERMS	15. NUMBER OF PAGES
Turbulent pipe flow, B-spline methods, Direct numerical simulations	157
	16. PRICE CODE: A08

17. SECURITY CLASSIFICATION OF REPORT	18. SECURITY CLASSIFICATION OF THIS PAGE	19. SECURITY CLASSIFICATION OF ABSTRACT	20. LIMITATION OF ABSTRACT
Unclassified	Unclassified		